ATLAS Note

HDBS-2018-37

26th March 2020

Draft version 0.18

Search for Decays of the Higgs Boson into a Z Boson and a Light Hadronically Decaying Resonance

Andrew Chisholm[a], Konstantinos Nikolopoulos[a], Elliot Reynolds[a]

[a]*University of Birmingham*

A search for decays of the Higgs boson to a Z boson and a light resonance in two lepton plus jet events, using the full Run 2 (2015-2018) dataset of 139 fb^{-1} is presented. The target resonance is an a^0 from the Two Higgs Doublet Model, or a J/ψ or η_c, which decays hadronically. Due to its low mass and high boost, the resonance is reconstructed as a single jet of hadrons, while the Z boson is reconstructed as a dilepton system. A multivariate event selection based on a Multi-Layer Perceptron is followed by a single-bin profile likelihood fit. In the absence of a signal, 95% CL_s upper limits on $\sigma(H)\mathrm{BR}(H \to Za^0)/\sigma_{\mathrm{SM}}(H)$ are set, with values starting from 16.8 pb for the signal hypothesis of a 0.5 GeV a^0 decaying to gluons, and 105 pb and 107 pb for the J/ψ and η_c, respectively.

Version 0.1 (CDS Version 7) - 17 June 19

Notes

- First draft presented to EB at first meeting.

- Comments from EB on CDS.

To-do

- Calculate and implement uncertainty to account for the fact that inclusive Higgs cross section is used to scale signal, while only ggF is modelled.

- Calculate and implement alternative parton shower uncertainty (probably based on HERWIG).

- Calculate and implement jet uncertainties.

- Calculate and implement PDF, factorisation and renormalisation SF uncertainties.

- Calculate and implement tracking uncertainties.

- Respond to comments from EB on CDS.

Version 0.2 (CDS Version 10) - 4 August 19

Notes

- Iteration of note for second EB meeting.

- Responded to comments on first iteration from EB on CDS.

Main Documentation Changes

- Changelog added at start of note

- All results updated as per analysis changes, which are described below.

- Background in plots of variables in Section 3 reweighted as per Section 4.2.1.

- Reweighting plots in Section 4.2.1 now shown with and without reweighting, side by side.

- Three addition validation regions with $150 < m_{\ell\ell\mathrm{j}} < 155$ GeV added to background validation tables of Section 4.2.3.

- New plot (Figure 22) showing all validations regions in MC and data.

- Numbers in Table 6 now calculated using only events with $120 < m_{\ell\ell\mathrm{j}} < 135$ GeV.

- Added Section 5.1.4, describing the hadronisation uncertainty which will be added.

- Updated Section 5.1.5, describing the acceptance uncertainty which has been added.

- Updated Section 5.2.1, describing the jet uncertainties which have been added.

- Table of correct X selection efficiencies replaced with range given in main text.

- Plots of toy limit distributions and profile likelihood scans updated to remove background MC statistical uncertainty from no-systematics plots.

- New model-independent results section: Section 6.4.

- Appendix on signal contamination added (now out of date).

- Appendix H added.

Analysis Changes

- $ggZZ$ cross section corrected (it was set to the ZZ cross section).

- All cross sections updated for slight changes (previously using MC15 values). Changes all negligible.

- Lepton SF updated to latest CP recommendations. Changes on $\sim 1\%$ level.

- Updated luminosity to latest recommendations. $\sim 2\%$ decrease in 2018 luminosity.

- Removed duplicated data events. Change negligible.

- Introduced uncertainty to account for the fact that inclusive Higgs cross section is used, while only ggF is modelled.

- Calculated, but not yet introduced, PDF, factorisation and renormalisation SF uncertainties.

- Introduced JES uncertainty. Note the asymmetric effect on the likelihood, described in Section 5.2.1.

- Unblinded region with $150 < m_{\ell\ell j} < 155$ GeV as additional validation region.

- Produced model-independent limits, as described in Section 6.4.

To-do

- Implement PDF, factorisation and renormalisation SF uncertainties.

- Calculate and implement alternative parton shower uncertainty (based on Herwig).

- Calculate and implement tracking uncertainties.

- Recast limits in terms of $\sigma \times$BRs

Version 0.3 (CDS Version 13) - 10 September 19

Notes

- Iteration of note for third EB meeting.

Main Documentation Changes

- Section added/adjusted for all Analysis Changes.

- Text and figure added explaining signal distribution of three body mass.

- Subsection on fits to toy datasets removed.

Analysis Changes

75 • Background model updated to use 10% MLP ABCD regions, as described in second EB meeting.

76 • Showering/ME systematics added for signal and background.

77 • Renormalisation scale systematics added for signal and background.

78 **To-do**

79 • Calculate and implement tracking uncertainties.

80 • Recast limits in terms of $\sigma\times$BRs.

81 # Version 0.4 (CDS Version 15) - 20 September 19

82 **Notes**

83 • Iteration of note for unblinding circulation

84 **Main Documentation Changes**

85 • Section added/adjusted for all Analysis Changes.

86 • Text added mentioning Herwig modelling issues.

87 **Analysis Changes**

88 • Tracking uncertainties calculated.

89 • Signal showering uncertainty for 3.5 GeV a signal hypothesis interpolated from values determined
90   on signal hypothesis with close masses.

91 • Bug fixed in MadGraph background reweighting

92 **To-do**

93 • Recast limits in terms of $\sigma\times$BRs.

94 # Version 0.5 (CDS Version 16) - 27 September 19

95 **Notes**

96 • Post-unblinding iteration of note.

97 **Main Documentation Changes**

98 • Results section updated with final results.

99 • Track studies plots updated with remaining signal samples.

100 • Various tables reformatted, including adding uncertainties.

101 **Analysis Changes**

102 • None.

To-do

- Recast limits in terms of $\sigma \times$BRs.

Version 0.6 (CDS Version 21) - 4 October 19

Notes

- Pre HDBS approval iteration of note.

Main Documentation Changes

- Extended unblinded classification MLP output plot range.

Analysis Changes

- Added limits which have been recast in terms of $\sigma \times$BRs.

To-do

- None.

Version 0.7 (CDS Version 22) - 14 October 19

Notes

- Pre HDBS approval second iteration of note, after responding to comments from Maximilian and Wade.

Main Documentation Changes

- New pages added between sections.

- Motivation section expanded.

- Appendix added with plots of MLP inputs in the SR.

- Section added describing reweighting uncertainty studies.

- Table added summarising background uncertainties.

Analysis Changes

- None.

To-do

- None.

Version 0.8 (CDS Version 23) - 14 October 19

Notes

- Post HDBS approval iteration of note.

Main Documentation Changes

- Description of indirect constraints on non-SM Higgs decays from couplings measurements added to *a* literature review section.

Analysis Changes

- None.

To-do

- None.

Version 0.9 (CDS Version 23) - 14 October 19

Notes

- Second post HDBS approval iteration of note.

Main Documentation Changes

- Addition of tables detailing signal systematic uncertainties: Tables 14 and 15.

- Addition of descriptions of the treatment of any possible uncertainties arising from the reweighting procedure in Section 5.1.8.

- Plots added comparing the nominal background prediction, MADGRAPH-based background prediction, and data, in all analysis regions (validation and signal). These are Figures 22 and 23.

Analysis Changes

- None.

To-do

- None.

Version 0.10 (CDS Version 23) - 16 January 20

Notes

- EB approved, HDBS approval iteration of the note.

Main Documentation Changes

- Small changes to reflect analysis changes.

- Generator-level acceptance added.

- Plots now include previously blinded data and MC.

- Merged signal and background MC statistics systematics sections.

Analysis Changes

- Explicit 18 GeV lepton p_{T} cut applied.

- Removed high weight SHERPA events as per PMG recommendations.

- NNLO signal scale factors added.

- Signal parton shower systematic uses 2D reweighting in the track multiplicity and $U1(0.7)$, and does not require interpolation. Also, bug fixed in which inconsistent selection was being used for two generator-level samples.

- Bug fixed in which changes to cross section were being included in the estimation of the signal renormalisation scale uncertainties.

To-do

- None.

Version 0.11 (CDS Version 24) - 20 January 20

Notes

- EB approved, HDBS approval iteration of the note, with improved plots for auxiliary material.

Main Documentation Changes

- Various figures updated/neatened, ready to be used as auxiliary material.

Analysis Changes

- None.

To-do

- None.

Version 0.12 (CDS Version 25) - 22 January 20

Notes

- EB approved, HDBS approval iteration of the note, with improved plots for auxiliary material.

Main Documentation Changes

- Various figures updated/neatened further, ready to be used as auxiliary material.

Analysis Changes

- None.

To-do

- None.

Version 0.13 (CDS Version 26) - 24 January 20

Notes

- EB approved, HDBS approval iteration of the note, with improved plots for auxiliary material.

Main Documentation Changes

- Various figures updated/neatened further, ready to be used as auxiliary material.

Analysis Changes

- None.

To-do

- None.

Version 0.14 (CDS Version 27) - 27 January 20

Notes

- EB approved, HDBS approval iteration of the note, with improved plots for auxiliary material.

Main Documentation Changes

- Labels fixed on limit plots.

Analysis Changes

- None.

To-do

- None.

Version 0.15 (CDS Version 28) - 31 January 20

Notes

- Circulation version of note.

Main Documentation Changes

- Minor changes to plots to make them compatible with paper auxiliary plots.

Analysis Changes

- None.

To-do

- None.

Version 0.16 (CDS Version 29) - 6 February 20

Notes

- Post first circulation version of note.

Main Documentation Changes

- Minor changes to plots to make them compatible with paper auxiliary plots.

Analysis Changes

- None.

To-do

- None.

Version 0.17 (CDS Version 30) - 3 March 20

Notes

- Post first circulation version of note, with modified background modelling systematics.

Main Documentation Changes

- Documentation updated to account for modified background modelling systematics.

- Plots and tables harmonised with those in paper.

- Table 16 fixed. It was showing $\Delta\mu$ for $\mu = 0$ before.

Analysis Changes

- Modified background modelling systematics.

₂₃₃ **To-do**

₂₃₄ • None.

₂₃₅ Version 0.18 (CDS Version 31) - 26 March 20

₂₃₆ **Notes**

₂₃₇ • Cutflow added.

₂₃₈ **Main Documentation Changes**

₂₃₉ • Appendix K added with cutflow.

₂₄₀ **Analysis Changes**

₂₄₁ • None.

₂₄₂ **To-do**

₂₄₃ • None.

Contents

301 # List of contributions

Andrew Chisholm	Analyser.
Konstantinos Nikolopoulos	Analyser.
Elliot Reynolds	Analyser.

302

303

1 Introduction

This analysis searches for decays of the Higgs boson to a Z boson, and a light (≤ 4 GeV) resonance. The Z boson is required to decay to leptons (ℓ), specifically electrons (e) or muons (μ), although the selection has some acceptance for decays to pairs of τ leptons if they both decay leptonically. Hadronic decays of the light resonance are targeted, and due to its low mass and large boost, they are reconstructed as a single jet of hadrons. The full Run 2 dataset is used. This is a dual interpretation analysis: first, a Standard Model (SM) charmonium resonance (η_c or J/ψ); second, the light pseudo-scalar resonance (a) from the Two Higgs Doublet Model (2HDM), or 2HDM with an additional singlet (2HDM+s).

1.1 Charmonium States

The ad-hoc nature of the Yukawa sector makes the coupling of the Higgs boson to quarks an ideal place to search for new physics. The couplings of the Higgs boson to third generation quarks have been established experimentally [1–4]. However, the coupling of the Higgs boson to first and second generation quarks have not yet been measured. With the largest mass of the first or second generation quarks [5], the charm quark provides the frontier of the couplings of the Higgs boson to quarks. Decays of the Higgs boson to a Z boson and light SM resonances provide an effective probe of this part of the Higgs sector [6–8], but are still only loosely constrained. However, the potential of searches for decays of the Higgs boson to bosons and light SM resonances has been demonstrated by the ATLAS experiment [9–12], though only in exclusive decay modes of the resonance. Searches have also been performed for inclusive Higgs boson decays to pairs of charm quarks [13], but never through a charmonium resonance. This is the first search at the LHC for decays of the Higgs boson to a final state containing a J/ψ or an η_c which decays to an inclusive hadronic final state. These decays provide a low Q^2 probe of $H \to ZZ^*$, in addition to probing the coupling of charm quark to the Higgs boson. With a SM branching ratio ($\mathcal{B}$) of 1.4×10^{-5} (2.2×10^{-6}) [14] the $H \to Z\eta_c$ ($H \to ZJ/\psi$) decay channels are highly sensitive to modifications from new physics [14, 15].

1.2 Light Higgs Bosons

The SM Higgs sector is the simplest mechanism to generate the masses of the W and Z bosons, though extended Higgs sectors are also possible. Two such extensions are the Two Higgs Doublet Model (2HDM) [16] and 2HDM with an additional singlet (2HDM+S) [16, 17], where the a can have a large coupling to the observed Higgs boson. These models are necessary to generate the masses in the Minimal Supersymmetric Model (MSSM), and the Next-to-MSSM (NMSSM), respectively [18]. The extension of the MSSM by this additional scalar field elegantly solves the μ-problem of the MSSM [19], and greatly reduces the fine-tuning and little hierarchy problems. Due to the narrow width of a SM Higgs boson with a mass of 125 GeV, even a small coupling to a non-SM Higgs boson could result in new decay modes with large branching ratios. The Yukawa-like couplings of these light Higgs bosons mean that for the mass range considered in this search, $m_a < 4$ GeV, their dominant branching ratios lead to hadronic final states, as shown in Figure 1 [20].

Previous searches for decays of the Higgs boson to light Higgs bosons at the LHC lead to upper limits from CMS in the $H \to aa \to \mu^+\mu^-\tau^+\tau^-$ [21], $H \to aa \to \mu^+\mu^-b\bar{b}$ [22], $H \to aa \to \tau^+\tau^-\tau^+\tau^-$ [23, 24] and $H \to aa \to \mu^+\mu^-\mu^+\mu^-$ [25] decay modes, and from ATLAS in the $H \to aa \to \mu^+\mu^-\tau^+\tau^-$ [26], $H \to aa \to b\bar{b}b\bar{b}$ [27], $H \to (Z/a)a \to \ell_1^+\ell_1^-\ell_2^+\ell_2^-$ [28], $H \to aa \to b\bar{b}\mu^+\mu^-$ [29], $H \to aa \to \gamma\gamma$jj [30],
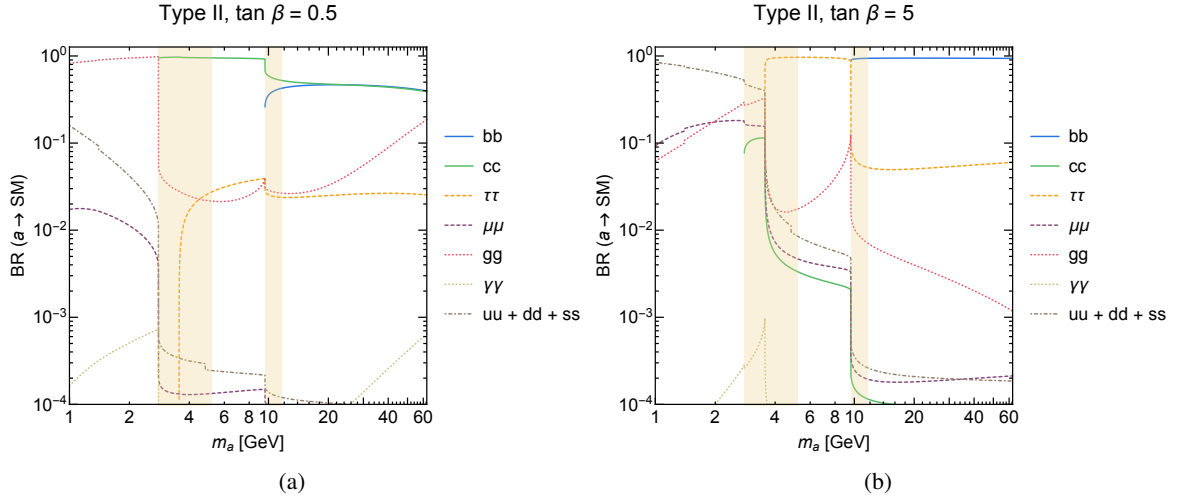
Figure 1: Branching ratios for the decay of the lightest pseudoscalar Higgs boson in the Type II 2HDM+s, for $tan\beta = 0.5$ (a) and $tan\beta = 5$ (b). [20].

and $H \rightarrow aa \rightarrow \gamma\gamma\gamma\gamma$ [31] decay modes. Previously, the DØ experiment at the Tevatron set limits in the $H \rightarrow aa \rightarrow \mu^+\mu^-\mu^+\mu^-$ and $H \rightarrow aa \rightarrow \mu^+\mu^-\tau^+\tau^-$ decay modes [32]. These previous searches have mostly been limited to $H \rightarrow aa$ decays, and a final states including leptons, photons or bottom quark pairs. This is the first search for hadronic decays of the a over this mass range, and one of the few searches for $H \rightarrow Za$ decays, and therefore it provides complementary information to the above searches [8]. This search is particularly important in the low (high) tan β phase space of the Type-II and Type-III (Type-I and Type-IV) 2HDM and 2HDM+S, where a decays to leptons are suppressed, leading to almost exclusively hadronic decays [16]. Therefore, these parts of the 2HDM(+S) phase space are largely unconstrained by previous searches, but can be probed with this search.

Constraints on decays of the Higgs boson to light Higgs bosons exist from simultaneous fits to the observed Higgs boson decay modes, which set a limit on decays of the Higgs boson to non-SM final states at 22% [33]. However, this constraint assumes SM couplings to the SM particles. If this assumption is relaxed, then the constraint on non-SM decays of the Higgs boson relaxes to $\sim$ 50% [33].

2 Experimental and Simulated Data Samples

2.1 Data Samples

The data used in this search correspond to the full Run 2 dataset, collected by the ATLAS detector between 2015-2018, using single-lepton triggers. This represents a total integrated luminosity of 139 fb^{-1}. This corresponds to: 3.2 fb^{-1} of 2015 data; 33.0 fb^{-1} of 2016 data; 44.3 fb^{-1} of 2017 data; and 58.5 fb^{-1} of 2018 data. This dataset is then processed using the *FTAG2* derivation, in order to reduce the size of the dataset, while retaining tracking information, which is necessary to separate the light resonance from multijet production. The Good Run Lists (GRL) applied are provided in Table 1. The datasets are listed in Appendix A. Finally, it was noticed that some data events were duplicated in the final data files. These events are removed in the analysis-level software.

Year	GRL
2015	All_Good_25ns
2016	All_Good_25ns
2017	All_Good_25ns_Triggerno17e33prim
2018	All_Good_25ns_Triggerno17e33prim

Table 1: Good Run Lists applied to each year of data. 2015 only had 25 ns runs.

2.2 Monte-Carlo Samples

Monte-Carlo (MC) simulation samples are used to guide the development of this analysis, and are used directly in the signal and background modelling. These MC samples are summarised in Table 2. The complete list of MC samples used in this analysis can be found in Appendices B and C, for signal and background samples respectively. All MC samples used in this analysis have been processed using the *FTAG2* derivation.

Having the largest cross section, MC samples in which Higgs bosons are produced via gluon-gluon Fusion (ggF) are generated for use in this analysis. The Higgs boson is produced in Powheg [34–36], using the AZNLO tune [37]. The decay, hadronisation, parton shower and underlying event are modelled using Pythia8 [38] (v8.212) and EvtGen [39], interfaced to the CT10 [40] and CTEQ6L1 PDF sets. For the BSM signal hypotheses, the SM Higgs boson (pdgId=25) is replaced by the heavy neutral scalar Higgs from the 2HDM (H^0, pdgId=35), which is then decayed in Pythia8 to a Z boson and a neutral pseudo-scalar a (pdgId=36). The a is allowed to decay to any final state, to ensure that any decay mode with a significant selection efficiency is considered, and the default Pythia8 2HDM $\tan\beta$ value of 1 is used to generate the decays of the BSM Higgs bosons. These resulting BRs are shown in Table 3. Lastly, NNLO corrections are applied to the p_T distribution of the Higgs boson.

The background for this analysis is dominated by Z + jets events, which is modelled using the ATLAS recommendations [41]. This choice is further motivated by this sample having a NLO ME calculation, and showing the best data to MC agreement of the samples we have studied. The calculation of the hard scatter and parton shower tuning is done with Sherpa2.2.1 [42] interfaced to the NNPDF [43] PDF sets. The samples are sliced according to the maximum of the scalar sum of the p_T of all jets and leptons in the event (H_T), and the p_T of the Z boson, at generator-level. They are further split by the presence of heavy flavour

	Process	Generator	Shower	DSID	Notes
Signal	$gg \rightarrow H \rightarrow Z(\ell\ell) + \eta_c$	Powheg+Pythia8	Pythia8+EvtGen	345906	
	$gg \rightarrow H \rightarrow Z(\ell\ell) + J/\psi$	Powheg+Pythia8	Pythia8+EvtGen	450549	
	$gg \rightarrow H \rightarrow Z(\ell\ell) + a$	Powheg+Pythia8	Pythia8+EvtGen	345907	$m_a = 0.5$ GeV
				450550	$m_a = 0.75$ GeV
				450551	$m_a = 1$ GeV
				450552	$m_a = 1.5$ GeV
				450553	$m_a = 2$ GeV
				345908	$m_a = 2.5$ GeV
				450554	$m_a = 3$ GeV
				450555	$m_a = 3.5$ GeV
				450556	$m_a = 4$ GeV
				345909	$m_a = 8$ GeV
Background	$pp \rightarrow Z(\ell\ell) + jets$	Sherpa2.2.1		364100-364141	$Max(H_T, p_T^V)$ slices and flavour filtered
	$gg \rightarrow Z(\ell\ell) + Z(q\bar{q})$	Sherpa2.2.2		364302	
	$pp \rightarrow Z(\ell\ell) + Z(q\bar{q})$	Sherpa2.2.1		363356	
	$pp \rightarrow Z(\ell\ell) + W(q\bar{q})$	Sherpa2.2.1		363358	
	$pp \rightarrow t\bar{t}$	Powheg	Pythia8+EvtGen	410503	$\geq 2\ell$

Table 2: Signal and background processes simulated with MC for this analysis.

a Mass	Branching Ratio
0.5 GeV	gg (92%), $\mu^+\mu^-$ (8%)
0.75 GeV	gg (88%), $\mu^+\mu^-$ (12%)
1 GeV	gg (88%), $\mu^+\mu^-$ (12%)
1.5 GeV	gg (76%), $s\bar{s}$ (16%), $\mu^+\mu^-$ (8%)
2 GeV	gg (82%), $s\bar{s}$ (13%), $\mu^+\mu^-$ (5%)
2.5 GeV	gg (88%), $s\bar{s}$ (8%), $\mu^+\mu^-$ (4%)
3 GeV	gg (86%), $s\bar{s}$ (9%), $\mu^+\mu^-$ (4%)
3.5 GeV	$c\bar{c}$ (88%), gg (10%), $s\bar{s}$ (1%)
4 GeV	$c\bar{c}$ (57%), $\tau^+\tau^-$ (37%), gg (5%)
4.5 GeV	$c\bar{c}$ (52%), $\tau^+\tau^-$ (43%), gg (4%)
5 GeV	$c\bar{c}$ (50%), $\tau^+\tau^-$ (45%), gg (4%)
8 GeV	$\tau^+\tau^-$ (45%), $c\bar{c}$ (40%), gg (14%)
12 GeV	$b\bar{b}$ (81%), $\tau^+\tau^-$ (10%), $c\bar{c}$ (7%), gg (2%)

Table 3: Branching ratios of the main decay modes (BR> 1%), for various a mass points. Values are determined in Pythia8 using the default BSMHiggs $\tan\beta$ value of 1.

388 partons at generator-level. The inclusive production cross sections are known to NNLO in QCD [44]. As
389 per the ATLAS PMG recommendations, for all of the SHERPA samples used in this analysis anomalous
390 high-weight (magnitude above 100) events have their event weights set to 1.

391 The ZZ and ZW processes constitute small ($< 1\%$) backgrounds to this analysis. The diboson backgrounds
392 are also modelled according to the ATLAS recommendations [45]. SHERPA2.2.1 is interfaced to the
393 NNPDF 3.0 PDF set for the modelling of the hard interaction and parton shower.

394 The $t\bar{t}$ process constitutes are further, small ($< 1\%$) background to this analysis. The hard interaction for
395 the $t\bar{t}$ background is modelled using POWHEG, while the decay, hadronisation, parton shower and underlying
396 event are modelled using PYTHIA8 and EVTGEN.

397 In addition to the nominal background MC samples, the dominant Z + jets background is modelled using
398 an alternative MC generator, in order to have a second estimate of the main background with which to
399 cross check the first. This sample uses events generated from MADGRAPH_aMC@NLO, PYTHIA8 and
400 EVTGEN. The generator tune is A14, and the PDF set is NNPDF23LO. The $Z \rightarrow e^+e^-$ and $Z \rightarrow \mu^+\mu^-$
401 samples are sliced based on H_{T} and heavy flavour filters, while the $Z \rightarrow \tau^+\tau^-$ sample is slides based on
402 the number of additional final state particles.

403 A full simulation of the ATLAS detector [46] in GEANT4 [47] is used to estimate the response of the ATLAS
404 detector in all of the above samples. Data-driven corrections are applied to the event level-trigger efficiency,
405 the jet vertex tagging efficiency, the electron reconstruction, identification and isolation efficiencies, and
406 the muon reconstruction, isolation and track-to-vertex association efficiencies.

407 Lastly, the design of the substructure-based selection was assisted using additional signal samples, with
408 finely sampled a mass values of: 0.4, 0.5, 0.75, 0.8, 1, 1.2, 1.5, 1.6, 2, 2.4, 2.5, 2.8, 3, 3.2, 3.5, 3.6 and
409 4 GeV, and a high-statistics Z+jets background sample of 20M events. These additional samples were
410 generated using PYTHIA8, and the response of the ATLAS detector was simulated using DELPHES with the
411 ATLAS card. These samples were used to explore different strategies to maximise the substructure-based
412 selection efficiency over the entire a mass range (which was not possible with the limited number of
413 full-simulation samples we had at hand), to ensure that the selection efficiency did not dip significantly for
414 a mass points not used in the optimisation, and as a second validation of the final selection.

3 Event Selection

The full event selection can be broken down into three main stages. First, an event-level pre-selection is applied, which targets a 2-lepton plus jet (used to reconstruct the target BSM or SM charmonium resonance) final state. This final state is contaminated by a large Z+jets background, and so track-based substructure techniques are used to discriminate between the signal resonances and the QCD background jets. The high resolution of the inner-tracker is required to do this, and so the second stage of the selection involved Ghost-Associating tracks to the reconstructed jet, and applying a loose track-selection in order to reject backgrounds from pileup, the underlying event, multiple parton interactions and fake tracks. Finally, the tracks surviving this track-selection are used to form substructure-based discriminants, which are given to a classification machine learning algorithm, to which we apply a requirement that discriminates signal from background.

3.1 Event-Level Pre-Selection

Events are triggered for offline storage using the lowest unprescaled single lepton trigger for each period. These are listed in Table 4. The studies justifying this choice of trigger menu are detailed in Appendix D. The trigger decisions are implemented using the *Trig::TrigDecisionTool* tool [48]. The trigger objects which fired the triggers are required to be matched to the offline leptons using the *Trig::MatchingTool* tool [49], which implements a requirement of $\Delta R < 0.1$ between the trigger object and the corresponding offline object.

Electron candidates are reconstructed offline by matching tracks in the inner detector to topological energy clusters in the electromagnetic calorimeter [50]. These electrons are then required to pass the *Medium* likelihood-based identification working point, which requires that the shower profile be compatible with that of an electromagnetic shower, and is implemented using the *DFCommonElectronsLHMedium xAOD* decoration [51]. The *FixedCutLoose* isolation working point is also applied, requiring the electrons to have a transverse energy sum in a cone of $\Delta R < 0.2$ around the electron of less than 20% of its p_{T}, and the p_{T} of tracks within a variable-width cone of $\Delta R < \mathrm{Min}(0.2,\ 10\ \mathrm{GeV}/p_{\mathrm{T}})$ of the electron must be less than 15% of its p_{T}, as implemented by the *IsolationSelectionTool* and *IsolationCloseByCorrectionTool* [52]. Close-by leptons are removed from the cones. The electrons must also have a longitudinal impact parameter ($z_0 sin\theta$) of less than 0.5 mm with respect to the reconstructed primary vertex, defined as the vertex with the highest sum of square track p_{T}. They are required to have a p_{T} of at least 18 GeV due to the *FTAG2* derivation[1], and be found in the central body of the detector ($|\eta| < 2.47$), but not the transition region ($1.37 < |\eta| < 1.52$). The leading lepton is required to have a p_{T} of at least 27 GeV, due to the trigger requirement. The reconstruction, identification and isolation efficiencies of these electrons are calibrated using the *AsgElectronEfficiencyCorrectionTool* tool [53], and the momentum is calibrated using the *EgammaCalibrationAndSmearingTool* [54].

Muon candidates are most often reconstructed offline by matching tracks in the inner detector to complete or partial tracks in the muon spectrometers [55]. If a complete track is present, the two momentum measurements are combined, else the inner detector track momentum measurement is used. In the absence of a track in the inner detector, a stand alone track in the muon spectrometer is used. In the center of the barrel of the detector ($|\eta| < 0.1$) there is no muon spectrometer coverage, and so tracks with a $p_{\mathrm{T}} > 15$ GeV are reconstructed as muons if they are matched to calorimeter deposits compatible with a

---

[1] This reduces the signal acceptance by approximately 5%, while also reducing the background acceptance.

Period	Triggers
2015	*HLT_mu20_iloose_L1MU15* *HLT_mu40* *HLT_e24_lhmedium_L1EM20VH* *HLT_e60_lhmedium* *HLT_e120_lhloose*
2016 A	*HLT_mu26_ivarmedium* *HLT_mu40* *HLT_e26_lhtight_nod0_ivarloose* *HLT_e60_lhmedium_nod0* *HLT_e140_lhloose_nod0*
2016 B-E	*HLT_mu26_ivarmedium* *HLT_mu50* *HLT_e26_lhtight_nod0_ivarloose* *HLT_e60_lhmedium_nod0* *HLT_e140_lhloose_nod0*
2016 F-L	*HLT_mu26_ivarmedium* *HLT_mu50* *HLT_e26_lhtight_nod0_ivarloose* *HLT_e60_lhmedium_nod0* *HLT_e140_lhloose_nod0*
2017	*HLT_mu26_ivarmedium* *HLT_mu50* *HLT_e26_lhtight_nod0_ivarloose* *HLT_e60_lhmedium_nod0* *HLT_e140_lhloose_nod0*
2018	*HLT_mu26_ivarmedium* *HLT_mu50* *HLT_e26_lhtight_nod0_ivarloose* *HLT_e60_lhmedium_nod0* *HLT_e140_lhloose_nod0*

Table 4: Triggers used to select events in data for the full Run 2 dataset. The letters correspond to the different run periods.

minimum ionising particle. Reconstructed muons are required to pass a *Medium* quality working point, as implemented by the *MuonSelectionTool* [56]. The *FixedCutLoose* isolation working point is applied using the *IsolationSelectionTool* and *IsolationCloseByCorrectionTool*, requiring the transverse energy sum in a cone of $\Delta R < 0.2$ around the muon of less than 30% of its p_T, and the p_T of tracks within a variable-width cone of $\Delta R < \text{Min}(0.15, 10 \text{ GeV}/p_T)$ of the muon must be less than 15% of its p_T. If an inner detector track is present, the muons must also have a longitudinal impact parameter ($z_0 sin\theta$) of less than 0.5 mm, and a transverse impact parameter (d_0) of less than 1 mm, with respect to the primary vertex. They are required to have a p_T of at least 18 GeV due to the *FTAG2* derivation[1], and be found within the acceptance of the muon spectrometers ($|\eta| < 2.7$). The leading lepton is required to have a p_T of at least 27 GeV, due to the trigger requirement. The reconstruction, isolation and track-to-vertex association efficiencies of these muons are calibrated using the *MuonEfficiencyScaleFactors* tool [57], and the momentum is calibrated using the *MuonCalibrationAndSmearingTool* [58].

Due to the low mass of the resonance, and the relatively large kinetic energy imparted to it from the mass difference between the Higgs and Z bosons, the resonance is highly boosted. The spread of the *a* decay products is contained in a cone of width $\Delta R \approx 2m_a/p_{T, a}$, which for our largest mass point (4 GeV) and lowest p_T jet (20 GeV), gives a cone size of 0.4. For this reason, it is reconstructed as a single anti-k_T jet with a radius parameter of 0.4, formed of topological calorimeter clusters and calibrated to the electromagnetic energy scale. This uses the *AntiKt4EMTopoJets xAOD* jet collection. Jet energies are corrected for contributions from pile-up interactions using a jet-area based technique, and calibrated using p_T- and η-dependent correction factors determined from simulation, with residual corrections from in situ measurements applied to data and internal jet properties, referred to as the Global Sequential Calibration (GSC). This calibration is implemented using the *JetCalibrationTool* [59]. Jets are required to satisfy $p_T > 20$ GeV, $|\eta| < 2.5$ and the "jet cleaning" selection of Ref [60]. To reject jets from pile-up interactions, jets with $p_T < 60$ GeV and $|\eta| < 2.4$ are required to have a "Jet Vertex Tagger" value in excess of 0.59.

To avoid double counting, overlapping electrons, muons and jets are then removed according to the standard ATLAS procedure [61]. This is implemented using the *OverlapRemovalTool* [62]. The procedure is outlined as follows:

1. Any electron sharing an inner detector track with a muon is removed from the event.

2. Any jets within ΔR of 0.2 of electrons are removed.

3. Electrons within $min(0.4, 0.04 + 10 \text{ GeV}/p_T^{\text{electron}})$ of jets which satisfy $JVT > 0.59$, $p_T < 60$ GeV and $|\eta| < 2.4$ are removed.

4. Remove jets within ΔR of 0.2 of muons if the jets have less than three associated tracks, or if the muon has 70% of the associated track momentum and less than 50% of the jet momentum

5. Muons within $min(0.4, 0.04 + 10 \text{ GeV}/p_T^{\text{muon}})$ of jets passing $JVT > 0.59$, $p_T < 60$ GeV and $|\eta| < 2.4$ are removed.

At least two leptons are required to survive the overlap removal procedure, two of which must be same-flavour opposite-sign leptons. These are required to have an invariant mass compatible with the Z boson, $81 < m_{\ell\ell} < 101$ GeV. If multiple same flavour opposite sign lepton pairs mass these requirements, then the pairing with an invariant mass closest to that of the Z boson is chosen.

The three body system is then required to have an invariant mass passing a loose pre-selection requirement: $m_{j\ell\ell} < 250$ GeV. This variable is used to form the regions from which the background is estimated, thus the large high side window is to allow sufficient background to determine the background normalisation

from data. Many events contain multiple jets which could be taken as the resonance candidate, in which case the jet with the highest p_T is chosen. This criteria correctly selects the resonance in 82.1% to 88.3% of cases for the 0-4 GeV a signal hypotheses, while not biasing the jet selection in such a way as to create a fake peak in the invariant mass of the three body system, as would be the case for a three body mass based selection. The fraction of events in which the correct jet was selected was also higher than with selecting the jet which gives a three body mass closest to 125 GeV.

Finally, the three body mass is required to be between 120 GeV and 135 GeV. This requirement was chosen to maximise the $S/\sqrt{B}$.

Kinematic distributions for the selected calorimeter jet are shown in Figure 2. Kinematic distributions for the leptons chosen to reconstruct the Z boson are shown Figure 3. Kinematic distributions for the reconstructed Z boson (the sum of the 2 lepton 4-momenta) are shown in Figure 4. Kinematic distributions for the reconstructed Higgs boson (the sum of the 2 lepton and the jet 4-momenta) are shown in Figure 5. Various event level angular distributions are shown in Figure 6.

The signal peak in Figure 5(b) is not centred on 125 GeV due to the calibration of the calorimeter jets used in the construction of this variable being designed for QCD jets, rather than the jets produced from the decay of one of these light resonances. This is demonstrated by Figure 7. The central value shifts and resolution of the three body mass peak degrades for high a masses, due to the presence of neutrinos from decaying charm-quarks and τ-leptons produced in the decay of the resonance.

3.2 Track Selection

Ultimately, a track-based discriminant will be used to separate the signal resonance from the background QCD jets. These tracks are selected by a method know as Ghost-Association [63], in which the tracks in the event are assigned a negligible p_T, and then the jet reconstruction algorithm is re-run, on both the calorimeter clusters (as per the original algorithm) and these new Ghost-tracks; any tracks clustered in the jet are considered Ghost-Associated to it.

The majority of tracks Ghost-Associated to the jet come from pileup, the underlying event, multiple parton interactions and fake tracks. This is demonstrated by using the track to truth particle link provided in the *xAOD* to identify the generator-level particle responsible for the track, and then following the truth record upwards to see if the particle originated from a decay of the signal resonance. The p_T distributions of the tracks Ghost-Associated to the calorimeter jet, with and without truth matching, are shown in Figure 8. The p_T distributions of the tracks which are not truth matched to the signal resonance follow that of pileup, while the signal events have a significantly higher p_T spectrum. This lower p_T spectrum in fakes means that most of the variables constructed from these tracks, which are dependant on the p_T of the jet, are somewhat resilient to change from the addition of fake tracks.

In order to reject the large contamination from fake tracks, the ATLAS *Loose* Track Quality and *Loose* track-to-vertex association (TTVA) requirements are applied, which are implemented using the *InDetTrackSelectionTool* [64] and *TrackVertexAssociationTool* [65], respectively. The *Loose* Track Quality working point requires that the track has $p_T > 500$ MeV, $|\eta| < 2.5$, at least 7 silicon hits, at most one shared module, at most 1 hole in the pixel, and at most 2 holes in the pixels or strips. The *Loose* TTVA working point requires that $|d_0| < 2$ mm and $|\Delta z_0 sin\theta| < 3$ mm, where d_0 and z_0 are the transverse and longitudinal impact parameters, respectively. The effect of this requirement on the track assisted mass are shown in Figure 9. The track assisted mass is defined as the mass of the track system multiplied by the ratio of the
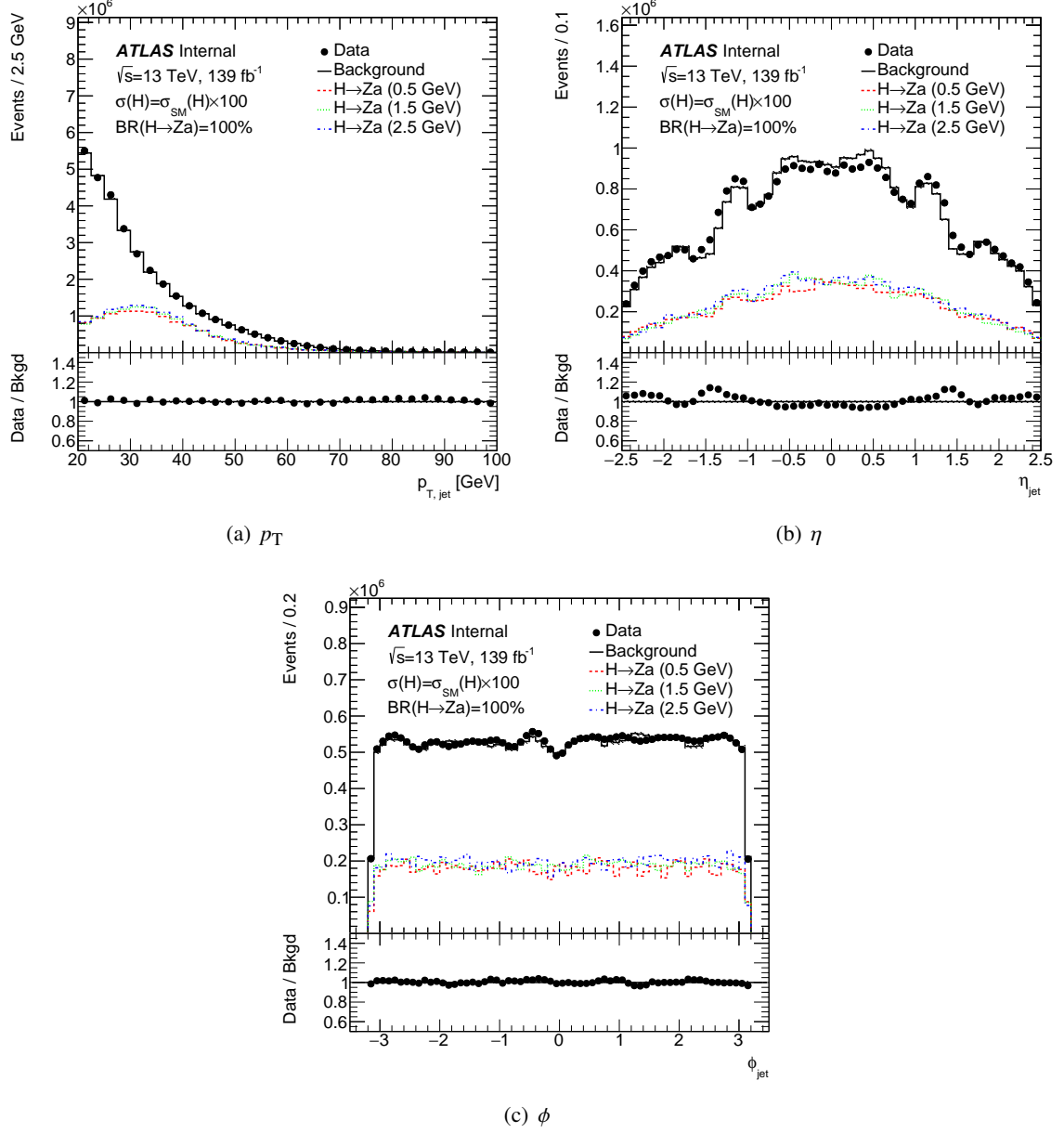
(a) p_T

(b) η

(c) ϕ

Figure 2: Kinematic distributions of the leading jet in the event, after the full event-level pre-selection. Data, signal and background distributions are shown. The background in these distributions has been reweighted as per Section 4.2.1.

Figure 3: Kinematic distributions of the leptons used to reconstruct the *Z* boson, after the full event-level pre-selection. Data, signal and background distributions are shown. Note the 18 GeV lepton requirement from the *FTAG2* derivation. The background in these distributions has been reweighted as per Section 4.2.1.

(a) p_T

(b) m

(c) η

(d) ϕ

Figure 4: Kinematic distributions of the reconstructed Z boson (the sum of the 2 lepton 4-momenta) in the event, after the full event-level pre-selection. Data, signal and background distributions are shown. The background in these distributions has been reweighted as per Section 4.2.1.
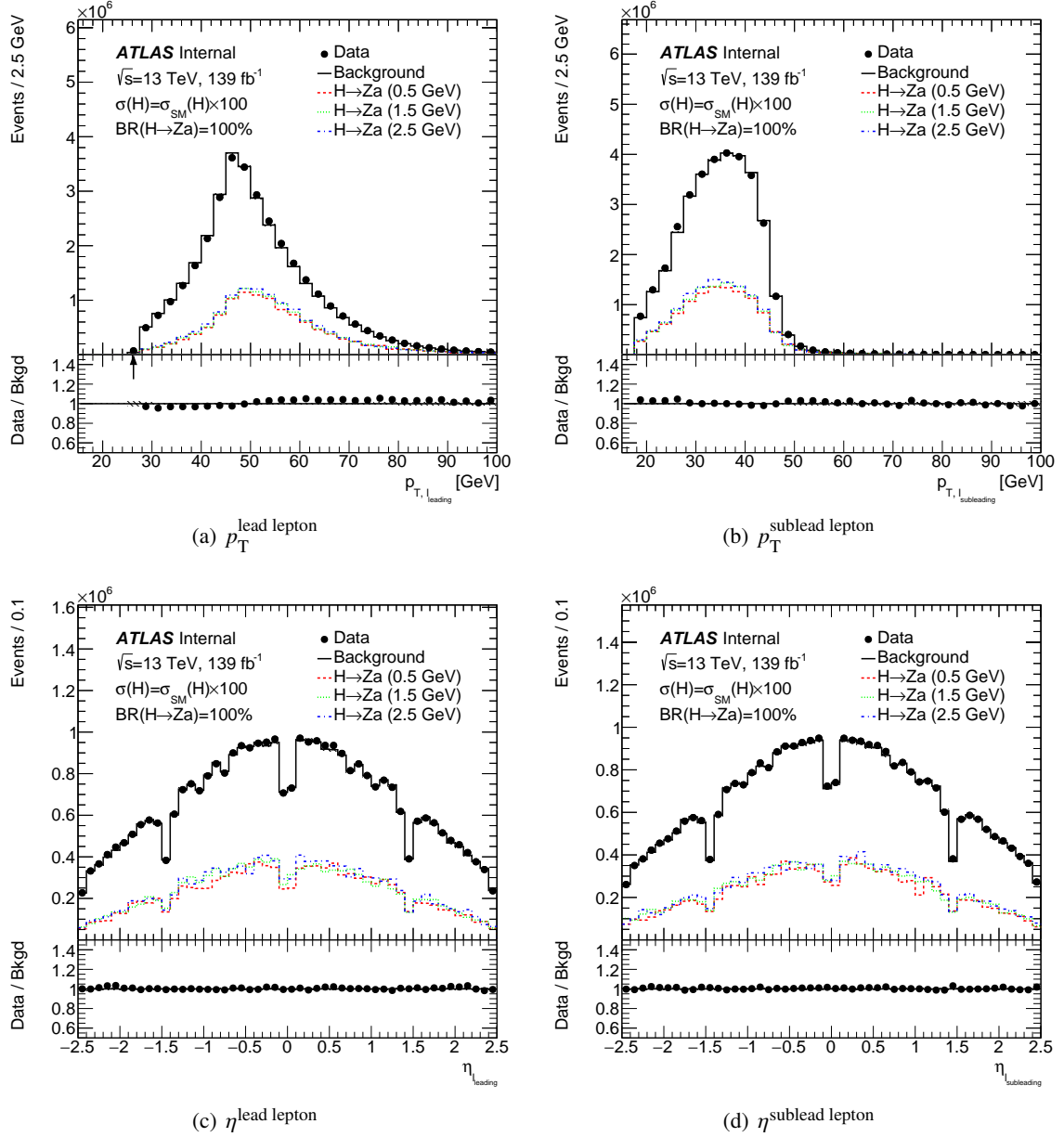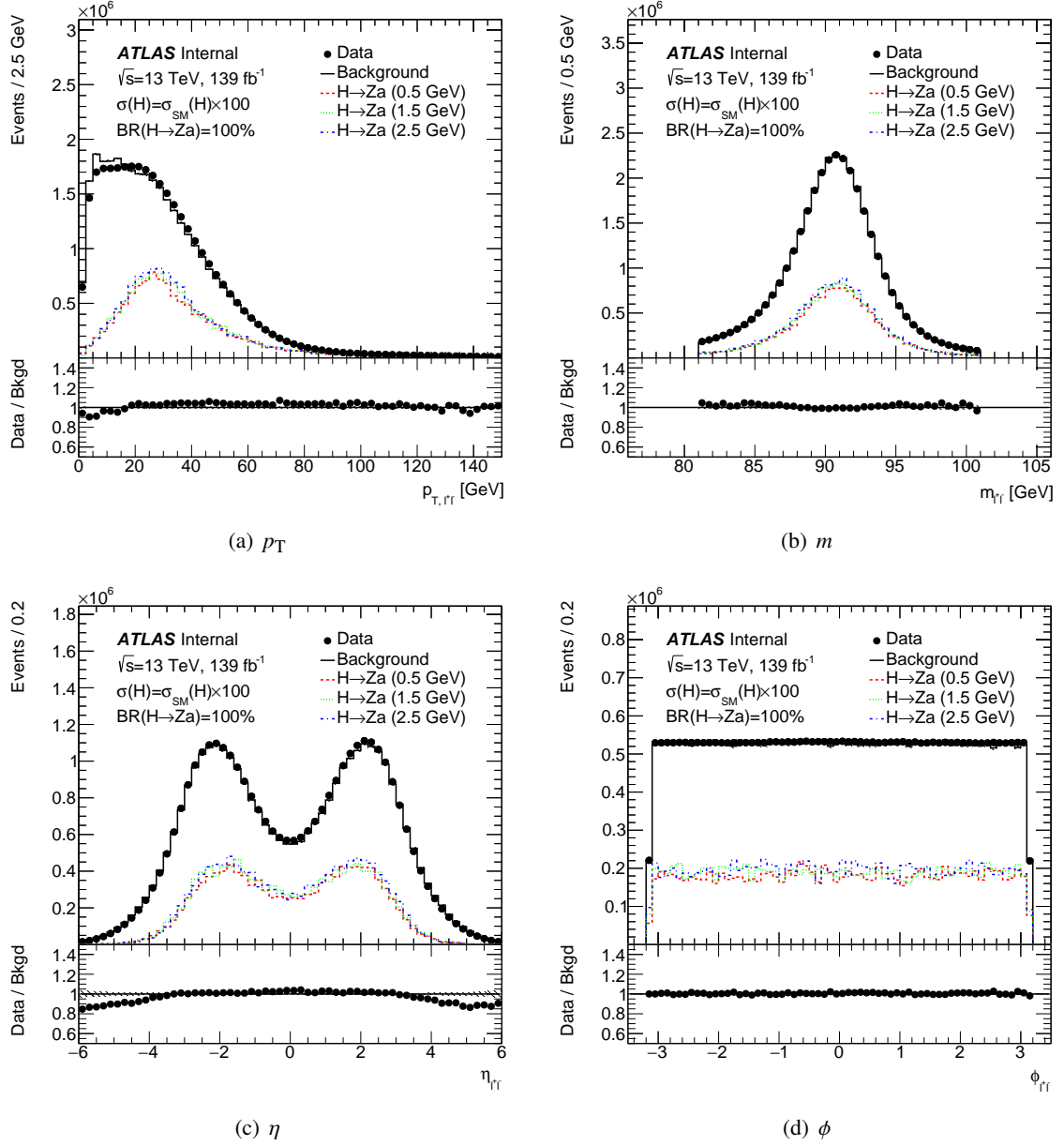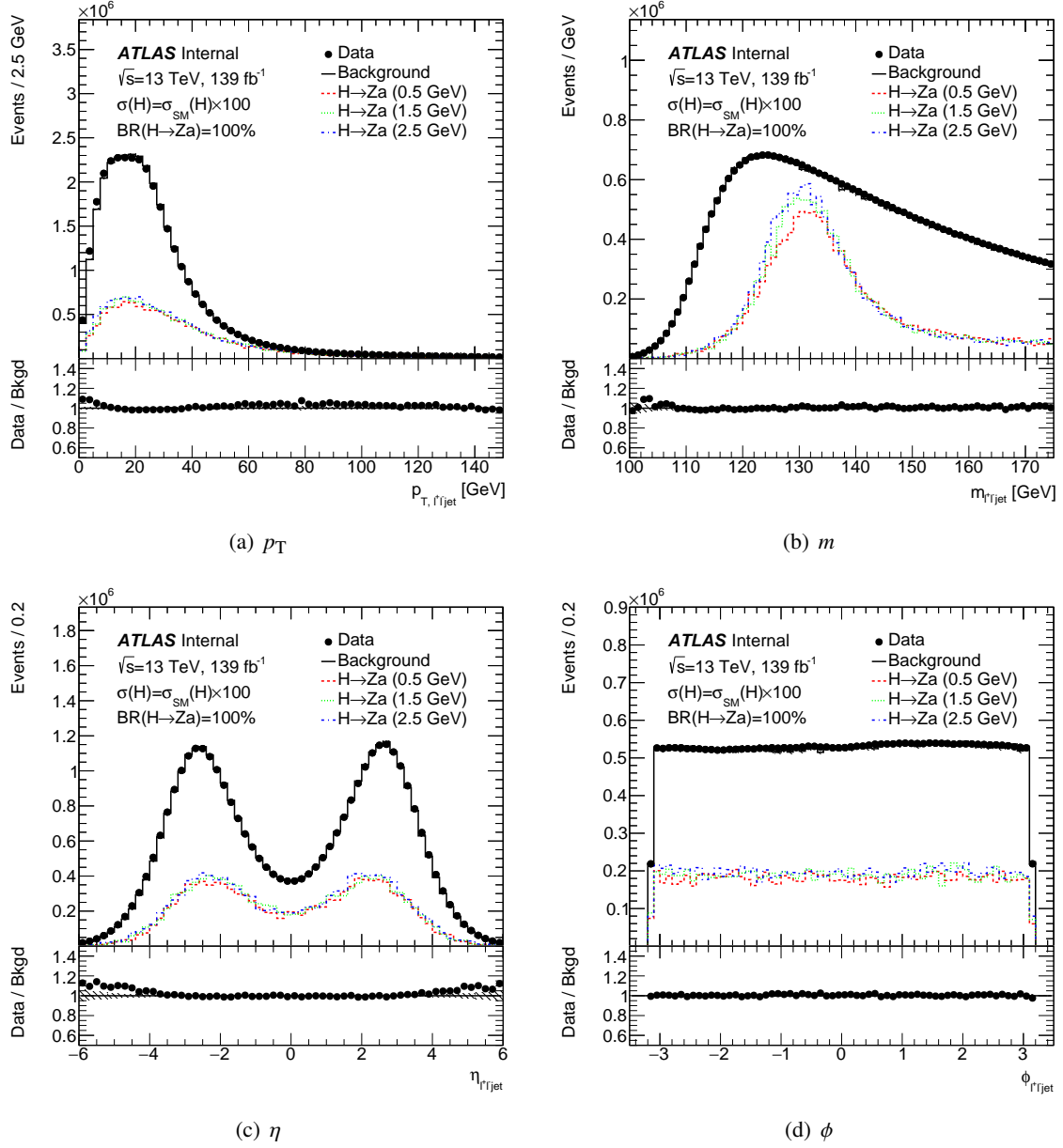
Figure 5: Kinematic distributions of the reconstructed Higgs boson (the sum of the 2 lepton and calo jet 4-momenta) in the event, after the full event-level pre-selection. Data, signal and background distributions are shown. The background in these distributions has been reweighted as per Section 4.2.1.

(a) $\mathrm{Max}(\Delta R^{\ell^-\mathrm{jet}}, \Delta R^{\ell^+ jet})$

(b) $\mathrm{Min}(\Delta R^{\ell^-\mathrm{jet}}, \Delta R^{\ell^+}\mathrm{jet})$

(c) $\Delta R^{\ell^-\ell^+}$

(d) $\Delta R^{Z\mathrm{jet}}$

Figure 6: Event level angular (ΔR) distributions between the various objects in the event, after the full event-level pre-selection. Data, signal and background distributions are shown. The background in these distributions has been reweighted as per Section 4.2.1.
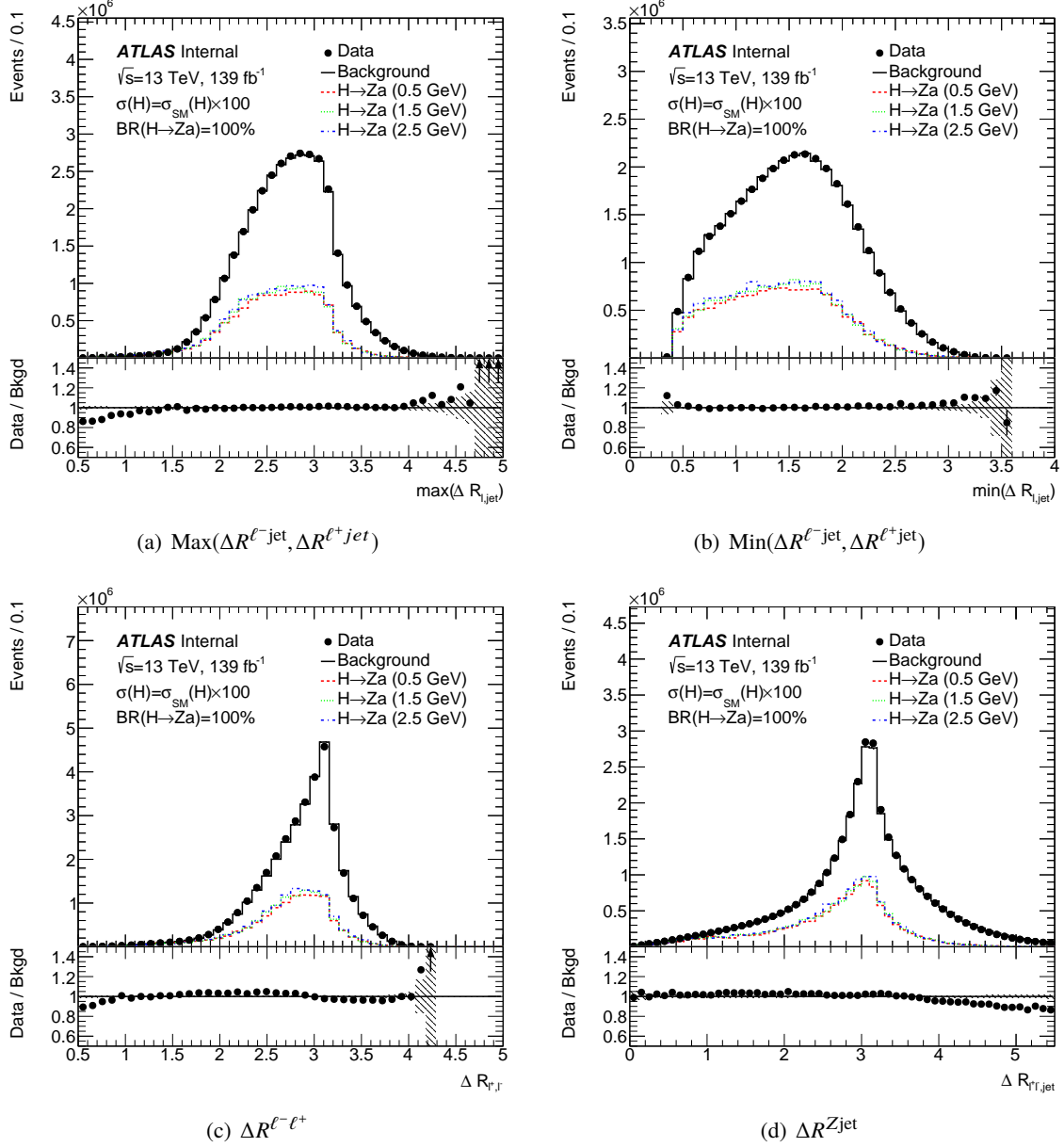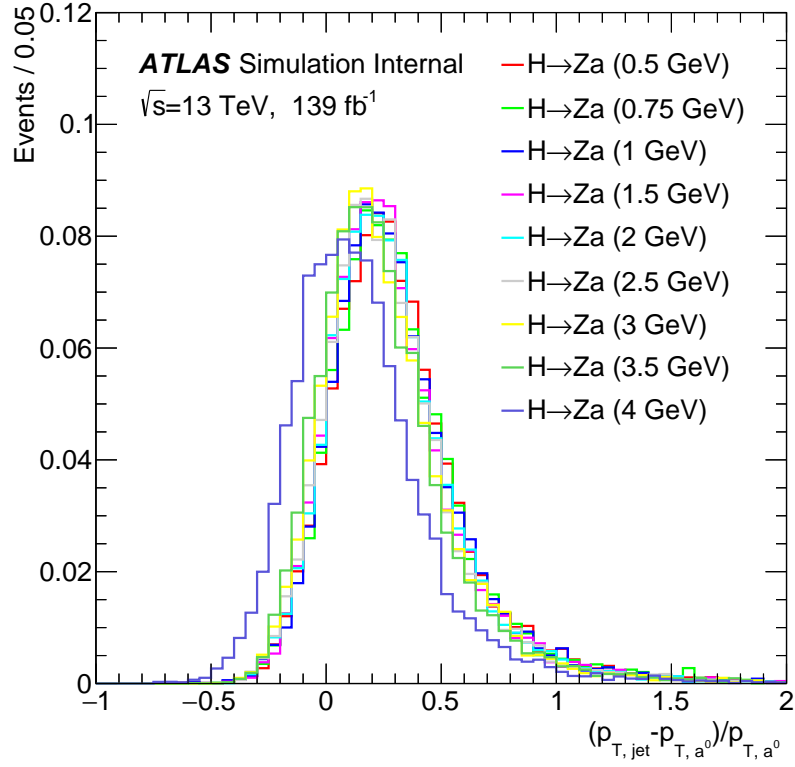
Figure 7: $(p_{T,\,\text{calo jet}} - p_{T,\,a})/p_{T,\,a}$ distribution.

(a) Generator-Level Matched

(b) Generator-Level Anti-Matched
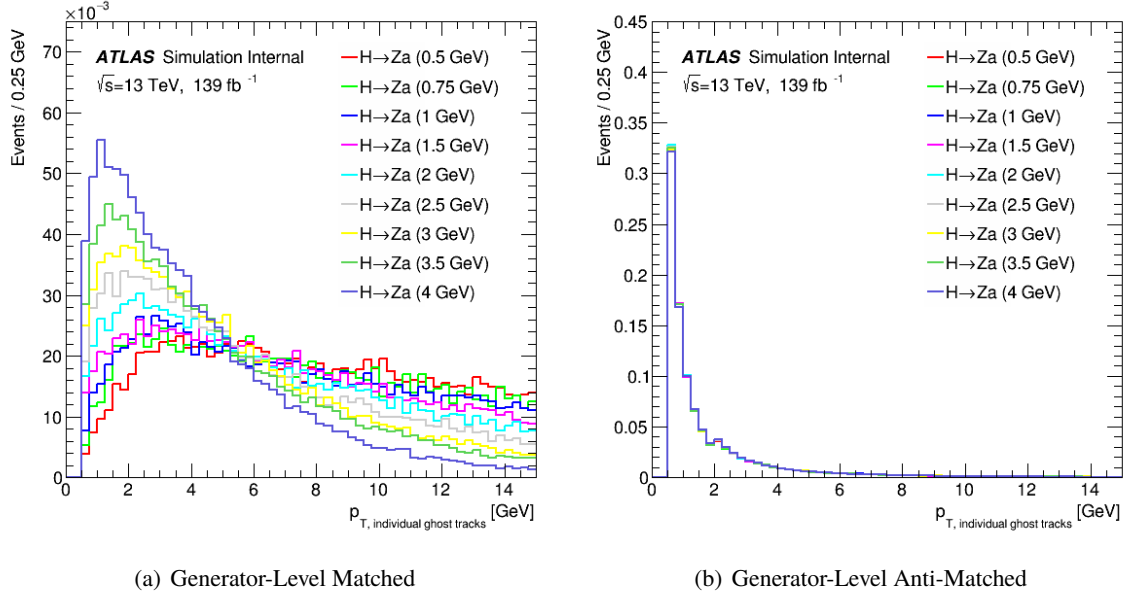
Figure 8: p_T distributions of the tracks Ghost-Associated to the calorimeter jet, with and without truth matching. Only signal distributions are shown here.

p_T of the jet as measured in the calorimeter and tracker. This is not used later in the analysis, but provides a reasonable proxy for the mass, which illustrates the effectiveness of the track-selection.

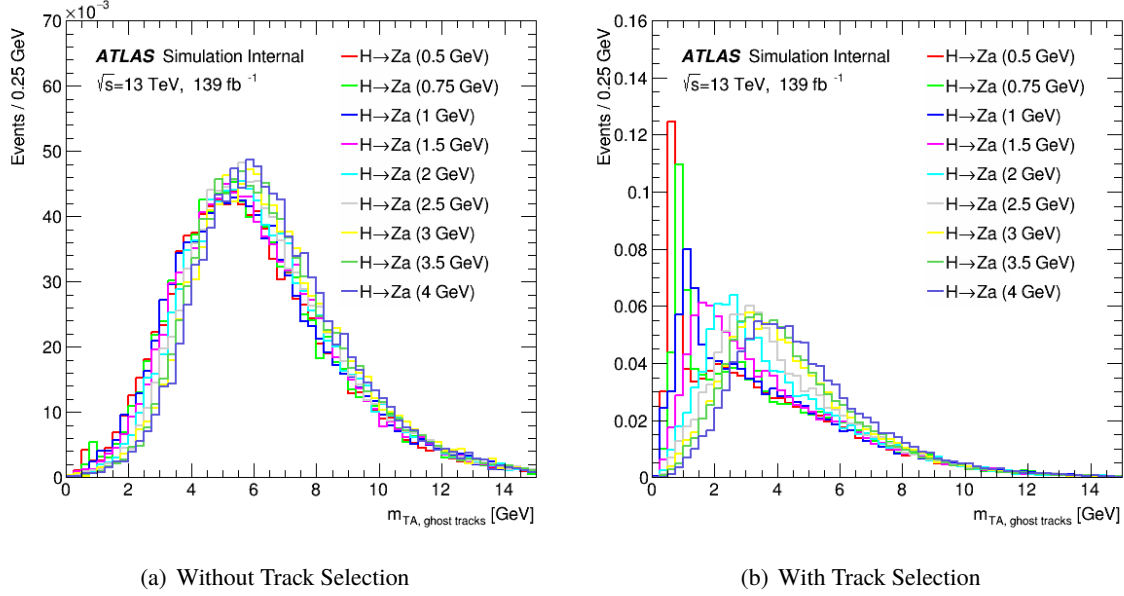(a) Without Track Selection   (b) With Track Selection

Figure 9: Track assisted mass distributions of the calorimeter jet, before and after the *Loose* TTVA and track selection requirements. Data, signal and background distributions are shown.

The resulting discriminant (Section 3.3) relies on there being multiple tracks Ghost-Associated to the jet. As such, any events in which the selected jet has less than two Ghost-Associated tracks which passing the requirements detailed in this section are discarded.

3.3 Track-Based Multi-Layer-Perceptron

A multi-layer perceptron (MLP) is used to discriminate between jets arising from hadronic X decays, and background multijet production. TMVA is used to train the MLP. As these are thin ($R = 0.4$) jets, the information from the inner tracker is expected to be more useful due to the improved angular and p_T resolution. The reconstruction and modelling of the tracks are also better understood than that of the calorimeter objects. We therefore use the set of Ghost-Associated tracks, selected as per subsection 3.2, as the basis for the inputs variables to this MLP.

Variables defined on these tracks are selected based on their ability to separate the various signals from the total background. These variables are summarised in Table 5, briefly described in the next paragraph, and displayed in Figures 10, 11, and 12. These variables are chosen to be dimensionless in order to reduce their correlation with event-level kinematic quantities; also minimising the correlation between the MVA output and the event-level kinematic quantities. The correlation coefficient between each of these variables and the three body mass is also shown in Table 5, with none having a correlation greater than 20%. What correlation remains between the three body mass and these variables occurs primarily through the transverse momentum of the calorimeter jet.

$p_T^{\text{lead track}}/p_T^{\text{tracks}}$ is the ratio of transverse momentum of the highest p_T track to transverse momentum of the Ghost-Associated track system. $\Delta R^{\text{lead track, calo jet}}$ is the angular separation (ΔR) between the highest

Variable	Description	$m_{\ell\ell j}$ Correlation
$p_T^{\text{lead track}} / p_T^{\text{tracks}}$	Ratio of transverse momentum of the leading track to total	7.5%
$\Delta R^{\text{lead track, calo jet}}$	ΔR between the leading track and the calorimeter jet axis	19.6%
τ_2	NSubJettiness 2 [66]	1.0%
$U_1(0.7)$	Modified energy correlation function (2, 1, 0.7) [67]	9.4%
$M_2(0.3)$	Ratio of modified energy correlation functions (3, 1, 0.3) and (2, 1, 0.3) [67]	12.5%
$angularity(2)$	Angularity 2 [68]	13.4%

Table 5: Variables chosen to discriminate the resonance signals from the combined background. All tracks have been Ghost-Associated to the calorimeter jet as per subsection 3.2. The Pearson correlation coefficient between each of these variables and the three body mass is shown in the last column for the background.

(a) $p_T^{\text{lead track}} / p_T^{\text{tracks}}$
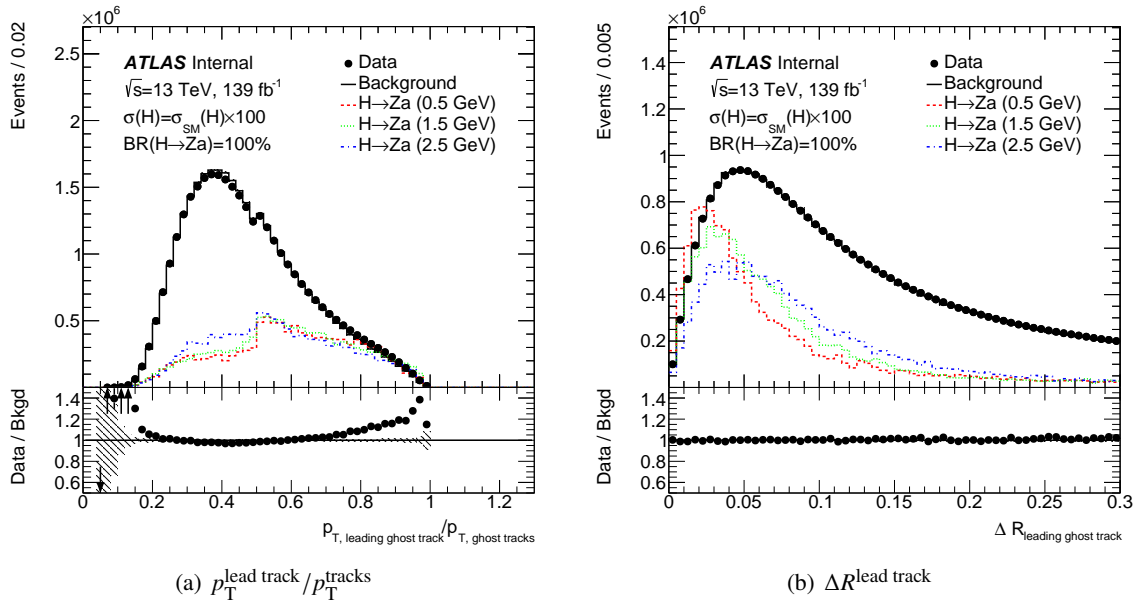
(b) $\Delta R^{\text{lead track}}$

Figure 10: MLP input distributions based on the leading track Ghost-Associated to the jet, after the full event-level pre-selection. Data, signal and background distributions are shown. The background in these distributions has been reweighted as per Section 4.2.1.

(a) $U1(0.7)$

(b) $M2(0.3)$
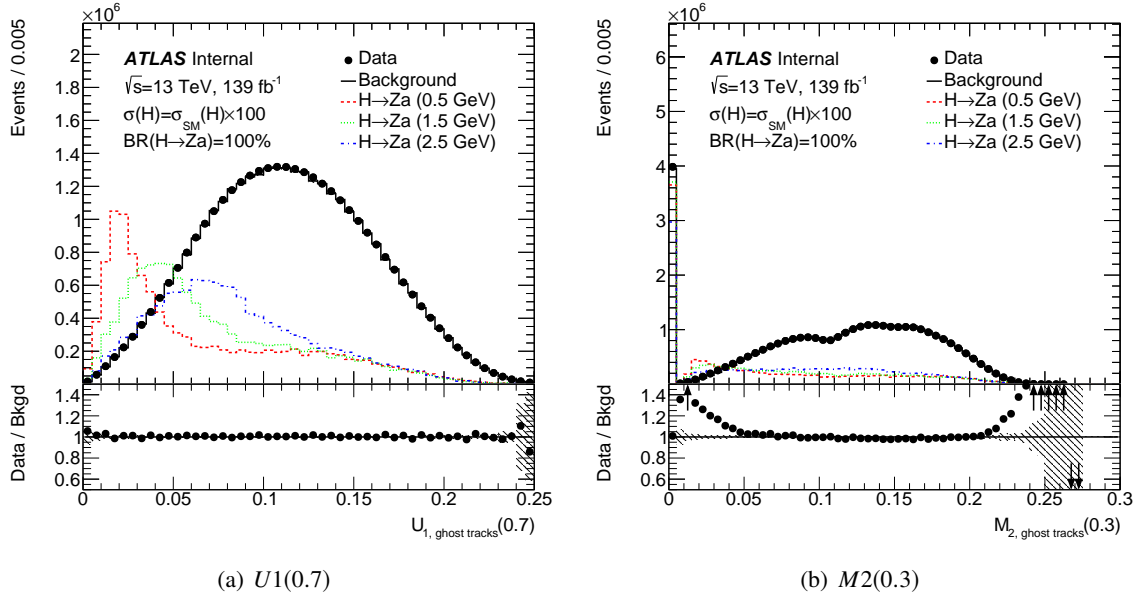
Figure 11: MLP input distributions based on the modified correlation functions, after the full event-level pre-selection. Data, signal and background distributions are shown. The background in these distributions has been reweighted as per Section 4.2.1.
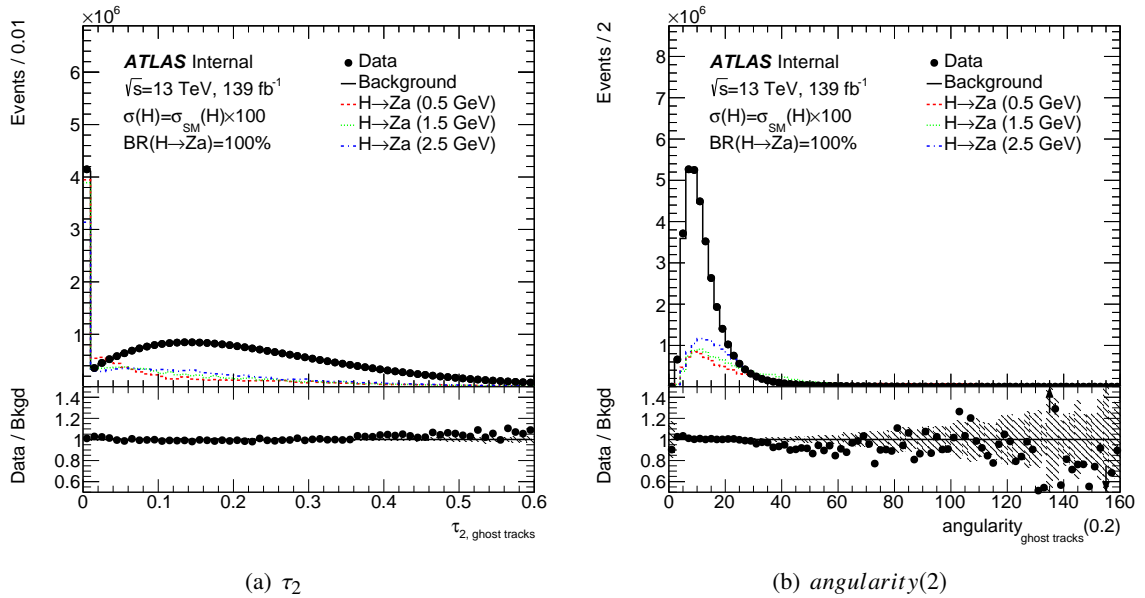

(a) τ_2

(b) $angularity(2)$

Figure 12: MLP input distributions based on the NSubJettiness and angularity variables, after the full event-level pre-selection. Data, signal and background distributions are shown. τ_2 is defined to be 0 for less than three tracks. The background in these distributions has been reweighted as per Section 4.2.1.

p_T track and the calorimeter jet axis. τ_2 is the NSubJettiness 2 variable [66], where NSubJettiness is a measure of how well the jet can be described in terms of two sub-jets. It is used due to the fact that most of the decays of the resonances of interest are to pairs of final state partons. It is defined as $\tau_2 = \Sigma_t p_{T,t} \min(\Delta R_{1,t}, \Delta R_{2,t})/\Sigma_t p_{T,t} R_0$, where the sums run over the Ghost-Associated tracks, the angles $\Delta R_{i,t}$ are between the track and one of two subjets, and R_0 is the radius parameter of the larger jet (0.4). The two subjets are chosen using the exclusive k_T sub-jet algorithm [66]. $U_1(0.7)$ and $M_2(0.3)$ are both modified energy correlation functions [67], designed for quark-gluon discrimination and to target 2-pronged substructure, respectively. $U_1(0.7) = {}_1e_2^{(0.7)}$ and $M_2(0.3) = {}_1e_3^{(0.3)}/{}_1e_2^{(0.3)}$, where ${}_1e_2^{(\beta)} = \Sigma_{1 \leq i < j \leq n} z_i z_j \theta_{ij}^\beta$ and ${}_1e_3^{(\beta)} = \Sigma_{1 \leq i < j < k \leq n} z_i z_j z_k \min(\theta_{ij}^\beta, \theta_{ik}^\beta, \theta_{jk}^\beta)$, and z_i is the ratio of the p_T of the track, to that of the track system. Lastly, $angularity(2)$ is an angularity variable, defined analogously to Ref. [68] as $angularity(2) = \Sigma_t p_{T,t} \sin^2(\pi\theta_t/2R_0)(1 - \cos(\pi\theta_t/2R))^{-1}$. The form of this variable is motivated by the different matrix elements for resonance- and QCD-induced jets, as detailed in Ref. [68].

This is not a typical classification task, as there is a continuous spectrum of signals being classified against a large background distribution. As such, before being given to a classification algorithm, the input variables are first given to a regression multi-layer-perceptron in TMVA. This MLP is trained on the 0.5, 0.75, 1, 1.5, 2, 2.5, 3, 3.5 and 4 GeV a signal samples, and is designed to estimate the mass of the a based on the input variables. Only events with $100 < m^{\ell\ell j} < 170$ GeV were used. It uses the default TMVA hyper-parameter values, and an architecture of 4 layers of 12 neurons. These default hyper-parameters are: NCycles=500, NeuronType=sigmoid, EstimatorType=Mean Square Estimator, NeuronInputType=sum, TrainingMethod=Back-Propagation, LearningRate=0.02, DecayRate=0.01, and TestRate=10. Negative weight events are ignored in the training of the MLPs. This regression is then given, along with the original input variables, to a classification MLP. This way, the classifier has been indirectly informed that it is searching for a spectrum of signals, rather than just a single signal; and it has some information with which to estimate which signal it is looking at in the event of a signal being present in the data. Various other architectures and hyper-parameters were tried, and these were found to be optimal. The regression output variable is shown in Figure 13.

This output variable of the regression MLP is then given, along with the original input variables, to a classification MLP. This MLP uses the default TMVA hyper-parameters (listed in the previous paragraph), and an architecture of 2 layers of 6 and 5 neurons, to separate the background from the sum of the following signals: 0.5, 1, 1.5, 2, 2.5, 3, 3.5 and 4 GeV a signal samples. As with the regression MLP, various other architectures and hyper-parameters were tried, and these were found to be optimal. Also as with the regression MLP, only events with $100 < m^{\ell\ell j} < 170$ GeV were used. The 0.75 GeV a signal sample was removed from the training because it was found to bias the classifier towards lower mass signal samples, resulting in a deterioration of the performance towards higher masses. The classification output variable is shown in Figure 14, and the ROC curves for the testing and training events are given inclusively in Figure 15, and separately in Figure 16. The ROC curves show good signal to background discrimination (average $\sim 50\%$ signal efficiency for $\sim 90\%$ background rejection), as well as little-to-no overtraining.

The design of this MVA was assisted, and concepts validated, by the use of PYTHIA8 MC samples, with a DELPHES [69] detector simulation using the ATLAS card. Signal samples were produced with a masses of: 0.4, 0.5, 0.75, 0.8, 1, 1.2, 1.5, 1.6, 2, 2.4, 2.5, 2.8, 3, 3.2, 3.5, 3.6 and 4 GeV. Each signal sample had 100k signal events, and 20M Z+jets background events were simulated. These samples were not used in any of the results in this note directly, but were used to test the concepts which were then implemented using the nominal MC samples.

MLPs were used as the chosen MVA because they showed good interpolation potential. This was tested
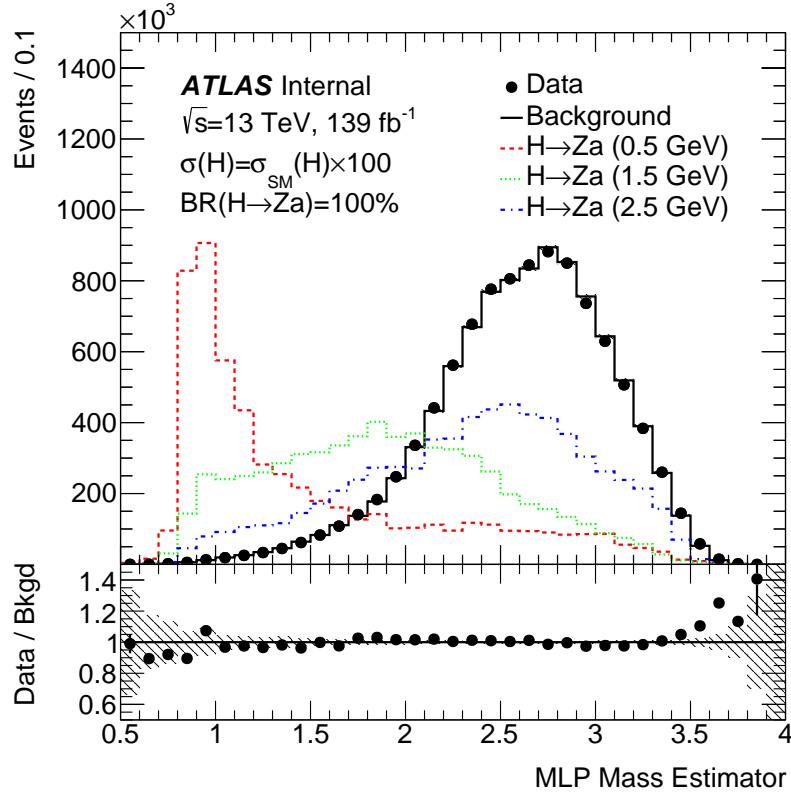
Figure 13: Output of the regression MLP, for data, background and three signal hypotheses. Events are required to pass the complete event selection, including the 120 GeV $< m_{\ell^+\ell^- j} <$ 135 GeV requirement, but not the requirement on the classification MLP output variable. The background normalisation is set equal to that of the data, and the signal normalisations assume the SM Higgs production cross section and $\mathcal{B}(H \rightarrow Za) = 100\%$ with the signal normalisation is scaled up by a factor of 100. The background in these distributions has been reweighted as per Section 4.2.1. The error bars are the data statistical uncertainty, and the dashed bars are the MC statistical uncertainty.

using both DELPHES- and GEANT4-based MC by removing a signal sample from the training of the MVA, and comparing the performance of the MVAs, with and without the exclusion of this signal sample in the training, on this signal sample. Removing the 2.2 GeV a mass DELPHES sample, the MLP was found to have an $S/\sqrt{B}$ 11% lower than with the sample included in the training. This is to be compared to a 30% loss in $S/\sqrt{B}$ improvement for a boosted decision tree (BDT) with the 2.2 GeV a mass removed from the training, showing that the BDT looses much more performance when interpolating to mass points for which is was not trained. The MLP also showed greater overall performance and less overtraining as compared to the BDT.

A single requirement on the resulting MLP is then used to reject background events. The requirement is chosen to maximise $S/\sqrt{B}$, as this minimises the uncertainty on the signal strength, and the limit, in the high stats limit. However, as there are multiple signal samples, the cut is chosen to maximise the average $S/\sqrt{B}$, with each signal sample given a weight. This weight is calculated as the a mass phase space which it represents, i.e. the phase space which is closest to that mass hypothesis. For example, for the 1.5 GeV a signal sample, because there is also a 1 GeV and 2 GeV a signal sample, it represents 0.5 GeV of phase space. This also maximises the expected $S/\sqrt{B}$, assuming a flat Bayesian prior on the signal mass. This results in an MLP cut at 0.0524, which results in a background efficiency of 1.01% for
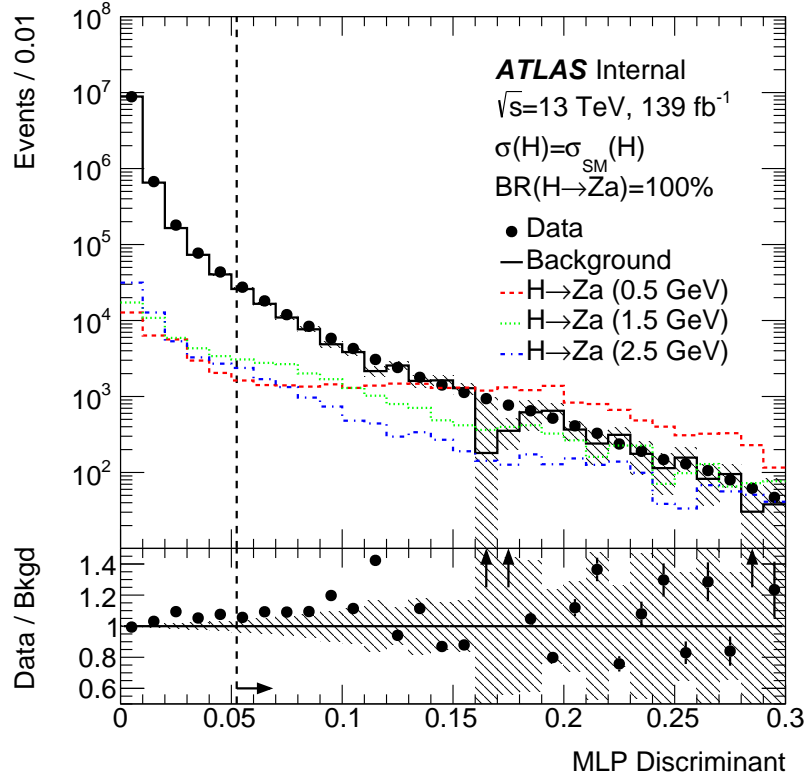
Figure 14: Output of the classification MLP, for data, background and three signal hypotheses. Events are required to pass the complete event selection, including the 120 GeV $< m_{\ell^+\ell^-\mathrm{j}} < 135$ GeV requirement, but not the requirement on the classification MLP output variable. The background normalisation is set equal to that of the data, and the signal normalisations assume the SM Higgs production cross section and $\mathcal{B}(H \to Za) = 100\%$. The background in these distributions has been reweighted as per Section 4.2.1. The error bars are the data statistical uncertainty, and the dashed bars are the MC statistical uncertainty. The region to the right of the dashed line is the signal region.

110 GeV $< m^{\ell\ell\mathrm{j}} < 170$ GeV, and signal efficiencies as given in Table 6. The inclusion of the regression output variable in the classification MVA was found to result in an improvement in $S/\sqrt{B}$ of 13%, when averaged across the signal samples with an $S/\sqrt{B}$ gain due to the MLP greater than unity. The MLP efficiency for the 8 GeV a signal sample is less than that for the background because the MLP was trained to target the lower masses, for which the analysis is most sensitive. However, this is not an issue because the analysis will only target a with masses below 4 GeV.

The performance of the MLP is then tested on both the testing and training samples to check for overtraining. No statistically significant overtraining is seen in any of the signal or background samples. Considering background events with 100 GeV $< m^{\ell\ell\mathrm{j}} < 175$ GeV, 3100 more events from the training sample than the validation sample pass the MLP cut. This is the opposite of what would be expected if overtraining were present, though it is consistent with equality within 0.42 times the statistical uncertainty. Taking the 1.5 GeV signal sample as an example, and considering events with 100 GeV $< m^{\ell\ell\mathrm{j}} < 175$ GeV, 43 more events from the training sample than the validation sample pass the MLP cut. This is consistent with equality within 0.48 times the statistical uncertainty.
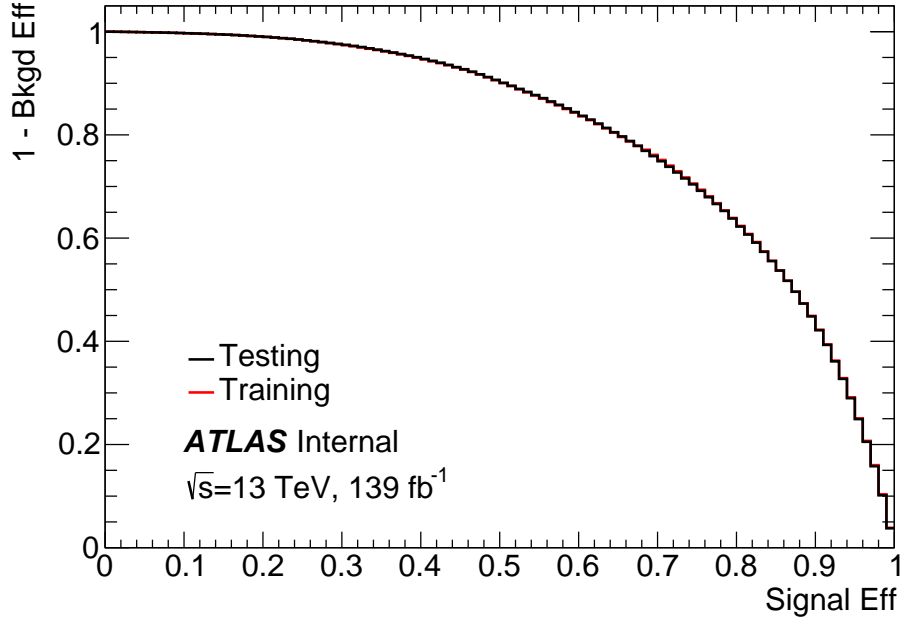
Figure 15: ROC curves for the testing events and the training events.

a mass / GeV	MLP Eff (%)	MLP $S/\sqrt{B}$ Gain
0.5	45.9 ± 0.8	5.26
0.75	42.1 ± 0.8	4.83
1	38.2 ± 0.7	4.38
1.5	31.5 ± 0.6	3.61
2	25.1 ± 0.5	2.87
2.5	15.4 ± 0.4	1.76
3	8.06 ± 0.29	0.924
3.5	5.70 ± 0.24	0.653
4	1.88 ± 0.15	0.216
η_c	5.89 ± 0.24	0.675
J/ψ	6.66 ± 0.26	0.763

Table 6: Efficiencies of the $MLP > 0.0524$ requirement on each signal sample. This requirement results in a background efficiency of $(0.761 \pm 0.020)\%$ for 120 GeV $< m^{\ell^+\ell^- j} < 135$ GeV. The $S/\sqrt{B}$ gains are defined as the ratio of the $S/\sqrt{B}$ after the MLP selection to before the MLP selection. Pythia8 a BRs are assumed, using the default BSMHiggs $\tan\beta$ value of 1, as given in Table 3.
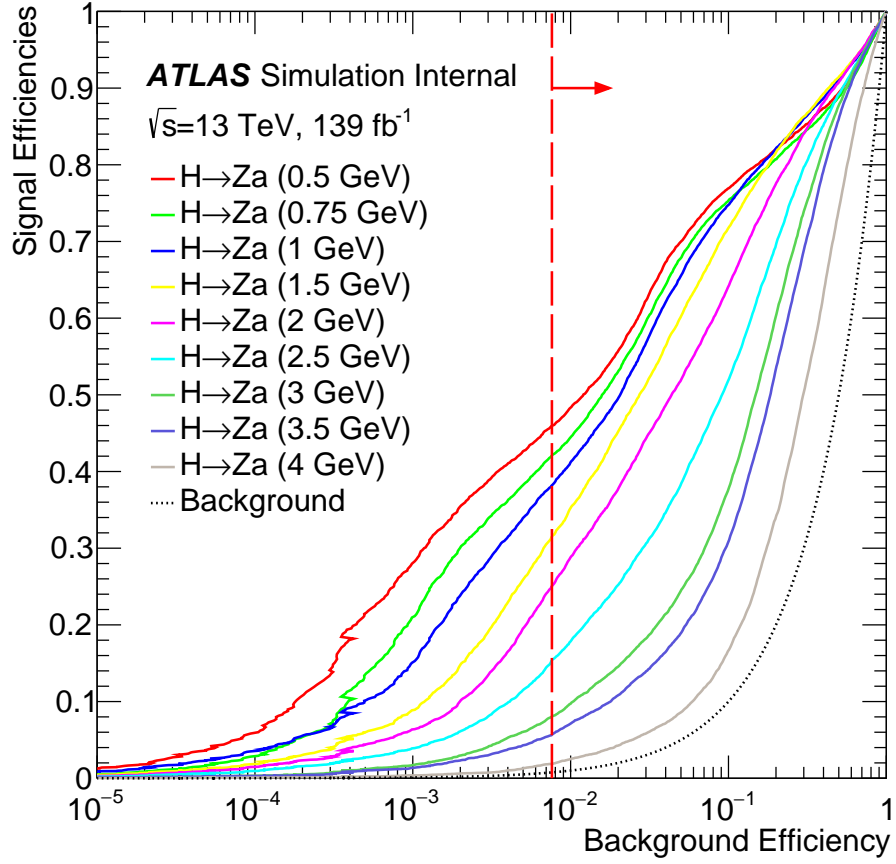
Figure 16: ROC curves for the individual signal samples, with the background curve given for reference.

3.4 Full Selection

The full selection is summarised in Table 7, and a cutflow is provided in Appendix K.

Cut	Details
Triggers	Single lepton triggers requiring $p_T > 27$ GeV
Leptons	e or $\mu \geq 2$ with $p_T > 18$ GeV
Z boson	2 same-flavour opposite-sign leptons, with $|m^{ll} - m_Z| < 10$ GeV and $p_T^{lead} > 27$ GeV
Select X-candidate as anti-k_T 4 topo EM jet ($p_T^{jet} > 20$ GeV), with highest p_T, for which $m^{llj} < 250$ GeV	
> 2 tracks	≥ 2 tracks ghost associated to the calo jet, surviving track selection
Higgs boson	120 GeV $< m^{llj} < 135$ GeV
MLP	$MLP > 0.0524$

Table 7: Summary of full event selection.

3.5 Generator-Level Acceptance

To quantify the kinematic acceptance of this analysis to the different signal hypotheses under consideration, a generator-level acceptance is optimised to be independent of the detector performance. This selection closely follows the requirements of the full selection described in subsection 3.4, but without the requirements placed on the track system, the MLP requirements, or the three body mass. This results in a generator-level acceptance which varies between 27% and 29% for the various signal hypotheses. The efficiency of the full (and fully reconstructed) selection efficiency, with these cuts relaxed varies between 16% and 21% for the various signal hypotheses. Thus the efficiency of the detector for signal events falling within its acceptance is approximately 65%.

4 Signal and Background Modelling

4.1 Signal Modelling

The signal efficiency for the selection is taken directly from MC. This scales the expected Higgs production yield, taken as the product of the luminosity (139 fb^{-1}) and the total SM Higgs production cross section (55.7 pb)[2]. The contributions to the total cross section are taken from the LHC Higgs Cross Section Working Group [70]. The total Higgs production cross section is taken as the sum of gluon fusion, vector boson fusion, ZH, WH, $b\bar{b}H$, $t\bar{t}H$ and tH associated production. This is scaled by the branching fraction of the Z boson to electrons, muons or tau-leptons, which is taken from the Particle Data Group to be 10.1% [71]. Finally, this is scaled by the signal strength: $\mu = \sigma(H)\text{BR}(H \rightarrow Za)/\sigma_{\text{SM}}(H)$, to give the total number of expected signal events, assuming the default PYTHIA branching ratios given in Table 3. μ is left free in the likelihood fit, as described in the subsection 6.1. Table 8 shows the expected signal yields for each of the signal hypotheses considered, assuming $\mu = 1$.

a mass / GeV	Total Efficiency (%)	Total Yield (1000×)
0.5	3.27 ± 0.06	25.6 ± 0.4
0.75	2.76 ± 0.05	21.6 ± 0.4
1	2.86 ± 0.05	22.4 ± 0.4
1.5	2.50 ± 0.05	19.5 ± 0.4
2	2.00 ± 0.04	15.7 ± 0.3
2.5	1.30 ± 0.03	10.2 ± 0.3
3	0.692 ± 0.025	5.41 ± 0.20
3.5	0.505 ± 0.021	3.95 ± 0.17
4	0.140 ± 0.011	1.09 ± 0.09
η_c	0.545 ± 0.022	4.26 ± 0.17
J/ψ	0.560 ± 0.022	4.37 ± 0.17

Table 8: Efficiencies of the full selection (pre-selection and MLP requirement) and total expected signal yields (assuming $\mu = 1$) for each signal sample. PYTHIA8 a BRs are assumed, using the default BSMHIGGS tan β value of 1, as given in Table 3.

4.2 Background Modelling

A semi data-driven background model is used to estimate the SM background content in the signal region (SR), using three steps. First, the simulated background is reweighted to match the data to improve the modelling of key variables. Second, a fully data-driven ABCD estimate of the background in the SR is produced, which assumes no correlation between the three body mass and the MLP output variable. Third, the reweighted MC is used to correct the data-driven ABCD estimate for the correlation between the three body mass and the MLP output variable. Finally, this background estimation method is compared to data in 13 validation regions.

---

[2] While the full inclusive Higgs production cross section is used in the normalisation, the MC samples were generated using the ggF production mode. A systematic uncertainty, described in Section 5.1.6, is ascribed to account for this difference.

4.2.1 Simulated Background Reweighting

Before being used to construct the background estimate, the simulated data is reweighted to improve the modelling in the key variables used in the ABCD estimate correction. These variables are the three body mass, and the MLP output variable. The modelling of the MLP output variable is improved by improving the modelling of the input variables. All of the variables are reweighted against data in a blinded data region, consisting of the events passing the full selection except either the Higgs mass or the MLP requirements, but not passing both $110 < m_{\ell\ell j} < 155$ GeV and the MLP requirement.

It was observed that the three body mass is well modelled for each given number of ghost-associated tracks. Therefore, the mismodelling in the three body mass distribution is entirely due to the mismodelling in the ghost-associated track multiplicity. Hence, the ghost-associated track multiplicity is reweighted against data to improve the three body mass distribution.

Reweighting the simulated data based on the $U_1(0.7)$ variable was observed to improve the modelling of the other track-based substructure variables input to the MLP. In doing so, this improves the modelling of the regression and classification MLP output variables. However, this introduces a mismodelling in the p_{T} distribution of the calorimeter jet and the ghost-associated track multiplicity, and thus in the three body mass.

To simultaneous improve the modelling in both the three body mass, and the MLP output variable, a fully-correlated 3D reweighting is applied based on n_{tracks}, $U_1(0.7)$, and $p_{\mathrm{T}}^{\mathrm{jet}}$. The reweighting is performed by applying corrections derived from the ratio of 3D histograms in data and background MC. Each value of n_{tracks} between 2 and 6 has a dedicated bin in the reweighting, events with n_{tracks} of 7 or 8 share a bin, and events with $n_{\mathrm{tracks}} \geq 9$ share a bin. The $U_1(0.7)$ range 0 to 0.25 is split into 25 equal bins 0.01 wide, and one overflow bin is used for events with $U_1(0.7) > 0.25$. The $p_{\mathrm{T}}^{\mathrm{jet}}$ region between 20 GeV and 50 GeV is split into 6 bins 5 GeV wide, the region 50 GeV to 60 GeV represents another bin, and the region above 60 GeV represents a final overflow bin. These three distributions before and after the reweighting procedure is applied are shown in Figure 17. This results in significant improvements to the modelling of the three body mass, the MLP input variables and the MLP output variables, as shown in Figure 18, Figures 19 and 20, and Figure 21, respectively. As shown in Figure 17(b), mismodelling remains for high values of the n_{tracks} variable. This is not an issue because the MLP efficiency for these events is very low, so the impact on the background estimate is negligible.

4.2.2 ABCD-Based Background Estimation

A semi-data-driven estimate is used to estimate the background contribution to the SR. The first step towards this estimate is to calculate a fully data-driven ABCD estimate of the background contribution in the signal region. To do this, 4 regions are defined in the space of the three body mass and MLP classifier output variables. Region A is the SR, Region B shares the same three body mass requirement as the signal region but also requires that $0.0108 < MLP < 0.0524$, Region C shares the MLP requirement of the SR but has $155 < m^{\ell\ell j} < 175$ GeV, and Region D is defined by $0.0108 < MLP < 0.0524$ and $155 < m^{\ell\ell j} < 175$ GeV. The region $0.0108 < MLP < 0.0524$ is chosen to contain approximately 10% of the background. An estimate of the background in the SR is then given by $A = BC/D$. This estimate is accurate if the MLP and three body mass variables are uncorrelated, and there is negligible signal contamination in regions B, C and D.

(a) n_{tracks} Pre-Reweighting

(b) n_{tracks} Post-Reweighting

(c) $U_1(0.7)$ Pre-Reweighting

(d) $U_1(0.7)$ Post-Reweighting

(e) $p_{\text{T}}^{\text{jet}}$ Pre-Reweighting

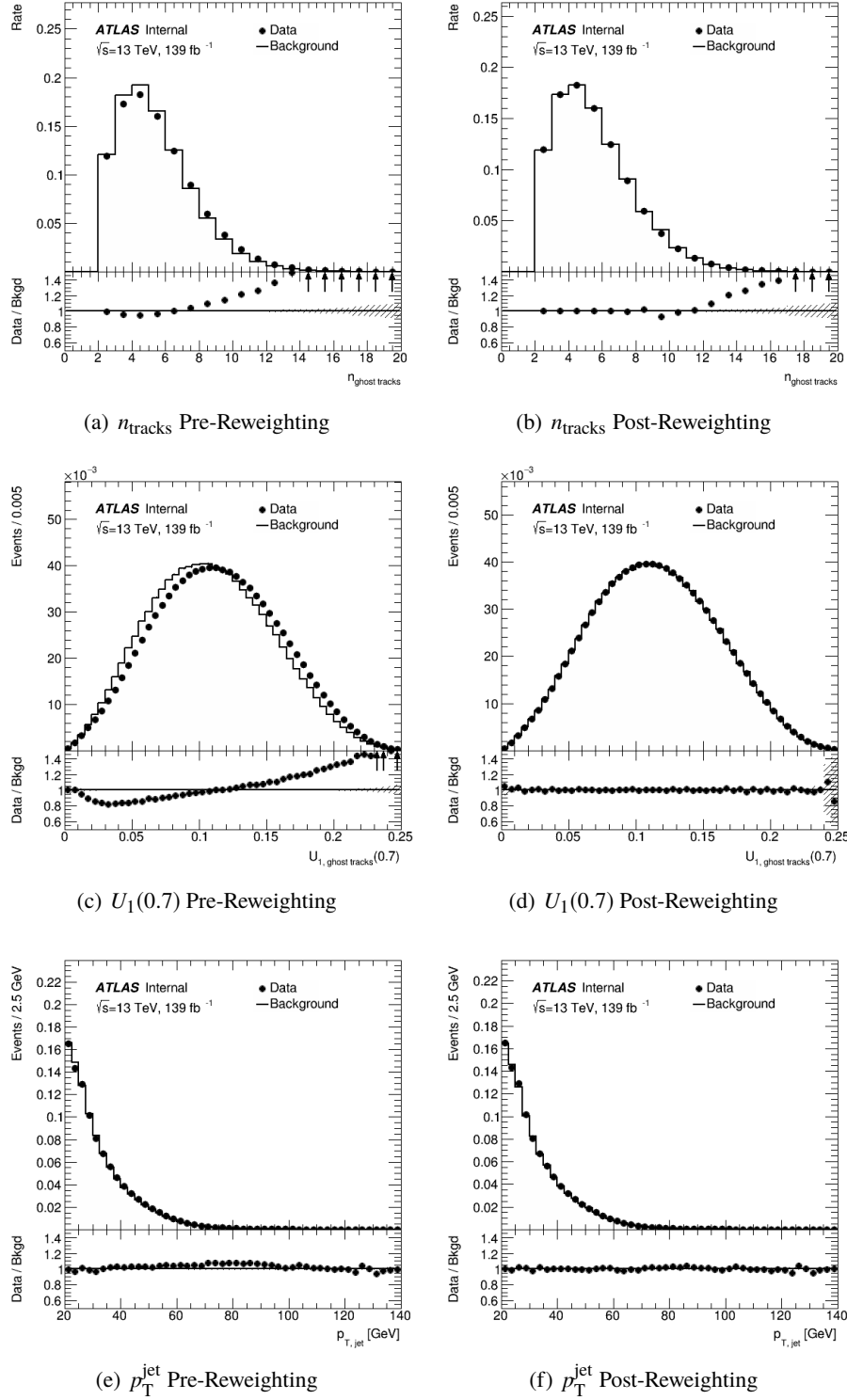(f) $p_{\text{T}}^{\text{jet}}$ Post-Reweighting

Figure 17: Distributions of the three variables used to reweight the background simulation, after the full event-level pre-selection, in data and background MC (both reweighted and not). These variables are the ghost-associated track multiplicity (a), the modified correlation variable $U_1(0.7)$ (b), and the transverse momentum of the calorimeter jet (c).

(a) $m_{\ell^+\ell^-\mathrm{j}}$ Pre-Reweighting

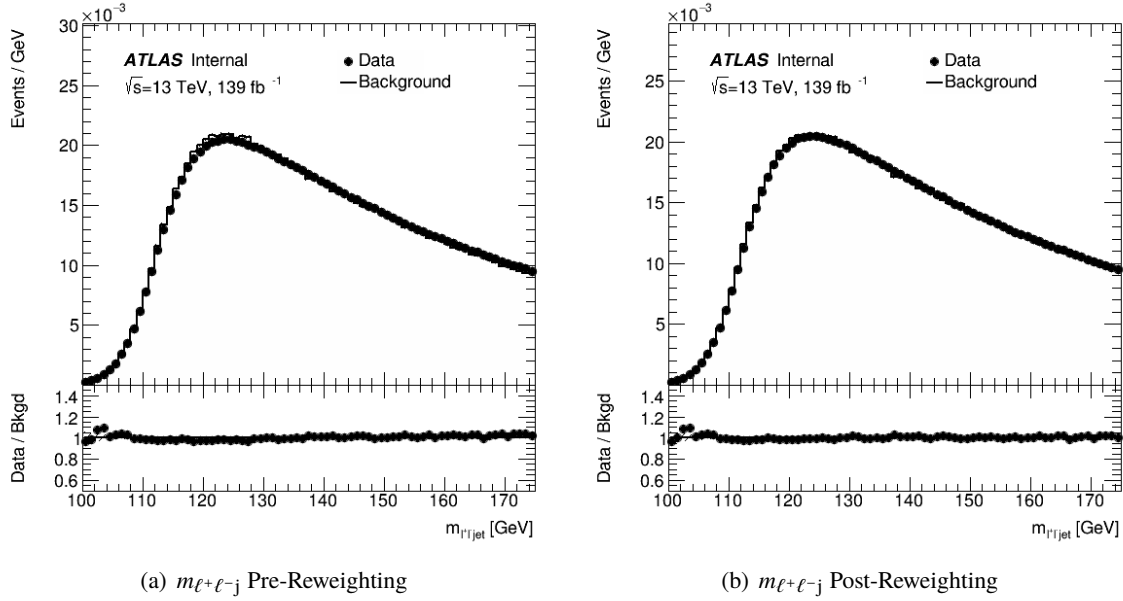(b) $m_{\ell^+\ell^-\mathrm{j}}$ Post-Reweighting

Figure 18: Distributions of the three body mass distribution, after the full event-level pre-selection, in data and background MC (both reweighted and not).

While the MLP input variables were selected to minimise the correlation with the three body mass, a non-negligible correlation remains. A correction factor is derived to account for this correlation, using the half of the MC events which were not used in the training of the MLP. This correction factor is defined as the ratio of the MC background events in the signal region, to the MC-based ABCD estimate in the SR: $A/(BC/D)$. This correction factor multiplies the data-driven ABCD estimate to produce the final background estimate:

$$
A_{\mathrm{SR}}^{\mathrm{ABCD\ Est.}} = \underbrace{\frac{B_{\mathrm{data}}C_{\mathrm{data}}}{D_{\mathrm{data}}}}_{\text{Data-driven ABCD Estimate}} \times \underbrace{\frac{A_{\mathrm{MC}}}{\frac{B_{\mathrm{MC}}C_{\mathrm{MC}}}{D_{\mathrm{MC}}}}}_{\text{MC-based ABCD Correction Factor}} .
$$

This results in an expectation of 82400 ± 2900 background events in the SR, where the uncertainty is derived from the statistical uncertainties in the MC and data inputs to the estimate.

This method allows an estimate of the background in the SR, in which only a double ratio of numbers of events are taken from MC. Only taking ratios of events from MC causes background normalisation uncertainties to fully cancel. While the double ratio ensures that any residual mismodelling in the shape of either of the ABCD variables will cancel insofar as the variables can be considered uncorrelated. The Pearson (Spearman) correlation coefficient between the three body mass and the MLP output variable plane, for post-reweighting background MC, is 6.54% (12.7%).

(a) $p_T^{\text{lead track}}/p_T^{\text{tracks}}$ Pre-Reweighting

(b) $p_T^{\text{lead track}}/p_T^{\text{tracks}}$ Post-Reweighting

(c) $\Delta R^{\text{lead track, calo jet}}$ Pre-Reweighting

(d) $\Delta R^{\text{lead track, calo jet}}$ Post-Reweighting

(e) τ_2 Pre-Reweighting

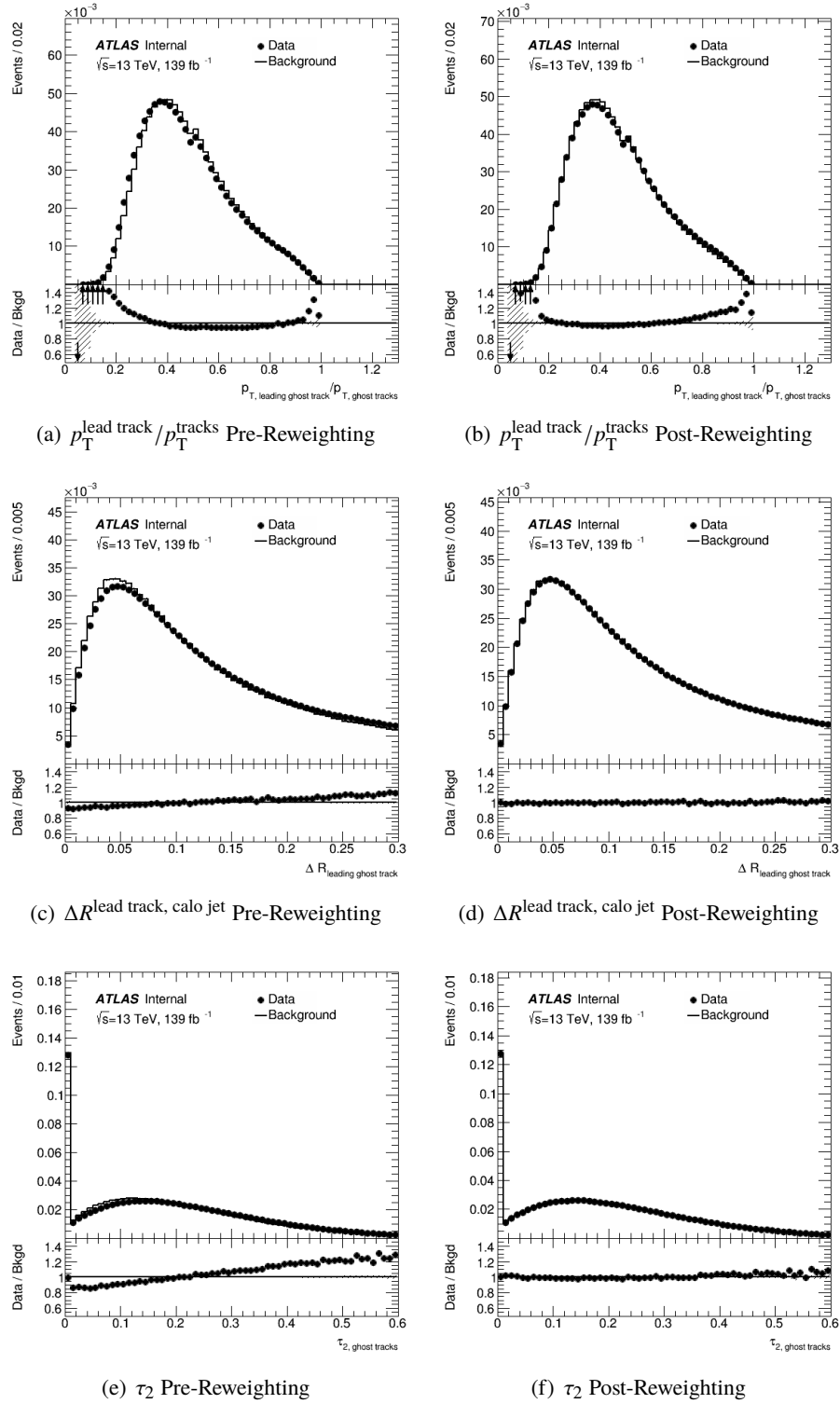(f) τ_2 Post-Reweighting

Figure 19: Distributions of the variables input to the MLP, after the full event-level pre-selection, in data and background MC (both reweighted and not). The modified correlation variable $U_1(0.7)$ is also input to the MLP, but it is used in the reweighting, and shown in Figure 17. In the case of exactly two tracks, the $p_T^{\text{lead track}}/p_T^{\text{tracks}}$ variable can not take values less than 0.5, leading to the spike around 0.5.

(a) $M_2(0.3)$ Pre-Reweighting

(b) $M_2(0.3)$ Post-Reweighting

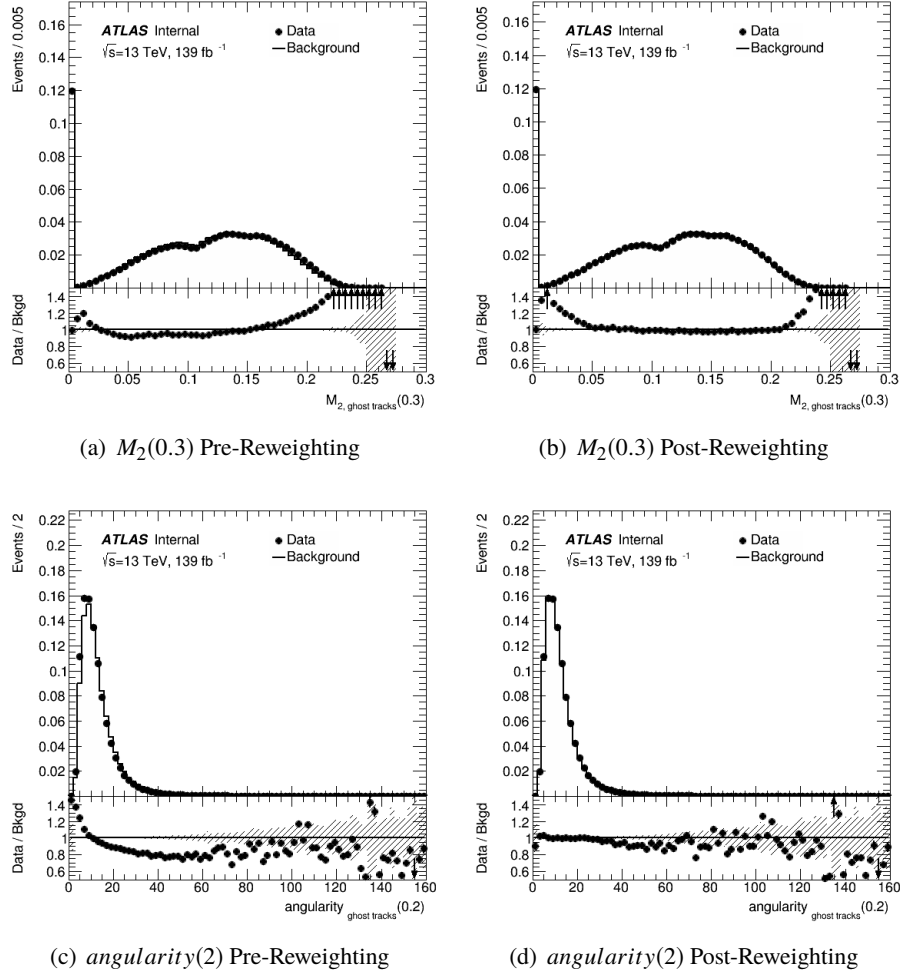(c) $angularity(2)$ Pre-Reweighting

(d) $angularity(2)$ Post-Reweighting

Figure 20: Distributions of the variables input to the MLP, after the full event-level pre-selection, in data and background MC (both reweighted and not). The modified correlation variable $U_1(0.7)$ is also input to the MLP, but it is used in the reweighting, and shown in Figure 17.

(a) Mass Regression MLP Output Variable Pre-Reweighting (b) Mass Regression MLP Output Variable Post-Reweighting

(c) Classification MLP Output Variable Pre-Reweighting (d) Classification MLP Output Variable Post-Reweighting
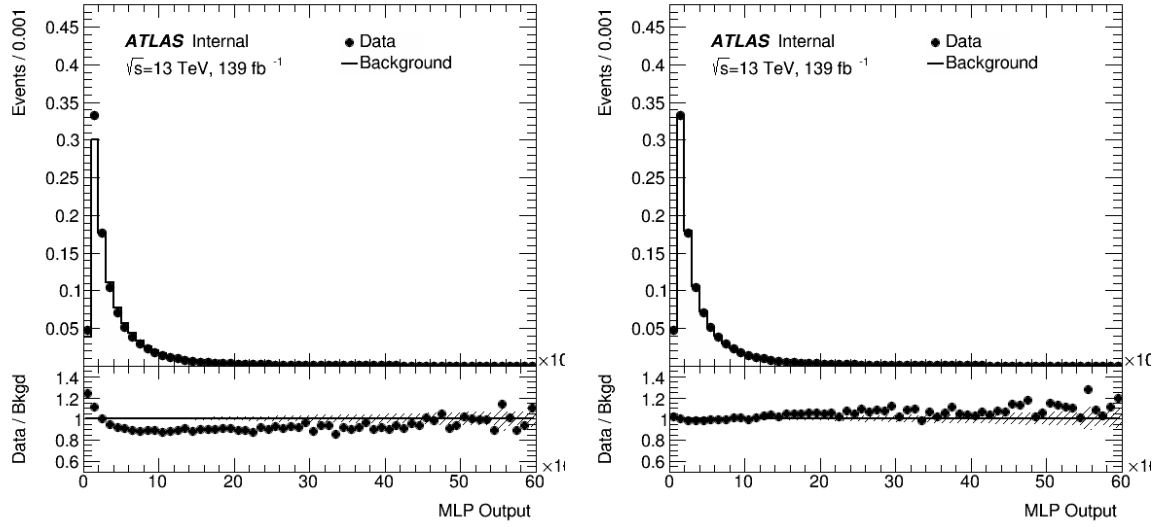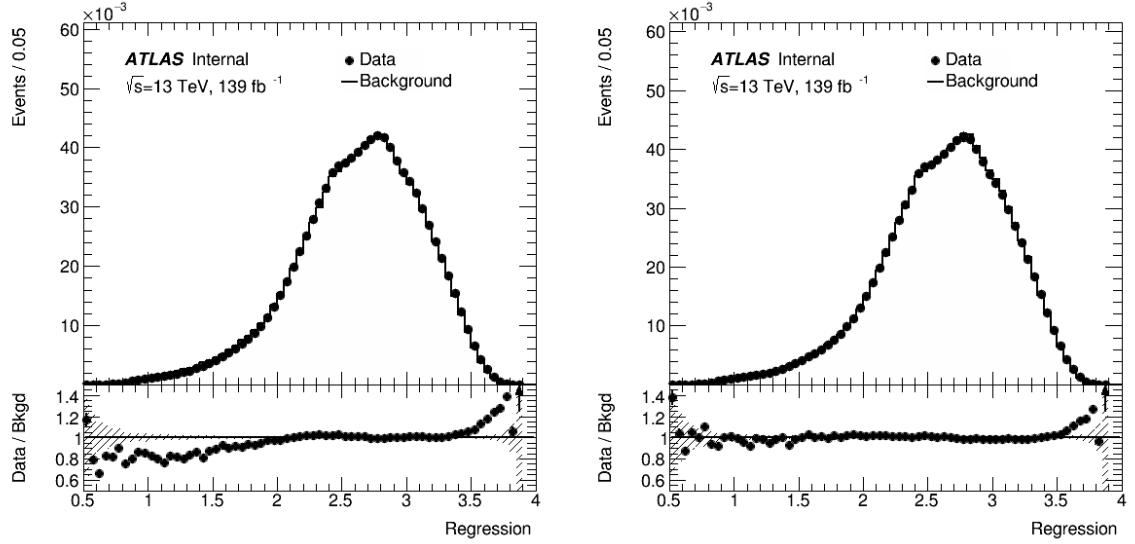
Figure 21: Distributions of the output of the regression (a) and classification (b) MLPs, after the full event-level pre-selection, in data and background MC (both reweighted and not).

4.2.3 Validation of Background Modelling

The background model is compared to data in 13 low-signal validation regions. 15 regions are defined by values of $m_{\ell\ell j}$ of 100-110 GeV, 110-120 GeV, 120-135 GeV, 135-150 GeV, 150-155 GeV, and the *MLP* ranges of > 0.052, $0.037 - 0.052$ and $0.026 - 0.037$. The two MLP validation regions are defined by the ranges in the *MLP* output variable nearest the signal region, which contain equal amounts of background to the signal region. 2 of these 15 regions are blinded due to high signal concentration. The data in each of these regions is shown in Table 9, and the background estimates (calculated following the procedure described in subsection 4.2.2) for each of these regions is shown in Table 10. This information is also provided graphically in Figure 22. Good agreement is seen between the data and the backgrounds estimates in these regions. The MC-based correction factors are presented in Table 11.

MLP Range	$m_{\ell\ell j}$ Range					
	100 − 110 GeV	110 − 120 GeV	120 − 135 GeV	135 − 150 GeV	150 − 155 GeV	155 − 175 GeV
SR (99-100%)	2470	23002	82908	94674	29289	100408
VR (98-99%)	3912	32475	89919	82468	23410	76103
VR (97-98%)	4350	33958	88536	79054	22131	73705

Table 9: Data in background estimate validation regions.

MLP Range	$m_{\ell\ell j}$ Range				
	100 − 110 GeV	110 − 120 GeV	120 − 135 GeV	135 − 150 GeV	150 − 155 GeV
(99-100%)	$2180 \pm 12.5 \pm 356$	$20\,800 \pm 78.4 \pm 1140$	$82\,400 \pm 291 \pm 2850$	$91\,100 \pm 323 \pm 3000$	$31\,100 \pm 123 \pm 1440$
(98-99%)	$3790 \pm 22.7 \pm 346$	$32\,000 \pm 133 \pm 1360$	$88\,700 \pm 351 \pm 2800$	$77\,900 \pm 309 \pm 2540$	$23\,800 \pm 104 \pm 1200$
(97-98%)	$4430 \pm 26.7 \pm 382$	$34\,000 \pm 143 \pm 1440$	$86\,900 \pm 348 \pm 2920$	$76\,100 \pm 306 \pm 2460$	$21\,100 \pm 93.0 \pm 1040$

Table 10: Background estimates (calculated following the procedure described in subsection 4.2.2) in background estimate validation regions. As the number of events in the 155 − 175 GeV bins are used to calculate the background estimates, the background estimate method can not provide a prediction in these regions. The first and second quoted uncertainties are due to limited data and MC statistics, respectively.

MLP Range	$m_{\ell\ell j}$ Range				
	100 − 110 GeV	110 − 120 GeV	120 − 135 GeV	135 − 150 GeV	150 − 155 GeV
(99-100%)	0.350 ± 0.0573	0.443 ± 0.0242	0.704 ± 0.0244	0.867 ± 0.0286	1.03 ± 0.0476
(98-99%)	0.795 ± 0.0727	0.897 ± 0.0382	1.01 ± 0.0319	0.987 ± 0.0322	1.05 ± 0.0528
(97-98%)	0.967 ± 0.0833	0.990 ± 0.0421	1.03 ± 0.0347	1.01 ± 0.0326	0.964 ± 0.0474

Table 11: MC-based correction factors used in the calculation of the background estimates (calculated following the procedure described in subsection 4.2.2) in background estimate validation regions. As the number of events in the 155 − 175 GeV bins are used to calculate the background estimates, the background estimate method can not provide a prediction in these regions. The quoted uncertainties are due to limited MC statistics.

As a further test of the background modelling strategy, these estimates are evaluated using a alternative Z + jets MC generator: MADGRAPH (Appendix C). The results of this test are given in Table 12, and Figure 23. This sample has been reweighted using a procedure designed to mitigate the observed mismodelling in the MADGRAPH Z + jets sample, using the p_T of the calorimeter jet, the p_T of the three
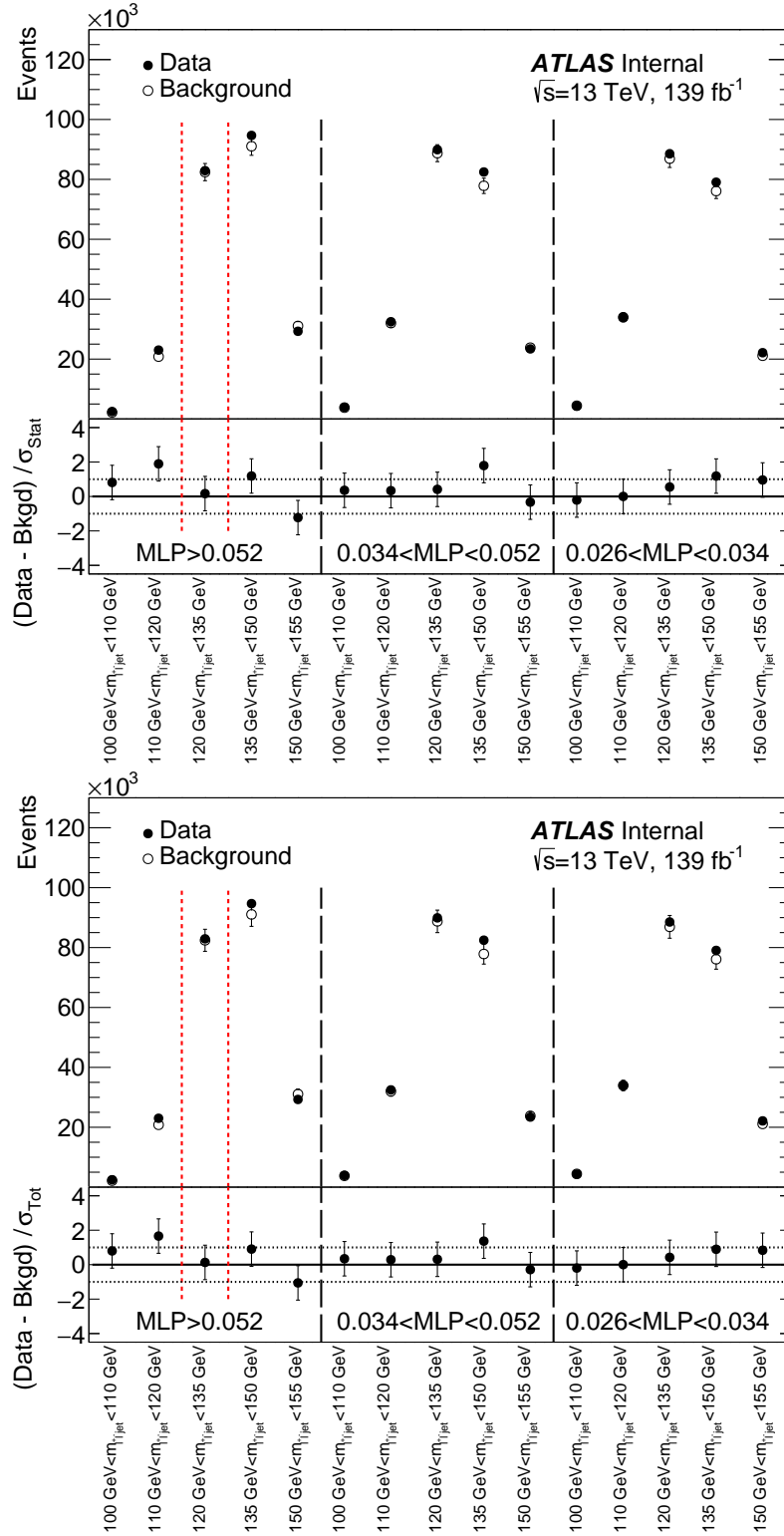
Figure 22: Data and background estimates (calculated following the procedure described in subsection 4.2.2) in background estimate validation and signal regions. As the number of events in the $155 - 175$ GeV bins are used to calculate the background estimates, the background estimate method can not provide a prediction in these regions. The uncertainties in (a) represent just the data and MC statistical uncertainties, while the uncertainties in (b) represent the total statistical and systematic uncertainties in this analysis.

733 body system, and the multiplicity of tracks Ghost-Associated to the calorimeter jet. Various distributions
734 before and after this reweighting is applied are given in Appendix I.

735 Finally, a 1.5 GeV a produced with a BR($H \rightarrow Za$) = 20% results in the background estimate increasing
736 by 0.53%, demonstrating that this background estimation method is robust against significant signal
737 contamination.

MLP Range	$m_{\ell\ell j}$ Range				
	100 − 110 GeV	110 − 120 GeV	120 − 135 GeV	135 − 155 GeV	155 − 175 GeV
(99-100%)	2770 ± 15.9 ± 281	24 500 ± 92.3 ± 865	85 200 ± 301 ± 1970	96 100 ± 341 ± 2140	31 000 ± 123 ± 995
(98-99%)	3340 ± 20.0 ± 300	30 300 ± 126 ± 1040	88 100 ± 348 ± 2160	79 200 ± 314 ± 2000	21 600 ± 94.0 ± 816
(97-98%)	4560 ± 27.5 ± 388	35 200 ± 148 ± 1180	85 900 ± 344 ± 2160	79 100 ± 319 ± 2040	20 900 ± 92.1 ± 793

Table 12: Background estimates (calculated following the procedure described in subsection 4.2.2) in background
estimate validation regions, using the alternative MADGRAPH generator for the Z + jets background. As the number
of events in the 155 − 175 GeV bins are used to calculate the background estimates, the background estimate method
can not provide a prediction in these regions. The first and second quoted uncertainties are due to limited data and
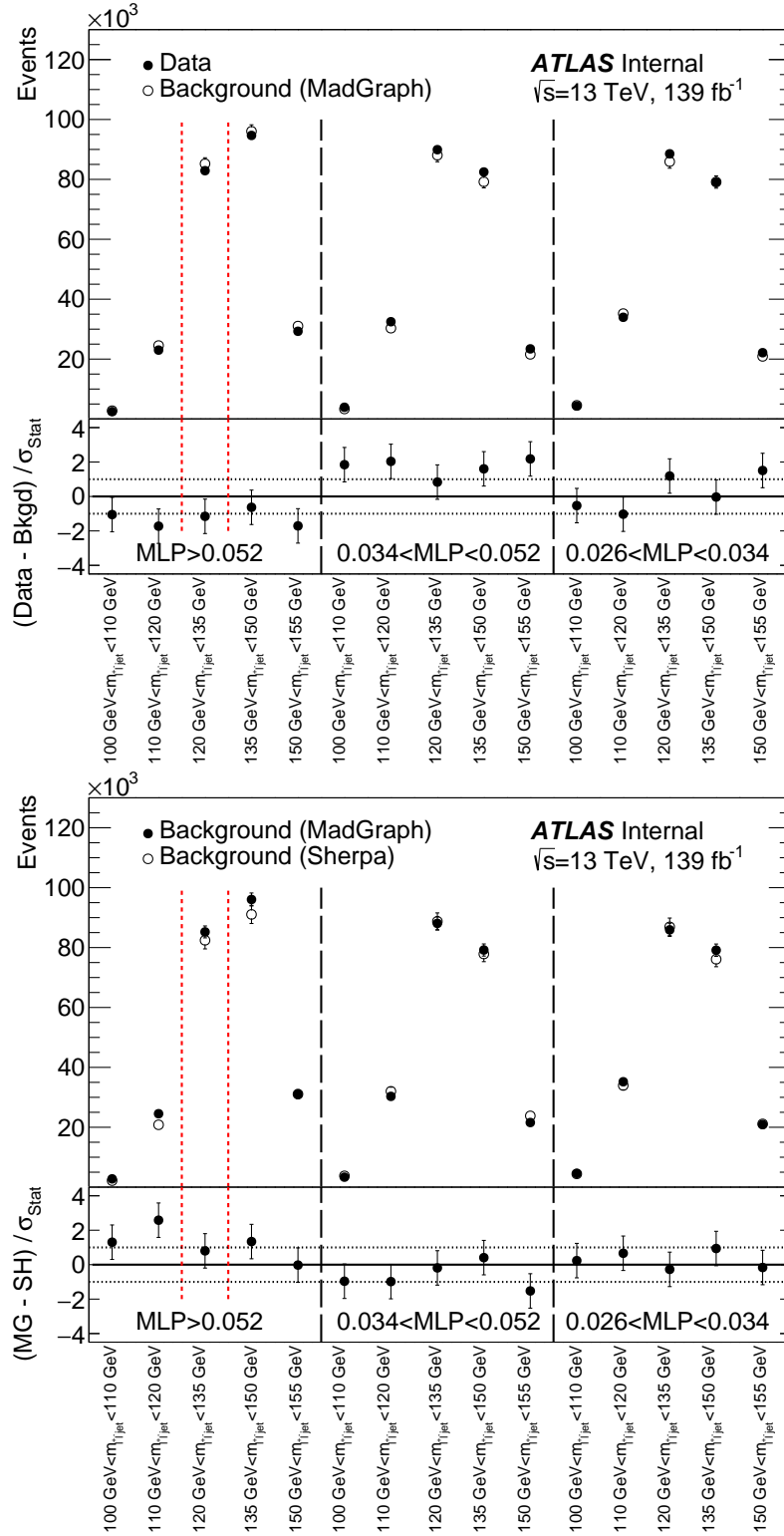MC statistics, respectively.

Figure 23: (a) Data and the alternative MADGRAPH background estimates and (b) alternative MADGRAPH and nominal background estimates (calculated following the procedure described in subsection 4.2.2) in background estimate validation and signal regions. As the number of events in the $155 - 175$ GeV bins are used to calculate the background estimates, the background estimate method can not provide a prediction in these regions. The uncertainties represent the data and MC statistical uncertainties.

5 Systematic Uncertainties

Systematic uncertainties are the dominant sources of uncertainty for this analysis. The systematic uncertainties relevant to this analysis have been implemented in the statistical model as nuisance parameters (NP). The systematic uncertainties are of two types: theoretical uncertainties, and experimental (detector and reconstruction) uncertainties. The following subsections describe the systematic uncertainties relevant to this analysis.

5.1 Systematic Uncertainties: Modelling

The following subsections describe the eight modelling systematic uncertainties relevant to this analysis in order of magnitude, where already evaluated.

5.1.1 Statistical Uncertainty

The dominant uncertainty for this analysis is the statistical uncertainty on the background estimate. This is due primarily to MC statistical uncertainty in the ABCD correction described in subsection 4.2.2. However, there is also a smaller contribution from the statistical uncertainty in data on the pre-correction ABCD estimate described in subsection 4.2.2. This results in a total uncertainty of 3.48% on the background estimate.

The MC statistical uncertainty on the signal estimate varies between 1.69% and 8.00% of the total signal normalisation, for the 0-4 GeV a signal samples, 4.06% for the η_c sample, and 3.98% for the J/ψ sample. This uncertainty is labelled *MCSTAT* in the correlation and pull plots.

5.1.2 Scale and PDF Uncertainties

The renormalisation and factorisation scale, and PDF, uncertainties are investigated for both the signal and Z + jets background samples. The half renormalisation scale uncertainty ($\mu_R = 0.5$) is found to be the largest of these by far, and so is implemented in the fit for both the signal and Z + jets background processes. This is illustrated in Table 13. It is implemented using internal weights in the relevant MC samples. This uncertainty is labelled *MUR* in the correlation and pull plots.

For the Z + jets background sample, the systematic uncertainty is first estimated by the change in the background estimate after a dedicated reweighting is applied to the Z + jets background sample. This dedicated reweighting is calculated analogously to the nominal reweighting, but the Z + jets MC sample used in the calculation of the reweighting factors has the dominant renormalisation scale variation applied. The renormalisation scale uncertainty on the background normalisation was found to be 4.78%; this was reduced from 5.71% due to the dedicated reweighting, showing that the reweighting is successfully reducing the reliance of the background estimate on the chosen MC samples.

This value is found to be consistent with zero within the statistical uncertainty on its evaluation, and the agreement between the background estimates and data in the 14 VRs was greater than would be expected if this uncertainty was accurately estimated by this number, making it likely that it has a large statistical component. As such, this estimate is amended to evaluate the systematic in a region of the MLP variable expected to contain approximately two times more signal than the SR, reducing the statistical component

Variation	Uncertainty
$\mu_R = 0.5$	5.71%
$\mu_R = 2$	0.731%
$\mu_F = 0.5$	0.565%
$\mu_F = 2$	3.68%
$\mu_R = 0.5 \ \& \ \mu_F = 0.5$	2.51%
$\mu_R = 2 \ \& \ \mu_F = 2$	1.14%
MMHT2014nnlo68cl	1.19%
CT14nnlo	1.06%

Table 13: Scale and PDF uncertainties on the total background, evaluated by scaling the Z + jets background and evaluating the change in the background estimate without a dedicated reweighting.

of the estimate. The resulting value of the uncertainty was found to be 1.83%. A linear fit to expanded MLP regions was also considered, as shown in Figure 24(b), but this resulted in an uncertainty of 0.685%, and so the more conservative approach was adopted.
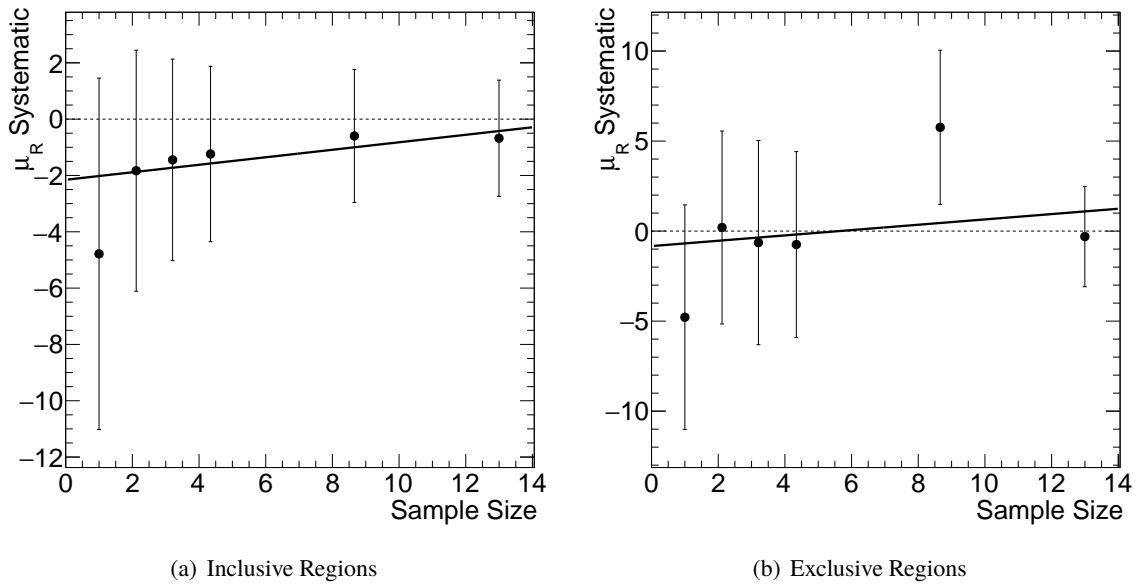

(a) Inclusive Regions

(b) Exclusive Regions

Figure 24: Renormalisation scale uncertainty on the Z + jets background, as determined using various expanded MLP requirements. The regions are defined to (a) contain and (b) not contain all of the more signal-like MLP regions. A linear fit is performed to both regions, and the fit to (b) is used to extract an estimate of this uncertainty.

For the signal samples, the systematic is taken from the change in the signal efficiency under the scaling. The internal weights used in the derivation of these uncertainties are not present in the first generation of MC signal samples: 0.5 GeV, 2.5 GeV and 8 GeV a, and the η_c samples. As such, the renormalisation scale systematic uncertainty on the missing a signal samples are interpolated if possible, else they are taken from the nearest signal sample. The renormalisation scale systematic uncertainty on the η_c signal sample is taken from the J/ψ signal sample. The renormalisation scale systematic uncertainty on the signal estimates are given in Table 14.

a mass / GeV	0.5	0.75	1	1.5	2	2.5	3	3.5	4	η_c	J/ψ
Uncertainty (%)	0.0267	0.0267	0.140	0.345	0.0782	0.103	0.128	0.960	1.66	0.782	0.782

Table 14: Renormalisation scale uncertainties for the various signal samples. They are evaluated for the $\mu_R = 0.5$ variation.

5.1.3 Background Modelling Uncertainty

The hadronisation and ME uncertainties are evaluated for the dominant Z + jets background, by comparing the background estimate derived with the nominal SHERPA MC sample to the background as estimated using an alternative MADGRAPH MC sample. The only difference in the estimation method is the reweighting, which uses different variables due to the different nature of the mismodelling in MADGRAPH. These three variables are the p_T of the calorimeter jet, the p_T of the three body system, and the multiplicity of tracks Ghost-Associated to the calorimeter jet. This results in an uncertainty of 3.40% on the background normalisation. The key distributions in the derivation of this estimate are compared for MADGRAPH and SHERPA in Figure 25. This uncertainty is labelled *MUR* in the correlation and pull plots.

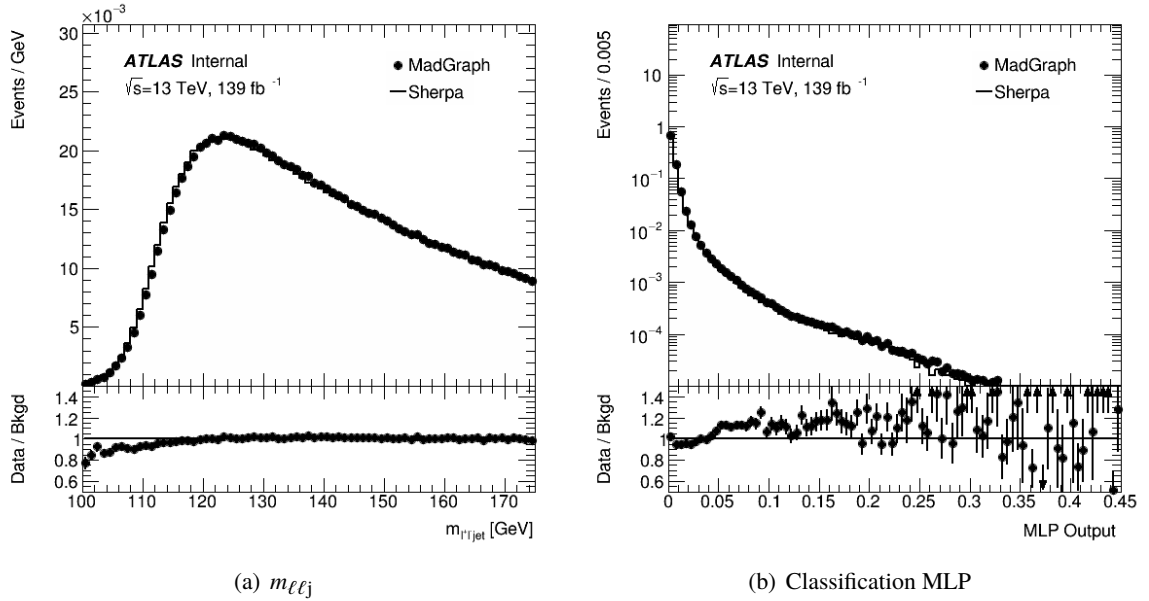(a) $m_{\ell\ell\text{j}}$

(b) Classification MLP

Figure 25: Distributions of the output of the three body mass (a) and classification MLP (b), for background MC, where the Z + jets process is being modelled by MADGRAPH and SHERPA. A dedicated reweighting is applied for both backgrounds, which differs between backgrounds.

This value is found to be consistent with zero within the statistical uncertainty on its evaluation, and the agreement between the background estimates and data in the 14 VRs was greater than would be expected if this uncertainty was accurately estimated by this number, making it likely that it has a large statistical component. As such, this estimate is amended to evaluate the systematic using a linear fit to expanded MLP regions, as shown in Figure 26(b), to reduce the statistical component of the estimate. The resulting value of this uncertainty was found to be 2.11%. Expanding the MLP region by a factor of two was also considered, but this resulted in an uncertainty of 1.19%, and so the more conservative approach was adopted.
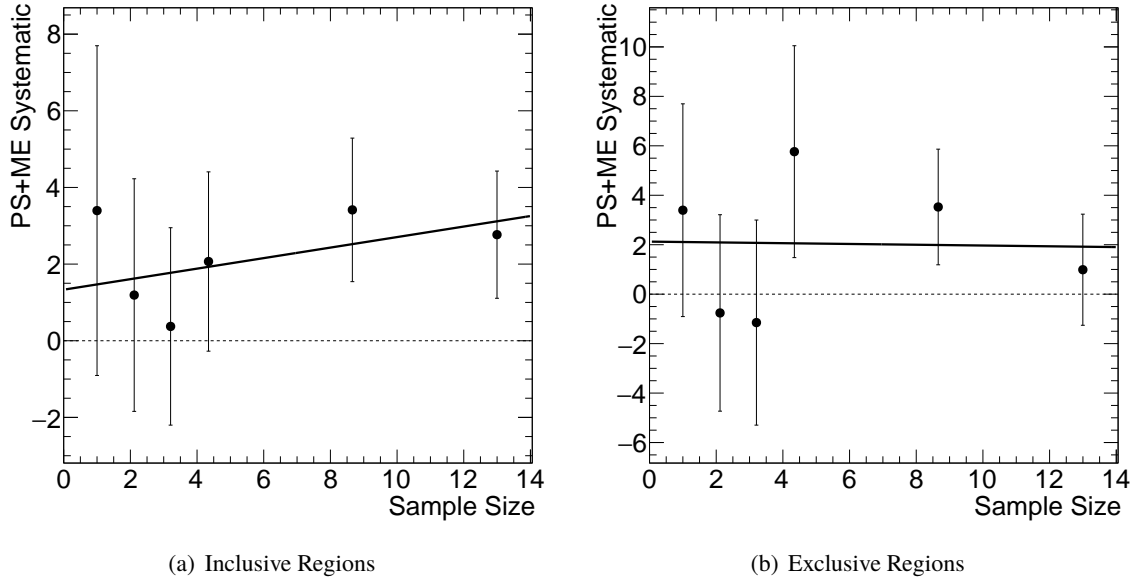
(a) Inclusive Regions

(b) Exclusive Regions

Figure 26: Background modelling uncertainty representing the hadronisation and ME uncertainties on the Z + jets background was estimated, as determined using various expanded MLP requirements. The regions are defined to (a) contain and (b) not contain all of the more signal-like MLP regions. A linear fit is performed to both regions, and the fit to (b) is used to extract an estimate of this uncertainty.

5.1.4 Signal Hadronisation Uncertainty

The effect of the signal hadronisation modelling uncertainty on the MLP output has been evaluated by calculating the change in acceptance after reweighting events based on generator-level track multiplicity and $U1(0.7)$. These reweightings are derived from an alternative signal sample produced using HERWIG7. This is based on the assumption that the largest impact of the modelling uncertainty is on the MLP via the track multiplicity. Due to technical limitations in HERWIG7, only quark decays are used in the calculation of the scale factors, and the 1.5 GeV a scale factors are used as a proxy for all lower masses. The hadronisation uncertainties on the signal estimates are given in Table 15. This uncertainty is labelled *PS* in the correlation and pull plots.

a mass / GeV	0.5	0.75	1	1.5	2	2.5	3	3.5	4	η_c	J/ψ
Uncertainty (%)	16.5	17.7	15.4	13.5	8.97	7.10	6.78	10.9	4.16	3.61	18.3

Table 15: Hadronisation uncertainties for the various signal samples.

5.1.5 Higgs Cross Section Uncertainty

Theory (truncation, unknown N^{3}LO PDFs and unknown finite-mass effects), renormalisation and factorisation scale, combined PDF, α_s, and flavour scheme uncertainties (only for tH associated production) are applied to the various Higgs production mode cross sections. These are taken from the official recommendations of the CERN Higgs Cross Section Working Group [72, 73]. The different types of

814 uncertainty are summed in quadrature, then a the uncertainties on the various Higgs production processes
815 are summed (weighted by the relevant cross sections) to calculate the total uncertainty. For all uncertainties,
816 a Higgs boson mass of 125 GeV is assumed. The uncertainty on the ggF process is by far the largest
817 contribution to the total uncertainty, with a combined theory, renormalisation and factorisation scale
818 uncertainty of $^{+4.6}_{-6.7}\%$, a PDF uncertainty of 1.9%, and a $+\alpha_s$ uncertainty of 2.6%. The uncertainty on the
819 inclusive cross section is $^{+9.4}_{-9.3}\%$. This uncertainty is labelled *HXS* in the correlation and pull plots.

5.1.6 Signal Production Uncertainty

821 The full inclusive Higgs production cross section is used to normalise the signal yields, while only the
822 ggF production mode is used to model the signal samples. We account for this by applying a systematic
823 uncertainty on the signal acceptance, derived from a comparison of generator-level MC. 100k ggF and
824 100k VBF events are generated using Pythia, the acceptance of these are compared in a generator-level
825 fiducial acceptance. The Higgs boson is more highly boosted in the case of VBF production, which means
826 the individual objects are more likely to pass the minimum p_T requirements. However, the boost means that
827 the angular separation between the objects is smaller, so they are more likely to fail the overlap removal for
828 VBF production. This leads to the generator-level acceptances differing by just 0.941%. This uncertainty
829 is scaled down to 12.8% of this value, which is the fraction of Higgs boson events in the SM which are not
830 produced by ggF, leading to an overall systematic uncertainty of just 0.120%. This uncertainty is labelled
831 *GGFACC* in the correlation and pull plots.

5.1.7 Signal Data to MC Discrepancy Uncertainty

833 The uncertainty described in subsection 5.1.4 estimates the effect of any mismodelling of the hadronisation
834 of the signal resonance. However, it is possible that other sources of mismodelling in the signal samples
835 may affect the estimates of the signal efficiencies. One such mechanism through which this may occur, is
836 the known mismodelling in the length of the beamspot in MC, which is 30% longer than data. The effect
837 of this mismodelling is estimated by reweighting the event in MC based on the z_0 of the primary vertex to
838 match data. For the 1.5 GeV a signal sample, this results in the efficiency decreasing by $\sim 2.0\%$, which has
839 a negligible impact on the final result.

840 Other similar affects may be present but unnoticed. A method to place an upper bound on the impact of
841 any such affect is to apply the background reweighting scale factors, described in subsection 4.2.1, to the
842 signal. This will exaggerate the impact of this uncertainty, because it also factors in any mismodelling in
843 the Sherpa2.2.1 Z + jets distribution. This results in an uncertainty on the signal efficiency of $\sim 5.0\%$ for
844 the 1.5 GeV a signal sample. Including this uncertainty in the likelihood fit as a nuisance parameter, as
845 described in subsection 6.1, leads to the observed limit for the 1.5 GeV a signal hypothesis changing by
846 $\sim 0.2\%$. Due to the negligible impact of this uncertainty, even after it double-counts the mismodelling in
847 the Sherpa2.2.1 Z + jets distribution, this uncertainty is not included in the final statistical model.

5.1.8 Reweighting Procedure Uncertainty

849 If any uncertainty were to be introduced by the reweighting procedure, this should be covered by the
850 uncertainty described in subsubsection 5.1.3, which uses a different reweighting procedure. However, any
851 such uncertainty is conservatively estimated in a more direct way by reevaluating the background estimate

852 without the reweighting, and evaluating the change in the background estimate. This is found to be 1.30%,
853 which is both small and highly conservative, and is therefore not included in the final fit.

5.2 Systematic Uncertainties: Experimental

855 The following subsections describe the seven experimental systematic uncertainties relevant to this analysis
856 in order of magnitude, where already evaluated.

5.2.1 Jet Energy Scale Uncertainties

858 The standard jet energy scale uncertainties are expected to be among the largest experimental uncertainties
859 for this analysis. They have been calculated using the *JetUncertaintiesTool* [74]. These uncertainties have
860 many sub-components, including those derived from: *in-situ* analysis, η calibration, high-p_T jets, pileup,
861 flavour composition, flavour response, b-jets and punch-through jets. The *SIMPLE* configuration is used, in
862 which a principle component analysis is used to combine the different components of the jet uncertainty, in
863 such a way as to preserve correlations in certain jet-kinematic regions, resulting in 30 nuisance parameters.
864 We are currently using *Scenario1*. This results in an uncertainty that varies between $^{+0.449}_{-11.1}$% and $^{+3.99}_{-21.3}$% of
865 the total signal normalisation for the 0-4 GeV a signal hypotheses, an uncertainty of $^{+0.533}_{-20.5}$% for the η_c
866 signal sample normalisation, and an uncertainty of $^{+1.63}_{-13.0}$% for the J/ψ signal sample normalisation.

867 The impact of the jet energy scale on the signal selection efficiencies is asymmetric due to the requirement
868 applied on the three body mass. If the jet energy scale is increased (decreased), the signal peak in the three
869 body mass distribution is shifted up (down), and more events are lost through the upper (lower) side of the
870 window that are gained through the lower (upper). So a shift up or down in the jet energy scale causes a
871 lowering of the signal efficiency. This causes in an asymmetric likelihood, as shown in Figure 27. This
872 asymmetry causes a deterioration in the expected limit in the event of a null observation, but has almost no
873 affect on the discovery potential. This uncertainty is labelled *JES* in the correlation and pull plots.

5.2.2 Pileup Uncertainty

875 The uncertainty on the pileup distribution affects many aspects of the event, especially the MLP input
876 variables, which in turn affects the efficiency of the MLP requirement. This is modelled by reweighting
877 the pileup distributions using the *CP::PileupReweightingTool* tool [75], using the actual-μ distribution
878 for the 2017 data as per the recommendations. This uncertainty covers the discrepancy seen between
879 predicted and measured inelastic cross-section in the fiducial volume defined by $M_X > 13$ GeV, where M_X
880 is the mass of the non-diffractive hadronic system. This discrepancy arises because of mismodelling of
881 the central activity by the MC tune, so can be incorporated into analysis as an uncertainty on the mean
882 number of hard interactions per bunch crossing that a given MC event corresponds to. This results in a
883 total uncertainty that varies between $^{-1.38}_{+1.39}$% and $^{-2.03}_{+1.84}$% of the total signal normalisation for the different
884 0-4 GeV a signal hypotheses, an uncertainty of $^{-0.455}_{+0.0357}$% for the η_c signal sample normalisation, and an
885 uncertainty of $^{-1.19}_{+1.53}$% for the J/ψ signal sample normalisation. The anti-correlation between the pileup
886 NP and the signal normalisations is due to the fact that signal jets have less Ghost-Associated tracks, and
887 so events with higher pileup are less likely to pass the MLP cut. This uncertainty is labelled *PRW* in the
888 correlation and pull plots.

5.2.3 Luminosity Uncertainty

The uncertainty in the combined 2015-2018 integrated luminosity is 1.7%. It is derived from the calibration of the luminosity scale using x-y beam-separation scans, following a methodology similar to that detailed in Ref. [76], and using the LUCID-2 detector for the baseline luminosity measurements [77]. This uncertainty is labelled *LUMI* in the correlation and pull plots.

5.2.4 Lepton Uncertainties

Data-driven uncertainties on the reconstruction, identification and isolation of electrons, as well as the reconstruction, isolation and track-to-vertex association of muons are considered in this analysis. These uncertainties are derived using $Z \rightarrow \ell^+\ell^-$ events, in addition to $J/\psi \rightarrow \mu\mu$ events for muons. The uncertainties for electrons (muons) are all computed using the *AsgElectronEfficiencyCorrectionTool* [53] (*CP::MuonEfficiencyScaleFactors* [57]) tool, as recommended and provided by the egamma (muon) CP group. For the electron tool, the *TOTAL* correlation model is used, in conjunction with the *Moriond_February2018_v1* configuration files. As all of these lepton uncertainties small, for convenience they are added in quadrature as though they were uncorrelated, and evaluated as one total lepton uncertainty. This results in a total uncertainty that varies between $^{+0.943}_{-0.941}\%$ and $^{+1.08}_{-1.08}\%$ of the signal normalisation for the various 0-4 GeV a signal hypotheses, an uncertainty of $^{+1.05}_{-1.05}\%$ for the η_c signal sample normalisation, and an uncertainty of $^{+1.03}_{-1.02}\%$ for the J/ψ signal sample normalisation. These uncertainties are labelled *LEP* in the correlation and pull plots.

5.2.5 Jet Vertex Tagging Uncertainties

Requirements are placed on the impact parameters of the jets from the primary vertex. These impact parameters have associated experimental uncertainties, which influence the efficiency of the jet vertex tagging cut. These efficiency scale factors are calculated using the *JetUpdateJvt* tool [78]. These uncertainties are between about 0.2% and 0.6% for $|\eta| < 2.4$, and between about 0.1% and 0.2% for $2.4 < |\eta| < 2.5$, depending on the p_T of the jet. This results in an uncertainty that varies between $^{+0.584}_{-0.578}\%$ and $^{+0.647}_{-0.639}\%$ of the total signal normalisation for the 0-4 GeV a signal hypotheses, an uncertainty of $^{+0.610}_{-0.604}\%$ for the η_c signal sample normalisation, and an uncertainty of $^{+622}_{-0.614}\%$ for the J/ψ signal sample normalisation. This uncertainty is labelled *JVT* in the correlation and pull plots.

5.2.6 Trigger Efficiency Uncertainty

Data-driven uncertainties on the trigger efficiencies are also considered in this analysis. Due to the multiple triggers used for this analysis, these uncertainties are computed using the *TrigGlobalEfficiencyCorrectionTool* [79], taking the *CP::MuonTriggerScaleFactors* [80] and *AsgElectronEfficiencyCorrectionTool* [53] tools as inputs, as per the recommendations of the egamma and muons CP groups. For the electron trigger efficiency tools, the *TOTAL* correlation model is used, in conjunction with the *Consolidation_September2018_v1* configuration files. For the muon trigger efficiencies, both the statistical and systematic components of the uncertainty are calculated. As these are all fairly small uncertainties, for convenience they are added in quadrature as though they were uncorrelated, and evaluated as one total trigger uncertainty. This results in an uncertainty that varies between $^{+0.270}_{-0.115}\%$ and $^{+0.319}_{-0.134}\%$ of the total signal

normalisation for the 0-4 GeV a signal hypotheses, an uncertainty of $^{+0.344}_{-0.144}$% for the η_c signal sample normalisation, and an uncertainty of $^{+0.328}_{-0.122}$% for the J/ψ signal sample normalisation. This uncertainty is labelled *TRIG* in the correlation and pull plots.

5.2.7 Tracking Uncertainties

The effect of the track smearing uncertainties on the MLP input variables has been estimated using the *InDet::IInDetTrackSmearingTool* [81]. This is propagated through to the MLP cut efficiency, and found to have a negligible impact on the signal efficiency, and as such is not included in the fit. The impact of these uncertainties has less than a ~ 0.4% effect on the signal for all systematic variations and all signal hypotheses.

6 Statistical Interpretation

6.1 Statistical Model

The statistical interpretation of the result is performed using a single-bin profile likelihood fit to the signal region, using the RooStats and RooFit frameworks. This uses a binned profile likelihood fit to extract the final results from the observed number of events, and the signal and background estimates described in the previous two sections. This likelihood is given by the product of the Poisson probability term for the signal region, and the Gaussian constraints on the various nuisance parameters which represent the systematic uncertainties described in Section 5:

$$\mathcal{L} = \text{Pois}\left(N_{\text{SR}}^{\text{D}}; \boldsymbol{\mu}\mathcal{L}_{\text{int}}\sigma_{\text{SM}}(H)\mathcal{B}(Z \to \ell^+\ell^-)\text{Eff}_{\text{SR}}^{\text{MC}}\prod_{i\epsilon S}\boldsymbol{\alpha_i} + A_{\text{SR}}^{\text{ABCD Est.}}\prod_{i\epsilon B}\boldsymbol{\alpha_i}\right) \times \prod_{i\epsilon S+B}\text{Gaus}\left(1; \boldsymbol{\alpha_i}, \sigma_i\right),$$

where variables in bold are free in the fit. N_{SR}^{D} is the observed number of data events in the signal region, $\mathcal{L}_{\text{int}}$ is the integrated luminosity, $\sigma_{\text{SM}}(H)$ is the SM Higgs production cross section, $\mathcal{B}(Z \to \ell^+\ell^-)$ is the BR of the Z boson to electron or muon pairs and $\text{Eff}_{\text{SR}}^{\text{MC}}$ is the signal efficiency in the SR, as determined in MC. The parameter of interest μ scales the signal in the fit, and is left free. The α parameters represent the nuisance parameters, which model the effect of the systematic uncertainties, and are described in Sections 5.1 and 5.2. A likelihood ratio test statistic is then defined as

$$q_\mu = -2\ln(\mathcal{L}(\mu, \hat{\hat{\alpha}})/\mathcal{L}(\hat{\mu}, \hat{\alpha})),$$

where $\hat{\mu}$ and $\hat{\alpha}$ are the values of the parameters which maximise the likelihood, and $\hat{\hat{\alpha}}$ are the values which maximise $\mathcal{L}$ given a certain value of μ. This test statistic is used to measure the compatibility between the background-only model and the data. We then define the local p_0 value as the probability, assuming the background-only model, that we would have observed a test statistic at least as incompatible with the background-only model than the observed test statistic. This is then used to form exclusion intervals using the CL_s method [82, 83].

6.2 Asimov Fits

Asimov datasets are defined based on the background hypothesis, and varying levels of signal. These are then fit with the signal plus background model, and the asymptotic approximation is used to produce uncertainties and limits. The uncertainties on the signal normalisation, along with 95% CL_s upper limits on both μ and $\sigma(H) \times \mathcal{B}(H \to Za)$, expected in the absence of a signal are summarised in Table 16.

The profiled likelihood curve, pull plot and correlation plot for the fit to the 1.5 GeV a signal hypothesis, are shown in Figures 27, 28 and 29, respectively. Signal injection tests are performed, in which various amounts of 1.5 GeV a signal are injected into the Asimov dataset, and then fitted to recover the fitted level of signal. The fitted signal consistently recovers the injected signal, as shown in Figure 30.

		95% CL$_s$ Limit	
a mass / GeV	$\Delta\mu$ (%)	μ (%)	$\sigma(H) \times \mathcal{B}(H \to Za)$/pb
0.5	30.6	$32.3^{+12.7}_{-9.0}$	$18.0^{+7.1}_{-5.0}$
0.75	29.8	$36.8^{+14.4}_{-10.3}$	$20.3^{+8.0}_{-5.7}$
1	30.3	$36.6^{+14.4}_{-10.2}$	$20.0^{+7.9}_{-5.6}$
1.5	30.1	$40.7^{+16.0}_{-11.4}$	$22.5^{+8.8}_{-6.3}$
2	32.2	$50.0^{+19.6}_{-14.0}$	$27.5^{+10.8}_{-7.7}$
2.5	39.3	$72.2^{+28.3}_{-20.2}$	$39.9^{+15.6}_{-11.1}$
3	72.0	141^{+55}_{-40}	$78.3^{+30.7}_{-21.9}$
3.5	97.3	195^{+76}_{-54}	108^{+42}_{-30}
4	342	675^{+265}_{-189}	374^{+146}_{-104}
η_c	91.0	184^{+72}_{-51}	102^{+40}_{-28}
J/ψ	89.8	180^{+71}_{-50}	$99.7^{+39.0}_{-27.8}$

Table 16: Uncertainties on the signal strength parameters for $\mu = 1$, and 95% CL$_s$ upper limits on $\sigma(H) \times \mathcal{B}(H \to Za)/\sigma_{\mathrm{SM}}(H)$ expected in the absence of a signal. $\Delta\mu$ is the post-fit uncertainty on the parameter of interest: $\sigma(H) \times \mathcal{B}(H \to Za)/\sigma_{\mathrm{SM}}(H)$. The uncertainties, $\Delta\mu$, are the mean of the upward and downward MINOS uncertainties. While the 68% intervals are given for all quoted limits. Pythia8 a BRs are assumed, using the default BSMHiggs $\tan\beta$ value of 1, as given in Table 3.

(a) Without Systematics
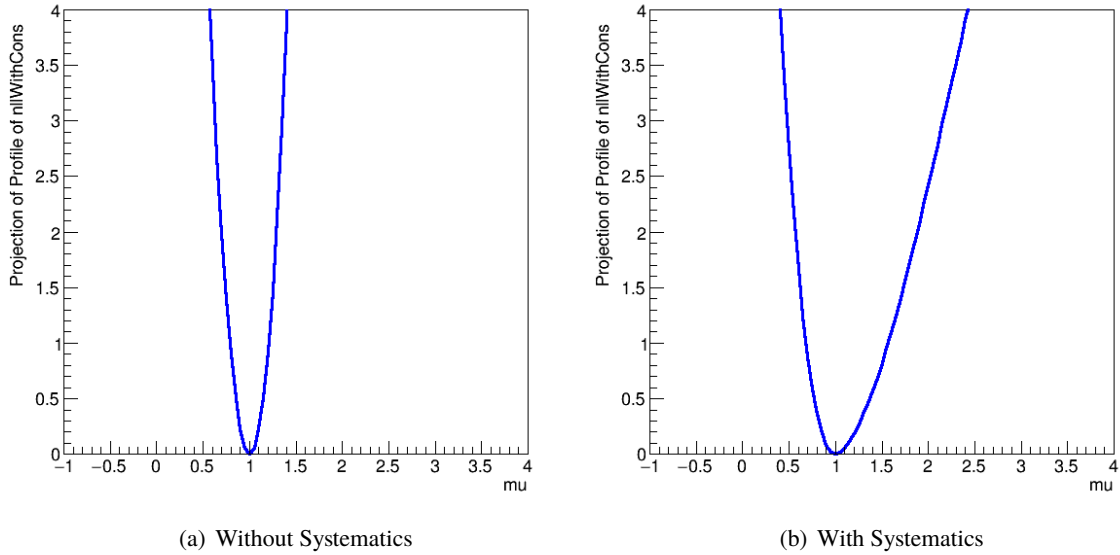
(b) With Systematics

Figure 27: The profiled likelihood curve for the fit to the Asimov dataset using the 1.5 GeV a signal hypothesis, with (a) no systematics except the background MC statistical uncertainty and (b) with all systematics, for a dataset with $\mu = 1$.
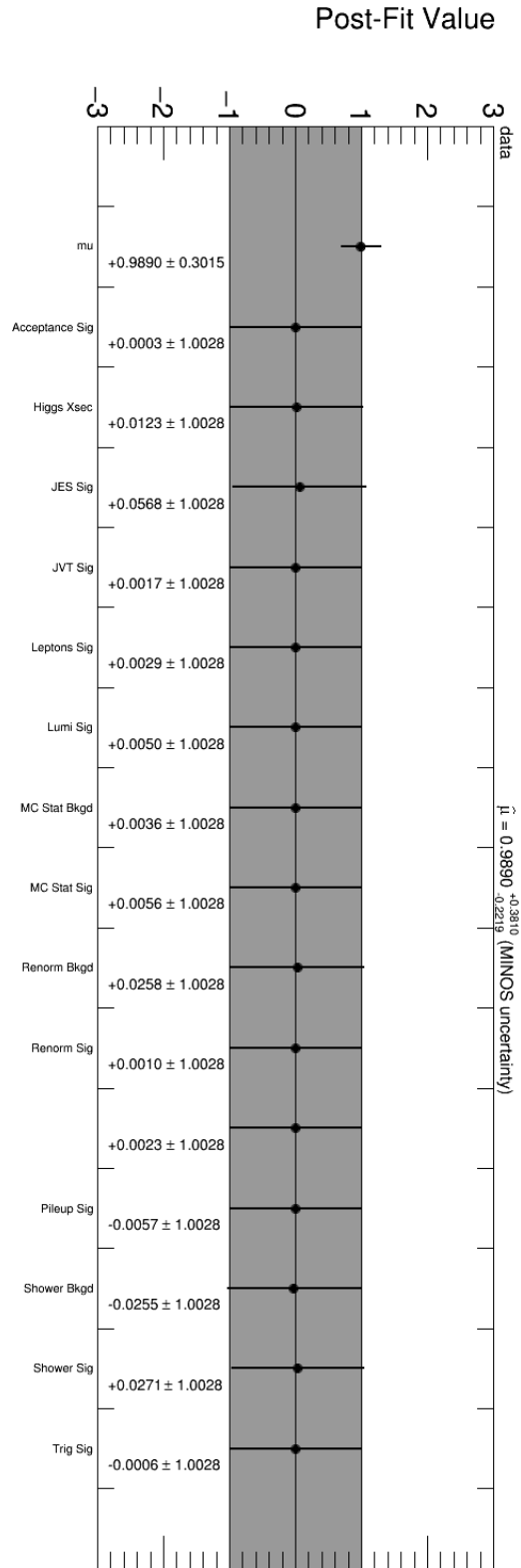
Post-Fit Value

Figure 28: The pull plot for the fit to the Asimov dataset using the 1.5 GeV *a* signal hypothesis, with systematics.
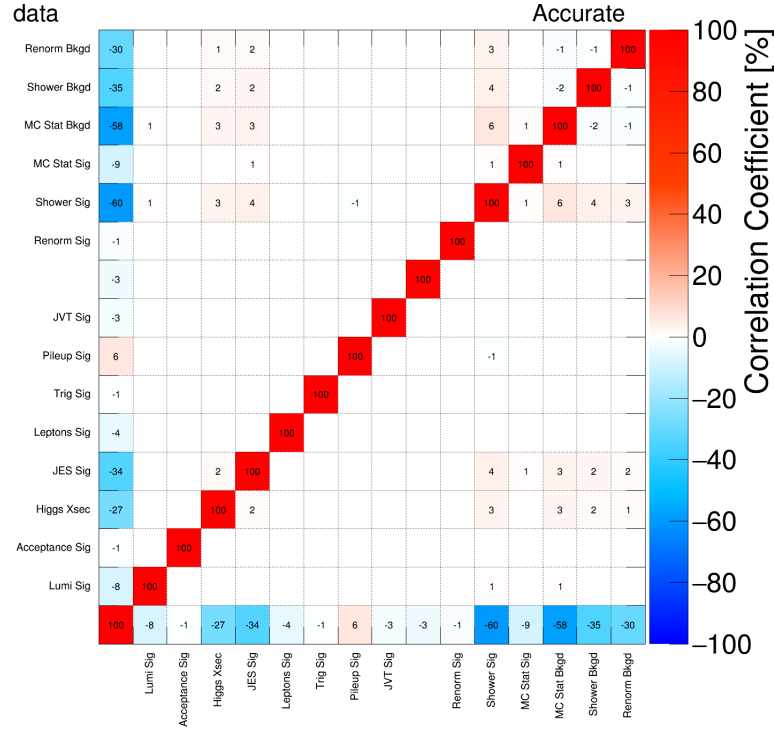
Figure 29: The correlation matrix for the fit to the Asimov dataset using the 1.5 GeV *a* signal hypothesis, with systematics. Only entries with values greater than 0.5% are plotted.

6.3 Uncertainty Breakdown

The breakdown of the uncertainties on μ are given for three example signal hypotheses in Table 17. The total uncertainty is approximately 99.7% systematic, the vast majority of which is due to the background modelling uncertainty. Due to the dominance of the background uncertainties, the pre-fit impact of the uncertainties described in Section 5 on the background estimate, are summarised in Table 18.

6.4 Model-Independent Interpretation

The nominal interpretation strategy assumes either a 2HDM(+s) or SM charmonium signal hypothesis, which although well motivated do not describe all possible processes which can produce this final state. The assumed BRs for these final states in each model leads to model-dependent limits which are only valid for the model under consideration, and not valid for other models.

To generalise the results of this search, model-independent results will be provided under the following assumptions. First, as the focus of this search, only hadronic decays are considered. Second, due to the Yukawa-ordering of the decays of Higgs bosons, only decays to gluons and the heaviest kinematically accessible quark will be considered. Third, due to the low masses of the first generation quarks, decays to these final states will not be considered. Fourth, the systematic uncertainties on each exclusive decay

a mass	0.5 GeV	1.5 GeV	2.5 GeV
Total Uncertainty	8.3 (100%)	10.7 (100%)	20.3 (100%)
Total Statistical Uncertainty	0.6 (7.6%)	0.8 (7.6%)	1.6 (7.7%)
Total Systematic Uncertainty	8.2 (99.7%)	10.7 (99.7%)	20.2 (99.7%)
Signal Systematic Uncertainties			
Jet Energy Scale	1.3 (16.0%)	1.5 (13.5%)	1.5 (7.5%)
Parton Shower	1.4 (16.5%)	1.4 (13.4%)	1.4 (7.1%)
Luminosity, Pileup, Trigger, Leptons, & JVT	0.2 (2.7%)	0.3 (2.6%)	0.5 (2.4%)
MC Statistics	0.2 (2.0%)	0.2 (1.9%)	0.6 (2.7%)
Renormalization Scale	0.1 (1.0%)	< 0.1 (< 1.0%)	0.2 (1.1%)
Acceptance	0.1 (1.0%)	< 0.1 (< 1.0%)	0.2 (0.8%)
Background Systematic Uncertainties			
MC Statistics	6.4 (77.8%)	8.4 (77.8%)	15.8 (77.8%)
Parton Shower and ME	3.9 (47.1%)	5.1 (47.1%)	9.6 (47.1%)
Renormalization Scale	3.4 (40.9%)	4.4 (40.9%)	8.3 (40.9%)

Table 17: Breakdown of the impact of the various sources of uncertainty on the estimate of $\sigma(pp \to H)\mathrm{BR}(H \to Za)/$pb for three different a mass hypotheses, derived from fits to the background-only Asimov dataset. The relative contribution of each source of uncertainty is given in parentheses. JVT and ME refer to the jet vertex tagging and matrix element uncertainties, respectively. The uncertainties are taken as the mean of the upward and downward MINOS uncertainties. The uncertainties are evaluated by removing them from the fit, and subtracting the overall uncertainty on μ without that parameter from with it in quadrature. The residual non-closure is due to correlations between the various nuisance parameters.

Source of Uncertainty	Impact on Background Estimate (%)
MC Statistics	3.48
Renormalisation Scale	1.83
Parton Shower and ME	2.11

Table 18: Pre-fit impact of the uncertainties described in Section 5 on the background estimate.
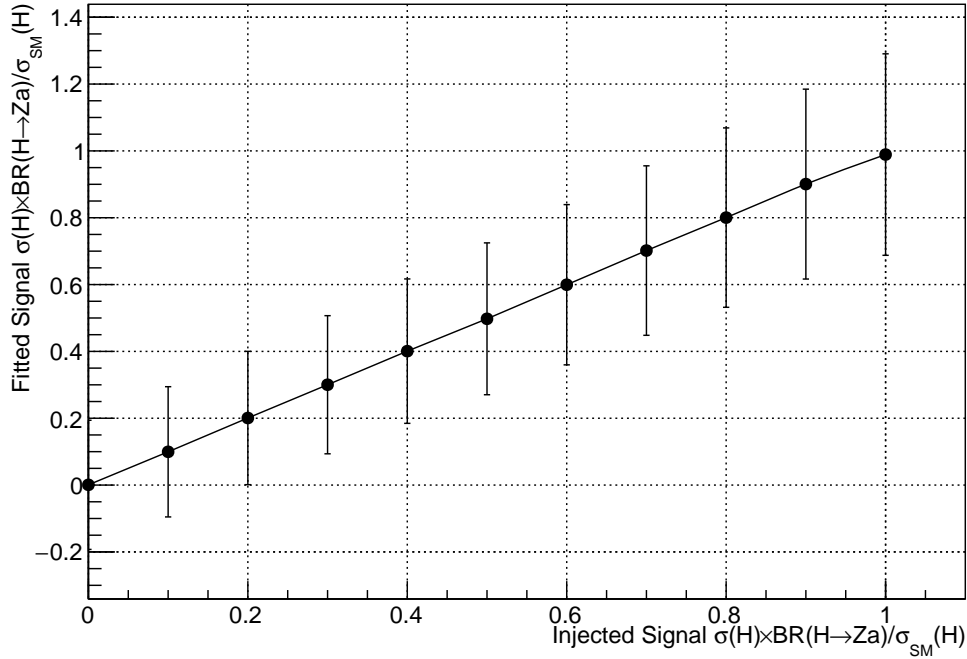
Figure 30: Plot of injected signal $\sigma(H) \times BR(H \to ZX)/\sigma_{\text{SM}}(H)$ against fitted signal $\sigma(H) \times BR(H \to ZX)/\sigma_{\text{SM}}(H)$ for the 1.5 GeV a signal hypothesis.

for any given sample, are the same as those for the inclusive decay for that sample. The motivation and justification for the fourth assumption is given in the next paragraph.

The efficiencies are then reevaluated for exclusive decays of the a to gluons, and either s- or c-quarks, as shown in Table 19. The decays to c-quarks occur only through charmonium resonances, for which the modelling is questionable. For this reason, the $a \to c\bar{c}$ results are not included in the paper. It can be seen that the efficiencies for quarks are consistently slightly higher than that for gluons. The limits from the inclusive search are then multiplied by the inclusive signal efficiency, and divided by the signal efficiencies to exclusive gluon or quark final states. These limits then represent the limits on $\sigma(H)\text{BR}(H \to Za) \times \text{BR}(a \to q/g)/\sigma_{\text{SM}}(H)$, under the assumption that the systematic uncertainties on the signal acceptance are the same for quark and gluon final states, and are given in Table 20. Model-independent limits on $\sigma(H)\text{BR}(H \to Za) \times \text{BR}(a \to q/g)$ in Table 21. This assumption allows the limit on any specific decay of the a to be calculated, by a linear superposition of the two exclusive limits, which would not be possible if the systematics were considered exclusively. The impact of the systematic uncertainties on the signal, which may vary between gluon or quark final states, has just a $\sim 2.1\%$ impact on the $\Delta\mu$ for the 1.5 GeV a signal hypothesis, justifying the assumption that these uncertainties can be approximated by their inclusive values. This only exception to this is for very low BR decays, such as the 8 GeV a to $c\bar{c}$, in which the signal MC statistical uncertainty could be much larger than in the inclusive case.

a mass / GeV	$a \to gg$	$a \to s\bar{s}$	$a \to c\bar{c}$
0.5	3.66 ± 0.08	-	-
0.75	2.97 ± 0.06	-	-
1	3.31 ± 0.06	-	-
1.5	2.74 ± 0.06	2.97 ± 0.13	-
2	2.13 ± 0.05	2.40 ± 0.13	-
2.5	1.36 ± 0.04	1.65 ± 0.14	-
3	0.727 ± 0.028	0.840 ± 0.089	-
3.5	0.475 ± 0.066	-	0.524 ± 0.023
4	0.162 ± 0.054	-	0.125 ± 0.014

Table 19: Efficiencies of the full selection (pre-selection and MLP requirement) for exclusive gluon or quark decays of each signal sample. The selection efficiencies for $a \to q\bar{q}$ decays are generally higher than $a \to gg$ due to a higher MLP cut efficiency.

a mass / GeV	$a \to gg$	$a \to s\bar{s}$	$a \to c\bar{c}$
0.5	$28.9^{+11.3}_{-8.1}$	-	-
0.75	$34.3^{+13.4}_{-9.6}$	-	-
1	$31.6^{+12.4}_{-8.8}$	-	-
1.5	$37.1^{+14.5}_{-10.4}$	$34.2^{+13.4}_{-9.6}$	-
2	$47.1^{+18.4}_{-13.2}$	$41.7^{+16.3}_{-11.7}$	-
2.5	$69.4^{+27.2}_{-19.4}$	$57.2^{+22.4}_{-16.0}$	-
3	135^{+53}_{-38}	117^{+46}_{-33}	-
3.5	207^{+81}_{-58}	-	188^{+74}_{-52}
4	584^{+229}_{-163}	-	755^{+296}_{-211}

Table 20: 95% CL_s upper limits on $\sigma(H) \times \mathcal{B}(H \to Za) \times \mathcal{B}(a \to q/g)/\sigma_{\mathrm{SM}}(H)$ expected in the absence of a signal. These results are derived for exclusive gluon or quark decays for each signal sample, using the Asimov dataset.

a mass / GeV	$a \to gg$	$a \to s\bar{s}$	$a \to c\bar{c}$
0.5	$16.1^{+6.3}_{-4.5}$	-	-
0.75	$18.9^{+7.4}_{-5.3}$	-	-
1	$17.3^{+6.8}_{-4.8}$	-	-
1.5	$20.4^{+8.0}_{-5.7}$	$18.9^{+7.4}_{-5.3}$	-
2	$25.9^{+10.1}_{-7.2}$	$22.9^{+9.0}_{-6.4}$	-
2.5	$38.3^{+15.0}_{-10.7}$	$31.6^{+12.4}_{-8.8}$	-
3	$74.6^{+29.2}_{-20.9}$	$64.6^{+25.3}_{-18.0}$	-
3.5	115^{+45}_{-32}	-	104^{+41}_{-29}
4	323^{+127}_{-90}	-	418^{+164}_{-117}

Table 21: 95% CL_s upper limits on $\sigma(H) \times \mathcal{B}(H \to Za) \times \mathcal{B}(a \to q/g)/\mathrm{pb}$ expected in the absence of a signal. These results are derived for exclusive gluon or quark decays for each signal sample, using the Asimov dataset.

7 Validation Strategy

A validation region is defined in the sideband of the MLP variable. It is as close as possible to the signal cut, containing the same amount of background as passes the signal cut. This includes all events with $0.0341 < MLP < 0.0524$. This region is used as a first validation of the analysis methods. This VR has an $S/\sqrt{B}$ improvement of less than 0.760 for all signal hypotheses, meaning that the full analysis can be performed in this VR as though it was the SR without unblinding the search.

89919 events were observed in this VR, to be compared with the background-only expectation of 88700 ± 2800 events. This region was fit with the full signal plus background hypothesis, including all the systematic uncertainties mentioned in Sections 5.1 and 5.2. The priors for the signal systematics were evaluated separately for this region. When fit with the 1.5 GeV a signal and background hypotheses, the best fit number of signal events was 997, with a best fit number of background events of 88900. The corresponding best fit values for the signal strength parameter is: $\mu = 0.160^{+0.667}_{-0.593}$. To test the relevant machinery, the 95% CL_s limit was found to be 131%. Figures 31 and 32 show the resulting pull plot and correlation matrix, respectively.
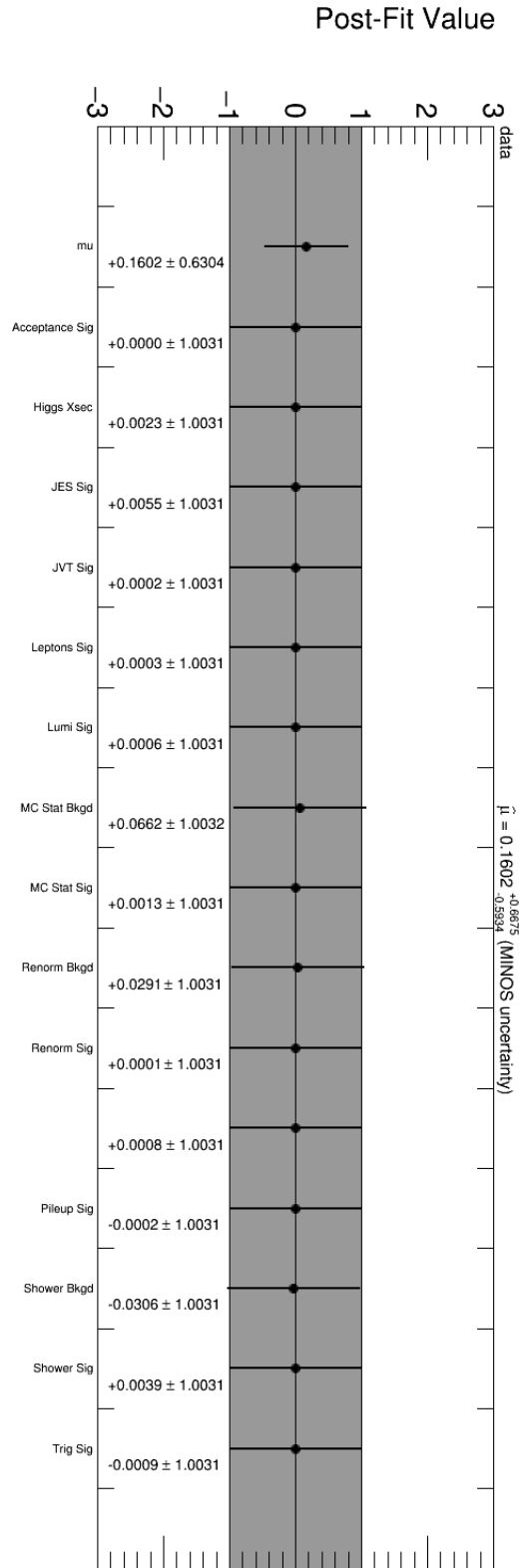
Figure 31: The pull plot for the fit to the data in the validation region using the 1.5 GeV *a* signal hypothesis, with systematics.
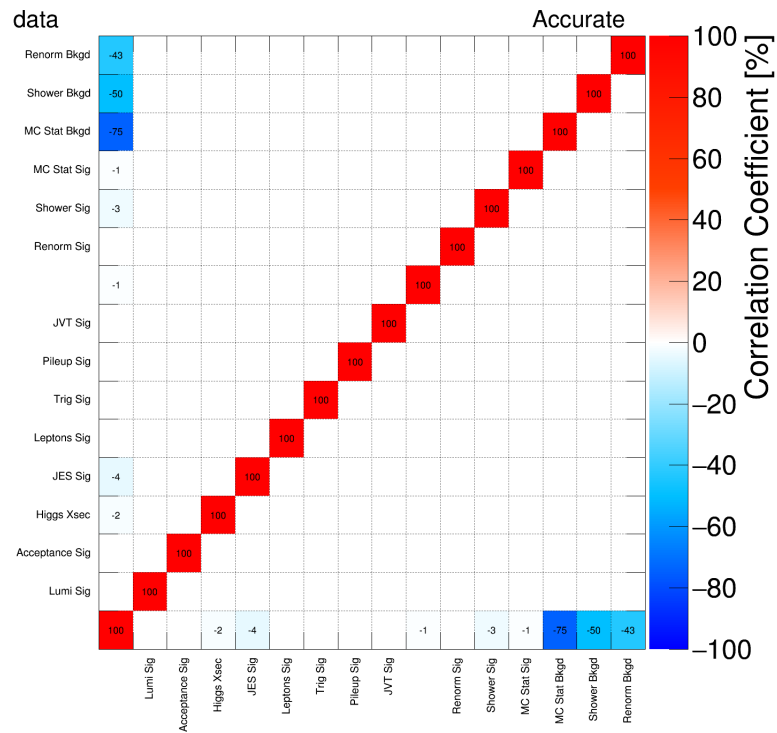
Figure 32: The correlation matrix for the fit to the data in the validation region using the 1.5 GeV a signal hypothesis, with systematics. Only entries with values greater than 0.5% are plotted.

8 Results

82908 events were observed in the signal region. This result is compatible with the SM background only expectation of $82400 \pm 3700 \, (2900 \oplus 2300)$ events, where the total uncertainty is followed by the uncertainty due to limited data and MC statistics, and then the systematic uncertainty. In the absence of a significant excess, 95% CL_s upper limits are set on $\sigma(H) \times \mathcal{B}(H \to Za)/\sigma_{SM}(H)$ and on $\sigma(H) \times \mathcal{B}(H \to Za)$, for both the nominal Pythia8 BRs, and the model independent interpretation described in Section 6.4. These are given in Table 22, and Tables 23 and 24, respectively. They are also given for the limits on $\sigma(H) \times \mathcal{B}(H \to Za)/\sigma_{SM}(H)$ in Figures 33 and Figures 34, respectively, and for the limits on $\sigma(H) \times \mathcal{B}(H \to Za)$ in Figure 35. In the absence of systematic uncertainties, these limits would range between 1.9 pb and 55 pb. The pull and correlation plots for the fit to the observed data are given for the 1.5 GeV a signal hypothesis in Figures 36 and 37, respectively. The regression MLP output and classification MLP outputs are given in Figure 38 for the events in the signal region. Finally, Figure 39 shows the three body mass distribution in the MLP signal region, without the three body mass cut applied.

a mass / GeV	μ (%)	95% CL_s Limit	
		μ (%)	$\sigma(H) \times \mathcal{B}(H \to Za)/$pb
0.5	$0.036^{+0.132}_{-0.168}$	34.0	18.8
0.75	$0.023^{+0.175}_{-0.176}$	38.8	21.5
1	$0.022^{+0.169}_{-0.170}$	38.3	21.2
1.5	$0.025^{+0.192}_{-0.195}$	42.8	23.7
2	$0.031^{+0.239}_{-0.241}$	52.5	29.1
2.5	$0.048^{+0.362}_{-0.368}$	75.7	41.9
3	$0.088^{+0.688}_{-0.694}$	149	82.3
3.5	$0.120^{+0.948}_{-0.952}$	206	113
4	$0.43^{+3.40}_{-3.43}$	710	392
η_c	$0.113^{+0.876}_{-0.883}$	193	107
J/ψ	$0.107^{+0.867}_{-0.864}$	189	105

Table 22: The observed model-dependent signal strength parameters and 95% CL_s upper limits on $\sigma(H) \times \mathcal{B}(H \to Za)/\sigma_{SM}(H)$ and $\sigma(H) \times \mathcal{B}(H \to Za)$ for the observed dataset. Pythia8 a BRs are assumed, using the default BSMHiggs $\tan \beta$ value of 1, as given in Table 3.

a mass / GeV	$a \to gg$	$a \to s\bar{s}$	$a \to c\bar{c}$
0.5	30.4	-	-
0.75	36.1	-	-
1	33.0	-	-
1.5	39.0	36.0	-
2	49.4	43.8	-
2.5	72.7	59.9	-
3	142	123	-
3.5	219	-	198
4	614	-	793

Table 23: 95% CL_s observed upper limits on $\sigma(H) \times \mathcal{B}(H \to Za) \times \mathcal{B}(a \to q/g)/\sigma_{SM}(H)$. These results are derived for exclusive gluon or quark decays for each signal sample.
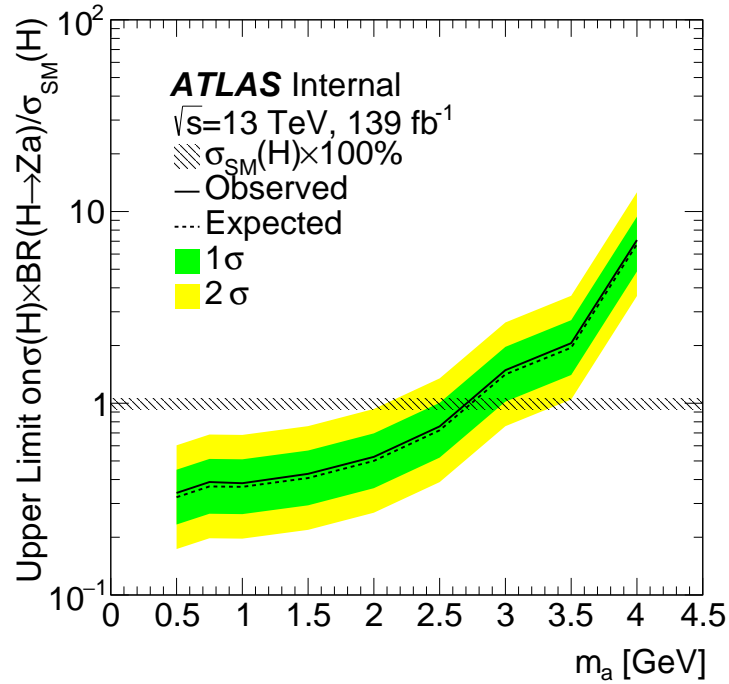
a mass / GeV	$a \to gg$	$a \to s\bar{s}$	$a \to c\bar{c}$
0.5	16.8	-	-
0.75	20.0	-	-
1	18.2	-	-
1.5	21.6	19.9	-
2	27.3	24.2	-
2.5	40.2	33.1	-
3	78.4	67.8	-
3.5	121	-	109
4	339	-	438

Table 24: 95% CL$_s$ observed upper limits on $\sigma(H) \times \mathcal{B}(H \to Za) \times \mathcal{B}(a \to q/g)$/pb. These results are derived for exclusive gluon or quark decays for each signal sample.

Figure 33: 95% CL$_s$ observed, and median expected upper limits on $\sigma(H)\mathrm{BR}(H \to Za)/\sigma_{\mathrm{SM}}(H)$. The 1σ and 2σ bands are also shown. The limits are taken from linearly interpolating between the points for which MC signal samples are generated.
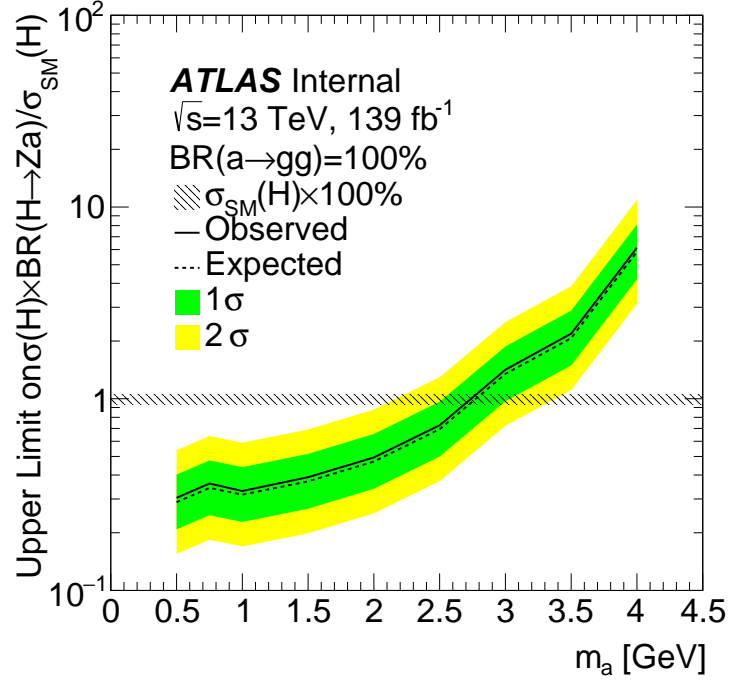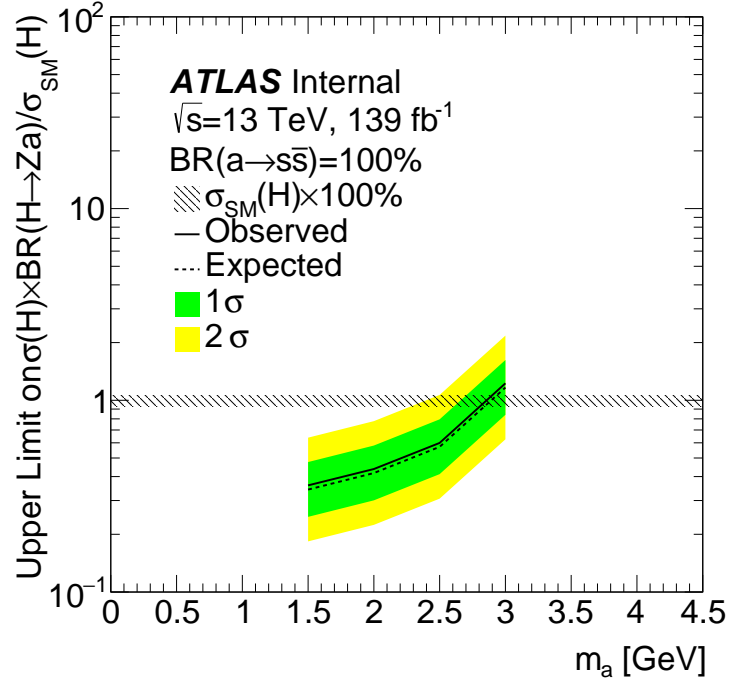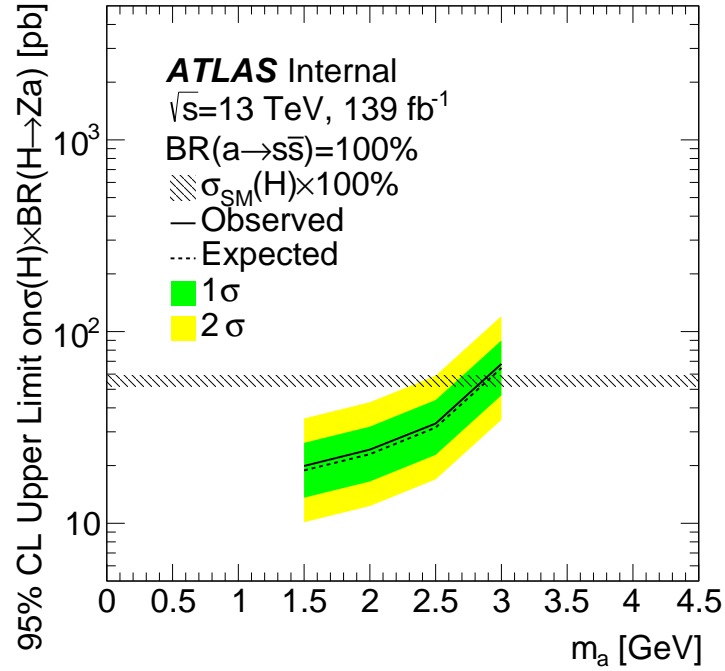
(a) $a \to gg$

(b) $a \to q\bar{q}$

Figure 34: Model-independent 95% CL$_s$ observed, and median expected upper limits on $\sigma(H)\mathrm{BR}(H \to Za)/\sigma_{\mathrm{SM}}(H)$, for (a) $a \to gg$ and (b) $a \to q\bar{q}$ signals. The 1σ and 2σ bands are also shown. The limits are taken from linearly interpolating between the points for which MC signal samples are generated.
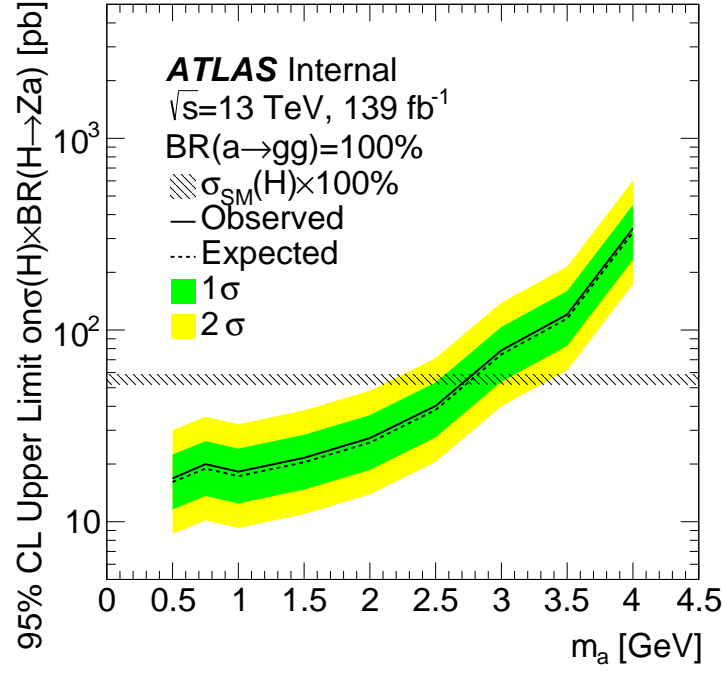
(a) $a \to gg$

(b) $a \to q\bar{q}$

Figure 35: Model-independent 95% CL_s observed, and median expected upper limits on $\sigma(H) \times \mathcal{B}(H \to Za)$, for (a) $a \to gg$ and (b) $a \to q\bar{q}$ signals. The 1σ and 2σ bands are also shown. The limits are taken from linearly interpolating between the points for which MC signal samples are generated.
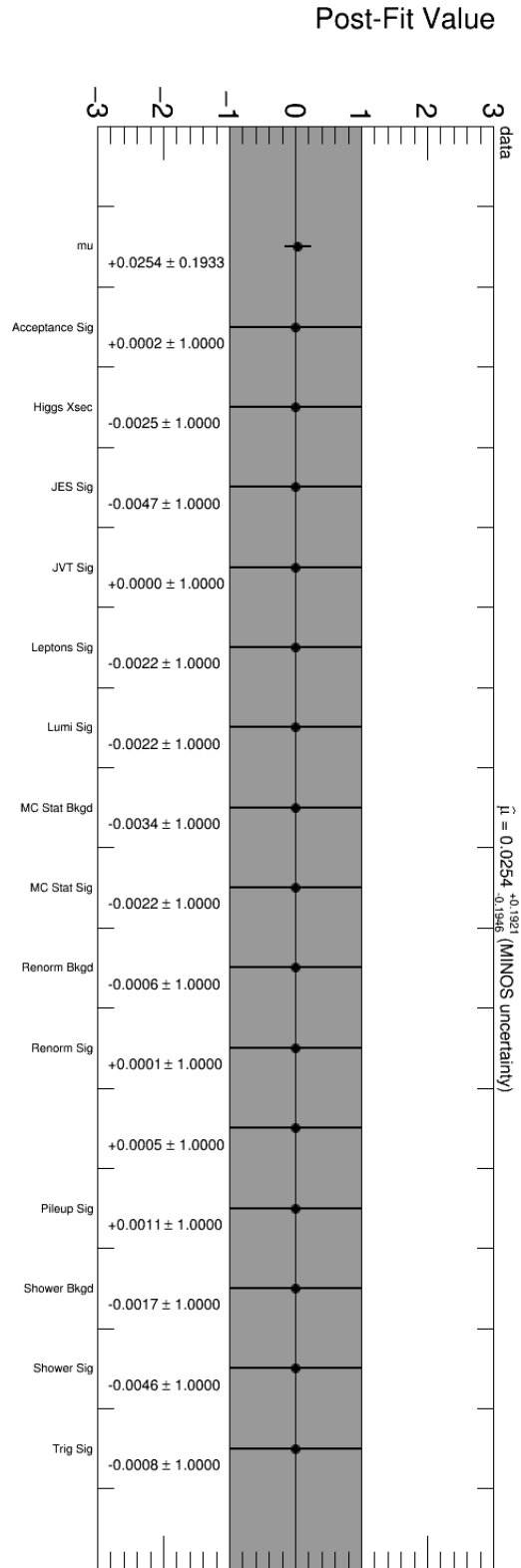
Figure 36: The pull plot for the fit to the data in the signal region using the 1.5 GeV a signal hypothesis, with systematics. Pythia8 a BRs are assumed, using the default BSMHiggs $\tan\beta$ value of 1, as given in Table 3.
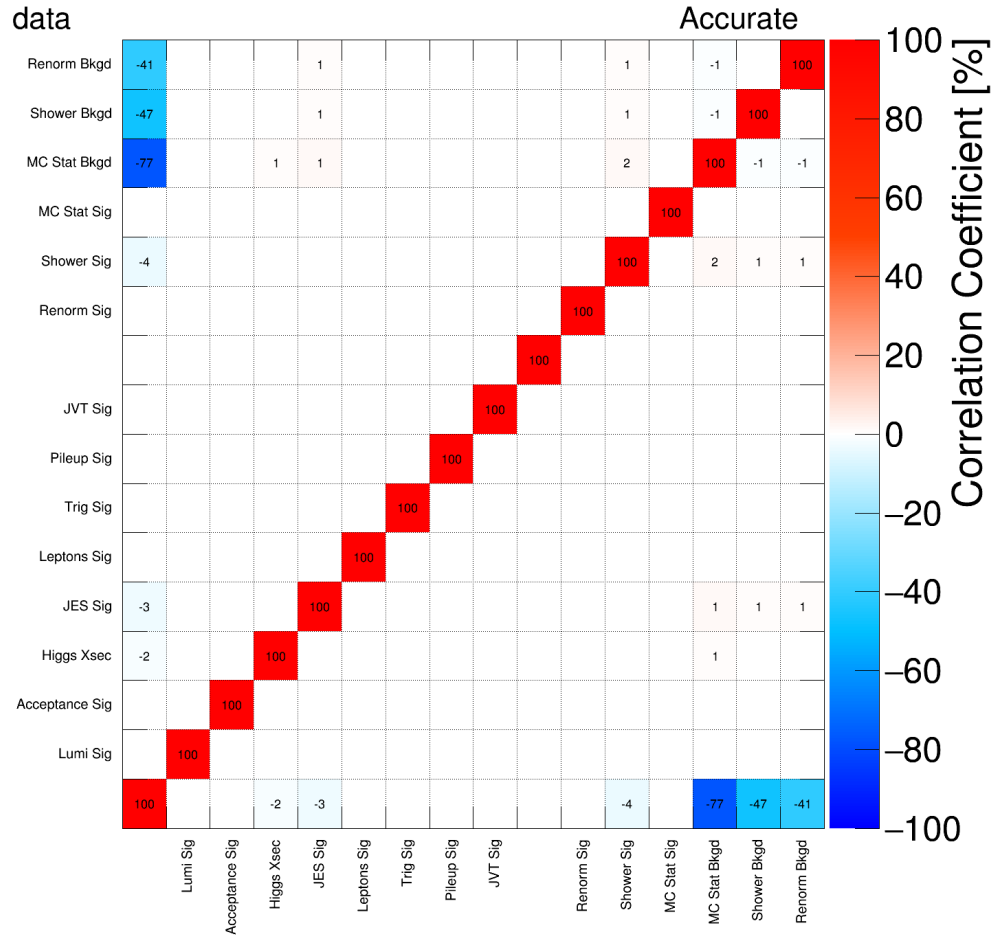
Figure 37: The correlation matrix for the fit to the data in the signal region using the 1.5 GeV *a* signal hypothesis, with systematics. Only entries with values greater than 0.5% are plotted. PYTHIA8 *a* BRs are assumed, using the default BSMHIGGS tan β value of 1, as given in Table 3.
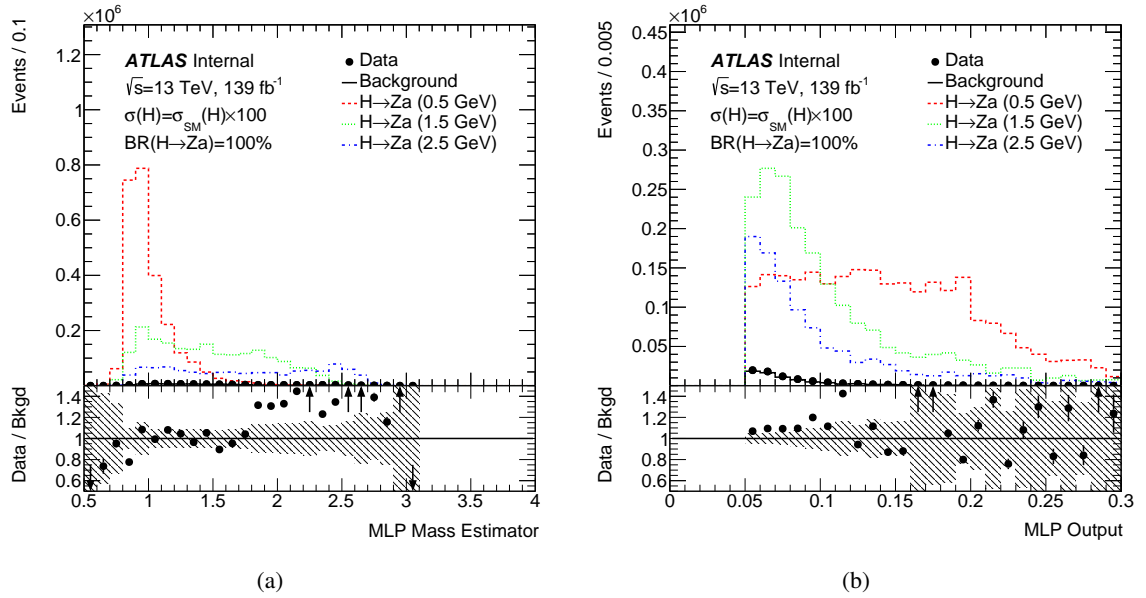
Figure 38: Distributions of the (a) regression MLP output and (b) classification MLP outputs for the unblinded data, reweighted background and various signal hypotheses, in the signal region.
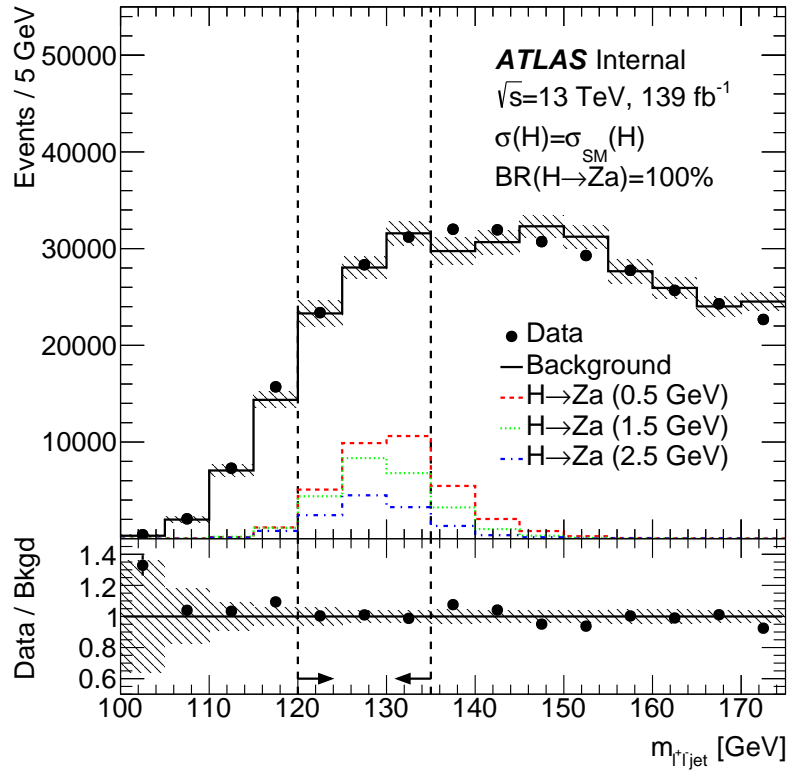
Figure 39: Invariant mass of the di-lepton plus jet system, for data, background and three signal hypotheses. Events are required to pass the the complete event selection, including the MLP output variable requirement, but not the 120 GeV $< m_{\ell^+ \ell^- j} <$ 135 GeV requirement. The background normalisation is set equal to that of the data, and the signal normalisations assume the SM Higgs production cross section and $\mathcal{B}(H \to Za) = 100\%$. The background in these distributions has been reweighted as per Section 4.2.1. The error bars are the data statistical uncertainty, and the dashed bars are the MC statistical uncertainty. The region between the dashed lines is the signal region.

9 Conclusion

A search has been performed, which probes Higgs boson decays to a Z boson, and a J/ψ or η_c charmonium state, or an a. It is well-motivated both in the SM, and from its sensitivity to non-SM final states. No excess is observed. 95% CL$_s$ upper limits are set on $\sigma(pp \rightarrow H)\mathcal{B}(H \rightarrow Z(a/Q))$, with values starting from 16.8 pb for the signal hypothesis of a 0.5 GeV a decaying to gluons, and 105 pb and 107 pb for the J/ψ and η_c, respectively. This is the first direct limit on hadronic decays of a non-SM Higgs boson over this mass range. Due to the large value of $\mathcal{B}(a \rightarrow \text{hadrons})$ over the entire 2HDM(+S) phase space, these limits represent the tightest direct constraints for low (high) $\tan \beta$ in the Type-II and type-II (Type-VI) 2HDM+S [84].

References

[1] ATLAS Collaboration,
    Observation of $H \rightarrow b\bar{b}$ decays and VH production with the ATLAS detector,
    Phys. Lett. **B786** (2018) 59, arXiv: 1808.08238 [hep-ex].

[2] CMS Collaboration, *Observation of Higgs boson decay to bottom quarks*,
    Phys. Rev. Lett. **121** (2018) 121801, arXiv: 1808.08242 [hep-ex].

[3] ATLAS Collaboration, *Observation of Higgs boson production in association with a top quark pair at the LHC with the ATLAS detector*, Phys. Lett. **B784** (2018) 173, arXiv: 1806.00425 [hep-ex].

[4] CMS Collaboration, *Observation of t$\bar{\text{t}}$H production*, Phys. Rev. Lett. **120** (2018) 231801,
    arXiv: 1804.02610 [hep-ex].

[5] Particle Data Group, *Review of Particle Physics*, Phys. Rev. D **98** (3 2018) 030001,
    URL: {https://link.aps.org/doi/10.1103/PhysRevD.98.030001}.

[6] G. T. Bodwin, F. Petriello, S. Stoynev and M. Velasco,
    Higgs boson decays to quarkonia and the $H\bar{c}c$ coupling, Phys. Rev. **D88** (2013) 053003,
    arXiv: 1306.5770 [hep-ph].

[7] A. L. Kagan et al., *Exclusive Window onto Higgs Yukawa Couplings*,
    Phys. Rev. Lett. **114** (2015) 101802, arXiv: 1406.1722 [hep-ph].

[8] A. S. Chisholm, S. Kuttimalai, K. Nikolopoulos and M. Spannowsky,
    Measuring rare and exclusive Higgs boson decays into light resonances,
    Eur. Phys. J. **C76** (2016) 501, arXiv: 1606.09177 [hep-ph].

[9] ATLAS Collaboration, *Searches for exclusive Higgs and Z boson decays into $J/\psi\gamma$, $\psi(2S)\gamma$, and $\Upsilon(nS)\gamma$ at $\sqrt{s} = 13$ TeV with the ATLAS detector*, Phys. Lett. **B786** (2018) 134,
    arXiv: 1807.00802 [hep-ex].

[10] ATLAS Collaboration,
    Search for exclusive Higgs and Z boson decays to $\phi\gamma$ and $\rho\gamma$ with the ATLAS detector,
    JHEP **07** (2018) 127, arXiv: 1712.02758 [hep-ex].

[11] ATLAS Collaboration, *Search for Higgs and Z Boson Decays to $\phi\gamma$ with the ATLAS Detector*,
    Phys. Rev. Lett. **117** (2016) 111802, arXiv: 1607.03400 [hep-ex].

[12] ATLAS Collaboration,
Search for Higgs and Z Boson Decays to J/ψγ and Υ(nS)γ with the ATLAS Detector,
Phys. Rev. Lett. **114** (2015) 121801, arXiv: 1501.03276 [hep-ex].

[13] ATLAS Collaboration,
Search for the Decay of the Higgs Boson to Charm Quarks with the ATLAS Experiment,
Phys. Rev. Lett. **120** (2018) 211802, arXiv: 1802.04329 [hep-ex].

[14] G. Isidori, A. V. Manohar and M. Trott,
Probing the nature of the Higgs-like Boson via $h \rightarrow V\mathcal{F}$ decays, Phys. Lett. **B728** (2014) 131,
arXiv: 1305.0663 [hep-ph].

[15] S. Alte, M. König and M. Neubert,
Exclusive Weak Radiative Higgs Decays in the Standard Model and Beyond, JHEP **12** (2016) 037,
arXiv: 1609.06310 [hep-ph].

[16] D. Curtin et al., *Exotic decays of the 125 GeV Higgs boson*, Phys. Rev. D **90** (7 2014) 075004,
URL: {https://link.aps.org/doi/10.1103/PhysRevD.90.075004}.

[17] A. Belyaev et al.,
LHC discovery potential of the lightest NMSSM Higgs in the h1 → a1 a1 → 4 muons channel,
Phys. Rev. **D81** (2010) 075021, arXiv: 1002.1956 [hep-ph].

[18] J. F. Gunion and H. E. Haber,
The CP conserving two Higgs doublet model: The Approach to the decoupling limit,
Phys. Rev. **D67** (2003) 075019, arXiv: hep-ph/0207010 [hep-ph].

[19] K. S. Babu and Y. Mimura,
Solving the muon problem in gauge mediated supersymmetry breaking models with flavor symmetry,
(2001), arXiv: hep-ph/0101046 [hep-ph].

[20] D. Curtin et al., *Exotic decays of the 125 GeV Higgs boson*, Phys. Rev. **D90** (2014) 075004,
arXiv: 1312.4992 [hep-ph].

[21] CMS Collaboration, *Search for the exotic decay of the Higgs boson to two light pseudoscalar
bosons with two taus and two muons in the final state at $\sqrt{s}$ = 8 TeV*,
tech. rep. CMS-PAS-HIG-15-011, CERN, 2016,
URL: https://cds.cern.ch/record/2128149.

[22] CMS Collaboration, *Search for exotic decays of the Higgs boson to a pair of new light bosons with
two muon and two b jets in final states*, tech. rep. CMS-PAS-HIG-14-041, CERN, 2016,
URL: https://cds.cern.ch/record/2135985.

[23] CMS Collaboration, *Search for a very light NMSSM Higgs boson produced in decays of the 125
GeV scalar boson and decaying into τ leptons in pp collisions at $\sqrt{s}$ = 8 TeV*, JHEP **01** (2016) 079,
arXiv: 1510.06534 [hep-ex].

[24] CMS Collaboration, *Search for Higgs Decays to New Light Bosons in Boosted Tau Final States*,
tech. rep. CMS-PAS-HIG-14-022, CERN, 2015,
URL: https://cds.cern.ch/record/2058768.

[25] CMS Collaboration, *A search for pair production of new light bosons decaying into muons*,
Phys. Lett. **B752** (2016) 146, arXiv: 1506.00424 [hep-ex].

[26] ATLAS Collaboration, *Search for Higgs bosons decaying to aa in the μμττ final state in pp
collisions at $\sqrt{s}$=8 TeV with the ATLAS experiment*, Phys. Rev. **D92** (2015).

[27] M. Aaboud et al., *Search for the Higgs boson produced in association with a W boson and decaying to four b-quarks via two spin-zero particles in pp collisions at 13 TeV with the ATLAS detector*, Eur. Phys. J. **C76** (2016) 605, arXiv: 1606.08391 [hep-ex].

[28] M. Aaboud et al., *Search for Higgs boson decays to beyond-the-Standard-Model light bosons in four-lepton events with the ATLAS detector at $\sqrt{s}$ = 13 TeV*, JHEP **06** (2018) 166, arXiv: 1802.03388 [hep-ex].

[29] M. Aaboud et al., *Search for Higgs boson decays into a pair of light bosons in the bbμμ final state in pp collision at $\sqrt{s}$ =13 TeV with the ATLAS detector*, Phys. Lett. **B790** (2019) 1, arXiv: 1807.00539 [hep-ex].

[30] M. Aaboud et al., *Search for Higgs boson decays into pairs of light (pseudo)scalar particles in the γγjj final state in pp collisions at $\sqrt{s}$ = 13 TeV with the ATLAS detector*, Phys. Lett. **B782** (2018) 750, arXiv: 1803.11145 [hep-ex].

[31] G. Aad et al., *Search for new phenomena in events with at least three photons collected in pp collisions at $\sqrt{s}$ = 8 TeV with the ATLAS detector*, Eur. Phys. J. **C76** (2016) 210, arXiv: 1509.05051 [hep-ex].

[32] V. M. Abazov et al., *Search for NMSSM Higgs bosons in the h —> aa —> mu mu mu mu, mu mu tau tau channels using p anti-p collisions at s**(1/2) = 1.96-TeV*, Phys. Rev. Lett. **103** (2009) 061801, arXiv: 0905.3381 [hep-ex].

[33] A. Falkowski, F. Riva and A. Urbano, *Higgs at last*, JHEP **11** (2013) 111, arXiv: 1303.1812 [hep-ph].

[34] P. Nason, *A New method for combining NLO QCD with shower Monte Carlo algorithms*, JHEP **11** (2004) 040, arXiv: hep-ph/0409146 [hep-ph].

[35] S. Frixione, P. Nason and C. Oleari, *Matching NLO QCD computations with Parton Shower simulations: the POWHEG method*, JHEP **11** (2007) 070, arXiv: 0709.2092 [hep-ph].

[36] S. Alioli, P. Nason, C. Oleari and E. Re, *A general framework for implementing NLO calculations in shower Monte Carlo programs: the POWHEG BOX*, JHEP **06** (2010) 043, arXiv: 1002.2581 [hep-ph].

[37] G. Aad et al., *Measurement of the Z/γ^* boson transverse momentum distribution in pp collisions at $\sqrt{s}$ = 7 TeV with the ATLAS detector*, JHEP **09** (2014) 145, arXiv: 1406.3660 [hep-ex].

[38] T. Sjostrand, S. Mrenna and P. Z. Skands, *A Brief Introduction to PYTHIA 8.1*, Comput. Phys. Commun. **178** (2008) 852, arXiv: 0710.3820 [hep-ph].

[39] A. Ryd et al., *EvtGen: A Monte Carlo Generator for B-Physics*, (2005).

[40] H.-L. Lai et al., *New parton distributions for collider physics*, Phys. Rev. **D82** (2010) 074024, arXiv: 1007.2241 [hep-ph].

[41] *Monte Carlo Generators for the Production of a W or Z/γ^* Boson in Association with Jets at ATLAS in Run 2*, tech. rep. ATL-PHYS-PUB-2016-003, CERN, 2016, URL: https://cds.cern.ch/record/2120133.

[42] T. Gleisberg et al., *Event generation with SHERPA 1.1*, Journal of High Energy Physics **2009** (2009) 007, URL: http://stacks.iop.org/1126-6708/2009/i=02/a=007.

[43] R. D. Ball et al., *Parton distributions with LHC data*, Nucl. Phys. **B867** (2013) 244,
arXiv: 1207.1303 [hep-ph].

[44] J Butterworth et al.,
Single Boson and Diboson Production Cross Sections in pp Collisions at sqrts=7 TeV,
tech. rep. ATL-COM-PHYS-2010-695, CERN, 2010,
URL: https://cds.cern.ch/record/1287902.

[45] *Multi-Boson Simulation for 13 TeV ATLAS Analyses*, tech. rep. ATL-PHYS-PUB-2017-005,
CERN, 2017, URL: https://cds.cern.ch/record/2261933.

[46] The ATLAS Collaboration, *The ATLAS Simulation Infrastructure*,
The European Physical Journal C **70** (2010) 823, ISSN: 1434-6052,
URL: https://doi.org/10.1140/epjc/s10052-010-1429-9.

[47] *Geant4—a simulation toolkit*, Nuclear Instruments and Methods in Physics Research Section A:
Accelerators, Spectrometers, Detectors and Associated Equipment **506** (2003) 250 ,
ISSN: 0168-9002,
URL: http://www.sciencedirect.com/science/article/pii/S0168900203013688.

[48] A. Collaboration, *https://twiki.cern.ch/twiki/bin/view/Atlas/TrigDecisionTool*, (2018),
URL: https://twiki.cern.ch/twiki/bin/view/Atlas/TrigDecisionTool (visited on
04/04/2019).

[49] A. Collaboration, *https://twiki.cern.ch/twiki/bin/view/Atlas/XAODMatchingTool*, (2016),
URL: https://twiki.cern.ch/twiki/bin/view/Atlas/XAODMatchingTool (visited on
04/04/2019).

[50] ATLAS Collaboration, *Electron reconstruction and identification efficiency measurements with the
ATLAS detector using the 2011 LHC proton-proton collision data*, Eur. Phys. J. **C74** (2014) 2941,
arXiv: 1404.2240 [hep-ex].

[51] A. Collaboration, *https://twiki.cern.ch/twiki/bin/view/AtlasProtected/EGammaIdentificationRun2*,
(2019), URL: https://twiki.cern.ch/twiki/bin/view/AtlasProtected/
EGammaIdentificationRun2#Electron_Identification (visited on 04/04/2019).

[52] A. Collaboration, *https://twiki.cern.ch/twiki/bin/view/AtlasProtected/IsolationSelectionTool*, (2019),
URL:
https://twiki.cern.ch/twiki/bin/view/AtlasProtected/IsolationSelectionTool
(visited on 04/04/2019).

[53] A. Collaboration,
https://twiki.cern.ch/twiki/bin/view/AtlasProtected/LatestRecommendationsElectronIDRun2,
(2019), URL: https://twiki.cern.ch/twiki/bin/view/AtlasProtected/
LatestRecommendationsElectronIDRun2 (visited on 04/04/2019).

[54] A. Collaboration, *https://twiki.cern.ch/twiki/bin/view/AtlasProtected/EGammaCalibrationRun2*,
(2016), URL:
https://twiki.cern.ch/twiki/bin/view/AtlasProtected/EGammaCalibrationRun2
(visited on 04/04/2019).

[55] ATLAS Collaboration, *Measurement of the muon reconstruction performance of the ATLAS
detector using 2011 and 2012 LHC proton–proton collision data*, Eur. Phys. J. **C74** (2014) 3130,
arXiv: 1407.3935 [hep-ex].

[56] A. Collaboration, *https://twiki.cern.ch/twiki/bin/view/Atlas/MuonSelectionToolR21*, (2018),
URL: https://twiki.cern.ch/twiki/bin/view/Atlas/MuonSelectionToolR21 (visited
on 04/04/2019).

[57] A. Collaboration,
https://twiki.cern.ch/twiki/bin/view/AtlasProtected/MCPAnalysisConsolidationMC16, (2019),
URL: https:
//twiki.cern.ch/twiki/bin/view/AtlasProtected/MCPAnalysisConsolidationMC16
(visited on 04/04/2019).

[58] A. Collaboration, *https://twiki.cern.ch/twiki/bin/view/AtlasProtected/MCPAnalysisGuidelinesMC16*,
(2018), URL: https://twiki.cern.ch/twiki/bin/view/AtlasProtected/
MCPAnalysisGuidelinesMC16#Momentum_corrections (visited on 04/04/2019).

[59] A. Collaboration, *https://twiki.cern.ch/twiki/bin/view/AtlasProtected/ApplyJetCalibrationR21*,
(2019), URL:
https://twiki.cern.ch/twiki/bin/view/AtlasProtected/ApplyJetCalibrationR21
(visited on 04/04/2019).

[60] *Selection of jets produced in 13TeV proton-proton collisions with the ATLAS detector*,
tech. rep. ATLAS-CONF-2015-029, CERN, 2015,
URL: https://cds.cern.ch/record/2037702.

[61] T. Masubuchi et al., *Search for a Standard Model Higgs boson produced in association with a
vector boson and decaying to a pair of b-quarks*, tech. rep. ATL-COM-PHYS-2016-1724,
CERN, 2016, URL: https://cds.cern.ch/record/2235437.

[62] D Adams et al.,
Recommendations of the Physics Objects and AnalysisHarmonisation Study Groups 2014,
tech. rep. ATL-PHYS-INT-2014-018, CERN, 2014,
URL: https://cds.cern.ch/record/1743654.

[63] M. Cacciari and G. P. Salam, *Pileup subtraction using jet areas*, Phys. Lett. **B659** (2008) 119,
arXiv: 0707.1378 [hep-ph].

[64] A. Collaboration, *https://twiki.cern.ch/twiki/bin/view/AtlasProtected/InDetTrackSelectionTool*,
(2017), URL: https:
//twiki.cern.ch/twiki/bin/view/AtlasProtected/InDetTrackSelectionTool
(visited on 04/04/2019).

[65] A. Collaboration, *https://twiki.cern.ch/twiki/bin/view/AtlasProtected/TrackVertexAssociationTool*,
(2015), URL: https:
//twiki.cern.ch/twiki/bin/view/AtlasProtected/TrackVertexAssociationTool
(visited on 04/04/2019).

[66] J. Thaler and K. Van Tilburg, *Identifying Boosted Objects with N-subjettiness*, JHEP **03** (2011) 015,
arXiv: 1011.2268 [hep-ph].

[67] I. Moult, L. Necib and J. Thaler, *New Angles on Energy Correlation Functions*,
JHEP **12** (2016) 153, arXiv: 1609.07483 [hep-ph].

[68] L. G. Almeida et al., *Substructure of high-p_T Jets at the LHC*, Phys. Rev. **D79** (2009) 074017,
arXiv: 0807.0234 [hep-ph].

[69] J. de Favereau et al.,
DELPHES 3, A modular framework for fast simulation of a generic collider experiment,
JHEP **02** (2014) 057, arXiv: 1307.6346 [hep-ex].

[70] CERN Higgs Cross Section Working Group,
https://twiki.cern.ch/twiki/bin/view/LHCPhysics/CERNYellowReportPageAt1314TeV2014, (2016),
URL: https://twiki.cern.ch/twiki/bin/view/LHCPhysics/
CERNYellowReportPageAt1314TeV2014 (visited on 04/04/2019).

[71] Particle Data Group, *http://pdg.lbl.gov/2018/tables/rpp2018-sum-gauge-higgs-bosons.pdf*, (2018),
URL: http://pdg.lbl.gov/2018/tables/rpp2018-sum-gauge-higgs-bosons.pdf
(visited on 04/04/2019).

[72] S. Dittmaier et al., *Handbook of LHC Higgs Cross Sections: 1. Inclusive Observables*, (2011),
arXiv: 1101.0593 [hep-ph].

[73] S. Dittmaier et al., *Handbook of LHC Higgs Cross Sections: 2. Differential Distributions*, (2012),
arXiv: 1201.3084 [hep-ph].

[74] A. Collaboration, *https://twiki.cern.ch/twiki/bin/view/AtlasProtected/JetUncertainties*, (2018),
URL: https://twiki.cern.ch/twiki/bin/view/AtlasProtected/JetUncertainties.

[75] W. Buttinger, *Using Event Weights to account for differences in Instantaneous Luminosity and
Trigger Prescale in Monte Carlo and Data*, tech. rep. ATL-COM-SOFT-2015-119, CERN, 2015,
URL: https://cds.cern.ch/record/2014726.

[76] ATLAS Collaboration,
Luminosity determination in pp collisions at $\sqrt{s}$ = 8 TeV using the ATLAS detector at the LHC,
Eur. Phys. J. C **76** (2016) 653, arXiv: 1608.03953 [hep-ex].

[77] G. Avoni et al., *The new LUCID-2 detector for luminosity measurement and monitoring in ATLAS*,
JINST **13** (2018) P07017.

[78] A. Collaboration, *https://twiki.cern.ch/twiki/bin/view/AtlasProtected/JVTCalibrationRel21*, (2018),
URL:
https://twiki.cern.ch/twiki/bin/view/AtlasProtected/JVTCalibrationRel21
(visited on 04/04/2019).

[79] A. Collaboration, *https://twiki.cern.ch/twiki/bin/view/Atlas/TrigGlobalEfficiencyCorrectionTool*,
(2018), URL: https:
//twiki.cern.ch/twiki/bin/view/Atlas/TrigGlobalEfficiencyCorrectionTool
(visited on 04/04/2019).

[80] A. Collaboration,
https://twiki.cern.ch/twiki/bin/view/Atlas/MuonTriggerPhysicsRecommendationsRel212017,
(2019), URL: https://twiki.cern.ch/twiki/bin/view/Atlas/
MuonTriggerPhysicsRecommendationsRel212017 (visited on 04/04/2019).

[81] A. Collaboration, *https://twiki.cern.ch/twiki/bin/view/AtlasProtected/TrackingCPRecsRun2Final*,
(2018), URL: https:
//twiki.cern.ch/twiki/bin/view/AtlasProtected/TrackingCPRecsRun2Final
(visited on 04/04/2019).

[82] G. Cowan, K. Cranmer, E. Gross and O. Vitells,
Asymptotic formulae for likelihood-based tests of new physics,
Eur. Phys. J. **C71** (2011) 1554, [Erratum: Eur. Phys. J.C73,2501(2013)],
arXiv: `1007.1727 [physics.data-an]`.

[83] A. L. Read, *Presentation of search results: the CL$_s$ technique*,
Journal of Physics G: Nuclear and Particle Physics **28** (2002) 2693,
URL: `https://doi.org/10.1088%2F0954-3899%2F28%2F10%2F313`.

[84] ATLAS Collaboration, *Exotic Higgs Decay Summary Plots*, tech. rep. ATL-PHYS-PUB-2018-045,
CERN, 2018, URL: `http://cds.cern.ch/record/2650740`.

1276 Appendices

A Data Samples

Tables 25 shows the datasets used in this search.

2015 Samples
data15_13TeV.periodD.physics_Main.PhysCont.DAOD_FTAG2.grp15_v02_p3704
data15_13TeV.periodE.physics_Main.PhysCont.DAOD_FTAG2.grp15_v02_p3704
data15_13TeV.periodF.physics_Main.PhysCont.DAOD_FTAG2.grp15_v02_p3704
data15_13TeV.periodG.physics_Main.PhysCont.DAOD_FTAG2.grp15_v02_p3704
data15_13TeV.periodH.physics_Main.PhysCont.DAOD_FTAG2.grp15_v02_p3704
data15_13TeV.periodJ.physics_Main.PhysCont.DAOD_FTAG2.grp15_v02_p3704
2016 Samples
data16_13TeV.periodA.physics_Main.PhysCont.DAOD_FTAG2.grp16_v02_p3704
data16_13TeV.periodB.physics_Main.PhysCont.DAOD_FTAG2.grp16_v02_p3704
data16_13TeV.periodC.physics_Main.PhysCont.DAOD_FTAG2.grp16_v02_p3704
data16_13TeV.periodD.physics_Main.PhysCont.DAOD_FTAG2.grp16_v02_p3704
data16_13TeV.periodE.physics_Main.PhysCont.DAOD_FTAG2.grp16_v02_p3704
data16_13TeV.periodF.physics_Main.PhysCont.DAOD_FTAG2.grp16_v02_p3704
data16_13TeV.periodG.physics_Main.PhysCont.DAOD_FTAG2.grp16_v02_p3704
data16_13TeV.periodI.physics_Main.PhysCont.DAOD_FTAG2.grp16_v02_p3704
data16_13TeV.periodK.physics_Main.PhysCont.DAOD_FTAG2.grp16_v02_p3704
data16_13TeV.periodL.physics_Main.PhysCont.DAOD_FTAG2.grp16_v02_p3704
2017 Samples
data17_13TeV.periodB.physics_Main.PhysCont.DAOD_FTAG2.grp17_v02_p3704
data17_13TeV.periodC.physics_Main.PhysCont.DAOD_FTAG2.grp17_v02_p3704
data17_13TeV.periodD.physics_Main.PhysCont.DAOD_FTAG2.grp17_v02_p3704
data17_13TeV.periodE.physics_Main.PhysCont.DAOD_FTAG2.grp17_v02_p3704
data17_13TeV.periodF.physics_Main.PhysCont.DAOD_FTAG2.grp17_v02_p3704
data17_13TeV.periodH.physics_Main.PhysCont.DAOD_FTAG2.grp17_v02_p3704
data17_13TeV.periodI.physics_Main.PhysCont.DAOD_FTAG2.grp17_v02_p3704
data17_13TeV.periodK.physics_Main.PhysCont.DAOD_FTAG2.grp17_v02_p3704
2018 Samples
data18_13TeV.periodB.physics_Main.PhysCont.DAOD_FTAG2.grp18_v04_p3704
data18_13TeV.periodC.physics_Main.PhysCont.DAOD_FTAG2.grp18_v04_p3704
data18_13TeV.periodD.physics_Main.PhysCont.DAOD_FTAG2.grp18_v04_p3704
data18_13TeV.periodF.physics_Main.PhysCont.DAOD_FTAG2.grp18_v04_p3704
data18_13TeV.periodI.physics_Main.PhysCont.DAOD_FTAG2.grp18_v04_p3704
data18_13TeV.periodK.physics_Main.PhysCont.DAOD_FTAG2.grp18_v04_p3704
data18_13TeV.periodL.physics_Main.PhysCont.DAOD_FTAG2.grp18_v04_p3704
data18_13TeV.periodM.physics_Main.PhysCont.DAOD_FTAG2.grp18_v04_p3704
data18_13TeV.periodO.physics_Main.PhysCont.DAOD_FTAG2.grp18_v04_p3704
data18_13TeV.periodQ.physics_Main.PhysCont.DAOD_FTAG2.grp18_v04_p3704

Table 25: Full list of Run 2 data samples.

B Monte-Carlo Simulation Signal Samples

Tables 26, 27 and 28 list the MC signal samples used in this analysis, for MC16a, MC16d and MC16e conditions, respectively.

Sample
mc16_13TeV.345906.PowhegPythia8EvtGen_CT10_AZNLOCTEQ6L1_ggH125_EtacZll.merge.AOD.e6591_e5984_s3126_r9364_r9315
mc16_13TeV.450549.PowhegPythia8EvtGen_CT10_AZNLOCTEQ6L1_ggH125_JpsiZll.merge.AOD.e7242_e5984_s3126_r9364_r9315
mc16_13TeV.345907.PowhegPythia8EvtGen_CT10_AZNLOCTEQ6L1_ggH125_a0Zll_0p5GeVa0.merge.AOD.e6591_e5984_s3126_r9364_r9315
mc16_13TeV.450550.PowhegPythia8EvtGen_CT10_AZNLOCTEQ6L1_ggH125_a0Zll_0p75GeVa0.merge.AOD.e7242_e5984_s3126_r9364_r9315
mc16_13TeV.450551.PowhegPythia8EvtGen_CT10_AZNLOCTEQ6L1_ggH125_a0Zll_1p0GeVa0.merge.AOD.e7242_e5984_s3126_r9364_r9315
mc16_13TeV.450552.PowhegPythia8EvtGen_CT10_AZNLOCTEQ6L1_ggH125_a0Zll_1p5GeVa0.merge.AOD.e7242_e5984_s3126_r9364_r9315
mc16_13TeV.450553.PowhegPythia8EvtGen_CT10_AZNLOCTEQ6L1_ggH125_a0Zll_2p0GeVa0.merge.AOD.e7242_e5984_s3126_r9364_r9315
mc16_13TeV.345908.PowhegPythia8EvtGen_CT10_AZNLOCTEQ6L1_ggH125_a0Zll_2p5GeVa0.merge.AOD.e6591_e5984_s3126_r9364_r9315
mc16_13TeV.450554.PowhegPythia8EvtGen_CT10_AZNLOCTEQ6L1_ggH125_a0Zll_3p0GeVa0.merge.AOD.e7242_e5984_s3126_r9364_r9315
mc16_13TeV.450555.PowhegPythia8EvtGen_CT10_AZNLOCTEQ6L1_ggH125_a0Zll_3p5GeVa0.merge.AOD.e7242_e5984_s3126_r9364_r9315
mc16_13TeV.450556.PowhegPythia8EvtGen_CT10_AZNLOCTEQ6L1_ggH125_a0Zll_4p0GeVa0.merge.AOD.e7242_e5984_s3126_r9364_r9315
mc16_13TeV.345909.PowhegPythia8EvtGen_CT10_AZNLOCTEQ6L1_ggH125_a0Zll_8GeVa0.merge.AOD.e6591_e5984_s3126_r9364_r9315

Table 26: MC16a MC background samples used in this analysis. MC16a files correspond to 2015 and 2016 data conditions.

Sample
mc16_13TeV.345906.PowhegPythia8EvtGen_CT10_AZNLOCTEQ6L1_ggH125_EtacZll.merge.AOD.e6591_e5984_s3126_r10201_r10210
mc16_13TeV.450549.PowhegPythia8EvtGen_CT10_AZNLOCTEQ6L1_ggH125_JpsiZll.merge.AOD.e7242_e5984_s3126_r10201_r10210
mc16_13TeV.345907.PowhegPythia8EvtGen_CT10_AZNLOCTEQ6L1_ggH125_a0Zll_0p5GeVa0.merge.AOD.e6591_e5984_s3126_r10201_r10210
mc16_13TeV.450550.PowhegPythia8EvtGen_CT10_AZNLOCTEQ6L1_ggH125_a0Zll_0p75GeVa0.merge.AOD.e7242_e5984_s3126_r10201_r10210
mc16_13TeV.450551.PowhegPythia8EvtGen_CT10_AZNLOCTEQ6L1_ggH125_a0Zll_1p0GeVa0.merge.AOD.e7242_e5984_s3126_r10201_r10210
mc16_13TeV.450552.PowhegPythia8EvtGen_CT10_AZNLOCTEQ6L1_ggH125_a0Zll_1p5GeVa0.merge.AOD.e7242_e5984_s3126_r10201_r10210
mc16_13TeV.450553.PowhegPythia8EvtGen_CT10_AZNLOCTEQ6L1_ggH125_a0Zll_2p0GeVa0.merge.AOD.e7242_e5984_s3126_r10201_r10210
mc16_13TeV.345908.PowhegPythia8EvtGen_CT10_AZNLOCTEQ6L1_ggH125_a0Zll_2p5GeVa0.merge.AOD.e6591_e5984_s3126_r10201_r10210
mc16_13TeV.450554.PowhegPythia8EvtGen_CT10_AZNLOCTEQ6L1_ggH125_a0Zll_3p0GeVa0.merge.AOD.e7242_e5984_s3126_r10201_r10210
mc16_13TeV.450555.PowhegPythia8EvtGen_CT10_AZNLOCTEQ6L1_ggH125_a0Zll_3p5GeVa0.merge.AOD.e7242_e5984_s3126_r10201_r10210
mc16_13TeV.450556.PowhegPythia8EvtGen_CT10_AZNLOCTEQ6L1_ggH125_a0Zll_4p0GeVa0.merge.AOD.e7242_e5984_s3126_r10201_r10210
mc16_13TeV.345909.PowhegPythia8EvtGen_CT10_AZNLOCTEQ6L1_ggH125_a0Zll_8GeVa0.merge.AOD.e6591_e5984_s3126_r10201_r10210

Table 27: MC16d MC background samples used in this analysis. MC16d files correspond to 2017 data conditions.

Sample
mc16_13TeV.345906.PowhegPythia8EvtGen_CT10_AZNLOCTEQ6L1_ggH125_EtacZll.merge.AOD.e6591_e5984_s3126_r10724_r10726
mc16_13TeV.450549.PowhegPythia8EvtGen_CT10_AZNLOCTEQ6L1_ggH125_JpsiZll.merge.AOD.e7242_e5984_s3126_r10724_r10726
mc16_13TeV.345907.PowhegPythia8EvtGen_CT10_AZNLOCTEQ6L1_ggH125_a0Zll_0p5GeVa0.merge.AOD.e6591_e5984_s3126_r10724_r10726
mc16_13TeV.450550.PowhegPythia8EvtGen_CT10_AZNLOCTEQ6L1_ggH125_a0Zll_0p75GeVa0.merge.AOD.e7242_e5984_s3126_r10724_r10726
mc16_13TeV.450551.PowhegPythia8EvtGen_CT10_AZNLOCTEQ6L1_ggH125_a0Zll_1p0GeVa0.merge.AOD.e7242_e5984_s3126_r10724_r10726
mc16_13TeV.450552.PowhegPythia8EvtGen_CT10_AZNLOCTEQ6L1_ggH125_a0Zll_1p5GeVa0.merge.AOD.e7242_e5984_s3126_r10724_r10726
mc16_13TeV.450553.PowhegPythia8EvtGen_CT10_AZNLOCTEQ6L1_ggH125_a0Zll_2p0GeVa0.merge.AOD.e7242_e5984_s3126_r10724_r10726
mc16_13TeV.345908.PowhegPythia8EvtGen_CT10_AZNLOCTEQ6L1_ggH125_a0Zll_2p5GeVa0.merge.AOD.e6591_e5984_s3126_r10724_r10726
mc16_13TeV.450554.PowhegPythia8EvtGen_CT10_AZNLOCTEQ6L1_ggH125_a0Zll_3p0GeVa0.merge.AOD.e7242_e5984_s3126_r10724_r10726
mc16_13TeV.450555.PowhegPythia8EvtGen_CT10_AZNLOCTEQ6L1_ggH125_a0Zll_3p5GeVa0.merge.AOD.e7242_e5984_s3126_r10724_r10726
mc16_13TeV.450556.PowhegPythia8EvtGen_CT10_AZNLOCTEQ6L1_ggH125_a0Zll_4p0GeVa0.merge.AOD.e7242_e5984_s3126_r10724_r10726
mc16_13TeV.345909.PowhegPythia8EvtGen_CT10_AZNLOCTEQ6L1_ggH125_a0Zll_8GeVa0.merge.AOD.e6591_e5984_s3126_r10724_r10726

Table 28: MC16e MC background samples used in this analysis. MC16e files correspond to 2018 data conditions.

C Monte-Carlo Simulation Background Samples

Tables 29, 30 and 31 list the nominal background MC samples used in this analysis, for MC16a, MC16d and MC16e conditions, respectively. Tables 32, 33 and 34 list the alternative Z + jets background MC samples used, for MC16a, MC16d and MC16e conditions, respectively.

Sample
$t\bar{t}$
mc16_13TeV.410472.PhPy8EG_A14_ttbar_hdamp258p75_dil.deriv.DAOD_FTAG2.e6348_s3126_r9364_p3703
Diboson
mc16_13TeV.363356.Sherpa_221_NNPDF30NNLO_ZqqZll.deriv.DAOD_FTAG2.e5525_s3126_r9364_p3703
mc16_13TeV.363358.Sherpa_221_NNPDF30NNLO_WqqZll.deriv.DAOD_FTAG2.e5525_s3126_r9364_p3703
mc16_13TeV.364302.Sherpa_222_NNPDF30NNLO_ggZllZqq.deriv.DAOD_FTAG2.e6273_s3126_r9364_p3703
Z + jets
mc16_13TeV.364100.Sherpa_221_NNPDF30NNLO_Zmumu_MAXHTPTV0_70_CVetoBVeto.deriv.DAOD_FTAG2.e5271_s3126_r9364_p3703
mc16_13TeV.364101.Sherpa_221_NNPDF30NNLO_Zmumu_MAXHTPTV0_70_CFilterBVeto.deriv.DAOD_FTAG2.e5271_s3126_r9364_p3703
mc16_13TeV.364102.Sherpa_221_NNPDF30NNLO_Zmumu_MAXHTPTV0_70_BFilter.deriv.DAOD_FTAG2.e5271_s3126_r9364_p3703
mc16_13TeV.364103.Sherpa_221_NNPDF30NNLO_Zmumu_MAXHTPTV70_140_CVetoBVeto.deriv.DAOD_FTAG2.e5271_s3126_r9364_p3703
mc16_13TeV.364104.Sherpa_221_NNPDF30NNLO_Zmumu_MAXHTPTV70_140_CFilterBVeto.deriv.DAOD_FTAG2.e5271_s3126_r9364_p3703
mc16_13TeV.364105.Sherpa_221_NNPDF30NNLO_Zmumu_MAXHTPTV70_140_BFilter.deriv.DAOD_FTAG2.e5271_s3126_r9364_p3703
mc16_13TeV.364106.Sherpa_221_NNPDF30NNLO_Zmumu_MAXHTPTV140_280_CVetoBVeto.deriv.DAOD_FTAG2.e5271_s3126_r9364_p3703
mc16_13TeV.364107.Sherpa_221_NNPDF30NNLO_Zmumu_MAXHTPTV140_280_CFilterBVeto.deriv.DAOD_FTAG2.e5271_s3126_r9364_p3703
mc16_13TeV.364108.Sherpa_221_NNPDF30NNLO_Zmumu_MAXHTPTV140_280_BFilter.deriv.DAOD_FTAG2.e5271_s3126_r9364_p3703
mc16_13TeV.364109.Sherpa_221_NNPDF30NNLO_Zmumu_MAXHTPTV280_500_CVetoBVeto.deriv.DAOD_FTAG2.e5271_s3126_r9364_p3703
mc16_13TeV.364110.Sherpa_221_NNPDF30NNLO_Zmumu_MAXHTPTV280_500_CFilterBVeto.deriv.DAOD_FTAG2.e5271_s3126_r9364_p3703
mc16_13TeV.364111.Sherpa_221_NNPDF30NNLO_Zmumu_MAXHTPTV280_500_BFilter.deriv.DAOD_FTAG2.e5271_s3126_r9364_p3703
mc16_13TeV.364112.Sherpa_221_NNPDF30NNLO_Zmumu_MAXHTPTV500_1000.deriv.DAOD_FTAG2.e5271_s3126_r9364_p3703
mc16_13TeV.364113.Sherpa_221_NNPDF30NNLO_Zmumu_MAXHTPTV1000_E_CMS.deriv.DAOD_FTAG2.e5271_s3126_r9364_p3703
mc16_13TeV.364114.Sherpa_221_NNPDF30NNLO_Zee_MAXHTPTV0_70_CVetoBVeto.deriv.DAOD_FTAG2.e5299_s3126_r9364_p3703
mc16_13TeV.364115.Sherpa_221_NNPDF30NNLO_Zee_MAXHTPTV0_70_CFilterBVeto.deriv.DAOD_FTAG2.e5299_s3126_r9364_p3703
mc16_13TeV.364116.Sherpa_221_NNPDF30NNLO_Zee_MAXHTPTV0_70_BFilter.deriv.DAOD_FTAG2.e5299_s3126_r9364_p3703
mc16_13TeV.364117.Sherpa_221_NNPDF30NNLO_Zee_MAXHTPTV70_140_CVetoBVeto.deriv.DAOD_FTAG2.e5299_s3126_r9364_p3703
mc16_13TeV.364118.Sherpa_221_NNPDF30NNLO_Zee_MAXHTPTV70_140_CFilterBVeto.deriv.DAOD_FTAG2.e5299_s3126_r9364_p3703
mc16_13TeV.364119.Sherpa_221_NNPDF30NNLO_Zee_MAXHTPTV70_140_BFilter.deriv.DAOD_FTAG2.e5299_s3126_r9364_p3703
mc16_13TeV.364120.Sherpa_221_NNPDF30NNLO_Zee_MAXHTPTV140_280_CVetoBVeto.deriv.DAOD_FTAG2.e5299_s3126_r9364_p3703
mc16_13TeV.364121.Sherpa_221_NNPDF30NNLO_Zee_MAXHTPTV140_280_CFilterBVeto.deriv.DAOD_FTAG2.e5299_s3126_r9364_p3703
mc16_13TeV.364122.Sherpa_221_NNPDF30NNLO_Zee_MAXHTPTV140_280_BFilter.deriv.DAOD_FTAG2.e5299_s3126_r9364_p3703
mc16_13TeV.364123.Sherpa_221_NNPDF30NNLO_Zee_MAXHTPTV280_500_CVetoBVeto.deriv.DAOD_FTAG2.e5299_s3126_r9364_p3703
mc16_13TeV.364124.Sherpa_221_NNPDF30NNLO_Zee_MAXHTPTV280_500_CFilterBVeto.deriv.DAOD_FTAG2.e5299_s3126_r9364_p3703
mc16_13TeV.364125.Sherpa_221_NNPDF30NNLO_Zee_MAXHTPTV280_500_BFilter.deriv.DAOD_FTAG2.e5299_s3126_r9364_p3703
mc16_13TeV.364126.Sherpa_221_NNPDF30NNLO_Zee_MAXHTPTV500_1000.deriv.DAOD_FTAG2.e5299_s3126_r9364_p3703
mc16_13TeV.364127.Sherpa_221_NNPDF30NNLO_Zee_MAXHTPTV1000_E_CMS.deriv.DAOD_FTAG2.e5299_s3126_r9364_p3703
mc16_13TeV.364128.Sherpa_221_NNPDF30NNLO_Ztautau_MAXHTPTV0_70_CVetoBVeto.deriv.DAOD_FTAG2.e5307_s3126_r9364_p3703
mc16_13TeV.364129.Sherpa_221_NNPDF30NNLO_Ztautau_MAXHTPTV0_70_CFilterBVeto.deriv.DAOD_FTAG2.e5307_s3126_r9364_p3703
mc16_13TeV.364130.Sherpa_221_NNPDF30NNLO_Ztautau_MAXHTPTV0_70_BFilter.deriv.DAOD_FTAG2.e5307_s3126_r9364_p3703
mc16_13TeV.364131.Sherpa_221_NNPDF30NNLO_Ztautau_MAXHTPTV70_140_CVetoBVeto.deriv.DAOD_FTAG2.e5307_s3126_r9364_p3703
mc16_13TeV.364132.Sherpa_221_NNPDF30NNLO_Ztautau_MAXHTPTV70_140_CFilterBVeto.deriv.DAOD_FTAG2.e5307_s3126_r9364_p3703
mc16_13TeV.364133.Sherpa_221_NNPDF30NNLO_Ztautau_MAXHTPTV70_140_BFilter.deriv.DAOD_FTAG2.e5307_s3126_r9364_p3703
mc16_13TeV.364134.Sherpa_221_NNPDF30NNLO_Ztautau_MAXHTPTV140_280_CVetoBVeto.deriv.DAOD_FTAG2.e5307_s3126_r9364_p3703
mc16_13TeV.364135.Sherpa_221_NNPDF30NNLO_Ztautau_MAXHTPTV140_280_CFilterBVeto.deriv.DAOD_FTAG2.e5307_s3126_r9364_p3703
mc16_13TeV.364136.Sherpa_221_NNPDF30NNLO_Ztautau_MAXHTPTV140_280_BFilter.deriv.DAOD_FTAG2.e5307_s3126_r9364_p3703
mc16_13TeV.364137.Sherpa_221_NNPDF30NNLO_Ztautau_MAXHTPTV280_500_CVetoBVeto.deriv.DAOD_FTAG2.e5307_s3126_r9364_p3703
mc16_13TeV.364138.Sherpa_221_NNPDF30NNLO_Ztautau_MAXHTPTV280_500_CFilterBVeto.deriv.DAOD_FTAG2.e5313_s3126_r9364_p3703
mc16_13TeV.364139.Sherpa_221_NNPDF30NNLO_Ztautau_MAXHTPTV280_500_BFilter.deriv.DAOD_FTAG2.e5313_s3126_r9364_p3703
mc16_13TeV.364140.Sherpa_221_NNPDF30NNLO_Ztautau_MAXHTPTV500_1000.deriv.DAOD_FTAG2.e5307_s3126_r9364_p3703
mc16_13TeV.364141.Sherpa_221_NNPDF30NNLO_Ztautau_MAXHTPTV1000_E_CMS.deriv.DAOD_FTAG2.e5307_s3126_r9364_p3703

Table 29: MC16a MC background samples used in this analysis. MC16a files correspond to 2015 and 2016 data conditions.

Sample
$t\bar{t}$
mc16_13TeV.410472.PhPy8EG_A14_ttbar_hdamp258p75_dil.deriv.DAOD_FTAG2.e6348_s3126_r10201_p3703
Diboson
mc16_13TeV.363356.Sherpa_221_NNPDF30NNLO_ZqqZll.deriv.DAOD_FTAG2.e5525_s3126_r10201_p3703
mc16_13TeV.363358.Sherpa_221_NNPDF30NNLO_WqqZll.deriv.DAOD_FTAG2.e5525_s3126_r10201_p3703
mc16_13TeV.364302.Sherpa_222_NNPDF30NNLO_ggZllZqq.deriv.DAOD_FTAG2.e6273_s3126_r10201_p3703
Z + jets
mc16_13TeV.364100.Sherpa_221_NNPDF30NNLO_Zmumu_MAXHTPTV0_70_CVetoBVeto.deriv.DAOD_FTAG2.e5271_s3126_r10201_p3703
mc16_13TeV.364101.Sherpa_221_NNPDF30NNLO_Zmumu_MAXHTPTV0_70_CFilterBVeto.deriv.DAOD_FTAG2.e5271_s3126_r10201_p3703
mc16_13TeV.364102.Sherpa_221_NNPDF30NNLO_Zmumu_MAXHTPTV0_70_BFilter.deriv.DAOD_FTAG2.e5271_s3126_r10201_p3703
mc16_13TeV.364103.Sherpa_221_NNPDF30NNLO_Zmumu_MAXHTPTV70_140_CVetoBVeto.deriv.DAOD_FTAG2.e5271_s3126_r10201_p3703
mc16_13TeV.364104.Sherpa_221_NNPDF30NNLO_Zmumu_MAXHTPTV70_140_CFilterBVeto.deriv.DAOD_FTAG2.e5271_s3126_r10201_p3703
mc16_13TeV.364105.Sherpa_221_NNPDF30NNLO_Zmumu_MAXHTPTV70_140_BFilter.deriv.DAOD_FTAG2.e5271_s3126_r10201_p3703
mc16_13TeV.364106.Sherpa_221_NNPDF30NNLO_Zmumu_MAXHTPTV140_280_CVetoBVeto.deriv.DAOD_FTAG2.e5271_s3126_r10201_p3703
mc16_13TeV.364107.Sherpa_221_NNPDF30NNLO_Zmumu_MAXHTPTV140_280_CFilterBVeto.deriv.DAOD_FTAG2.e5271_s3126_r10201_p3703
mc16_13TeV.364108.Sherpa_221_NNPDF30NNLO_Zmumu_MAXHTPTV140_280_BFilter.deriv.DAOD_FTAG2.e5271_s3126_r10201_p3703
mc16_13TeV.364109.Sherpa_221_NNPDF30NNLO_Zmumu_MAXHTPTV280_500_CVetoBVeto.deriv.DAOD_FTAG2.e5271_s3126_r10201_p3703
mc16_13TeV.364110.Sherpa_221_NNPDF30NNLO_Zmumu_MAXHTPTV280_500_CFilterBVeto.deriv.DAOD_FTAG2.e5271_s3126_r10201_p3703
mc16_13TeV.364111.Sherpa_221_NNPDF30NNLO_Zmumu_MAXHTPTV280_500_BFilter.deriv.DAOD_FTAG2.e5271_s3126_r10201_p3703
mc16_13TeV.364112.Sherpa_221_NNPDF30NNLO_Zmumu_MAXHTPTV500_1000.deriv.DAOD_FTAG2.e5271_s3126_r10201_p3703
mc16_13TeV.364113.Sherpa_221_NNPDF30NNLO_Zmumu_MAXHTPTV1000_E_CMS.deriv.DAOD_FTAG2.e5271_s3126_r10201_p3703
mc16_13TeV.364114.Sherpa_221_NNPDF30NNLO_Zee_MAXHTPTV0_70_CVetoBVeto.deriv.DAOD_FTAG2.e5299_s3126_r10201_p3703
mc16_13TeV.364115.Sherpa_221_NNPDF30NNLO_Zee_MAXHTPTV0_70_CFilterBVeto.deriv.DAOD_FTAG2.e5299_s3126_r10201_p3703
mc16_13TeV.364116.Sherpa_221_NNPDF30NNLO_Zee_MAXHTPTV0_70_BFilter.deriv.DAOD_FTAG2.e5299_s3126_r10201_p3703
mc16_13TeV.364117.Sherpa_221_NNPDF30NNLO_Zee_MAXHTPTV70_140_CVetoBVeto.deriv.DAOD_FTAG2.e5299_s3126_r10201_p3703
mc16_13TeV.364118.Sherpa_221_NNPDF30NNLO_Zee_MAXHTPTV70_140_CFilterBVeto.deriv.DAOD_FTAG2.e5299_s3126_r10201_p3703
mc16_13TeV.364119.Sherpa_221_NNPDF30NNLO_Zee_MAXHTPTV70_140_BFilter.deriv.DAOD_FTAG2.e5299_s3126_r10201_p3703
mc16_13TeV.364120.Sherpa_221_NNPDF30NNLO_Zee_MAXHTPTV140_280_CVetoBVeto.deriv.DAOD_FTAG2.e5299_s3126_r10201_p3703
mc16_13TeV.364121.Sherpa_221_NNPDF30NNLO_Zee_MAXHTPTV140_280_CFilterBVeto.deriv.DAOD_FTAG2.e5299_s3126_r10201_p3703
mc16_13TeV.364122.Sherpa_221_NNPDF30NNLO_Zee_MAXHTPTV140_280_BFilter.deriv.DAOD_FTAG2.e5299_s3126_r10201_p3703
mc16_13TeV.364123.Sherpa_221_NNPDF30NNLO_Zee_MAXHTPTV280_500_CVetoBVeto.deriv.DAOD_FTAG2.e5299_s3126_r10201_p3703
mc16_13TeV.364124.Sherpa_221_NNPDF30NNLO_Zee_MAXHTPTV280_500_CFilterBVeto.deriv.DAOD_FTAG2.e5299_s3126_r10201_p3703
mc16_13TeV.364125.Sherpa_221_NNPDF30NNLO_Zee_MAXHTPTV280_500_BFilter.deriv.DAOD_FTAG2.e5299_s3126_r10201_p3703
mc16_13TeV.364126.Sherpa_221_NNPDF30NNLO_Zee_MAXHTPTV500_1000.deriv.DAOD_FTAG2.e5299_s3126_r10201_p3703
mc16_13TeV.364127.Sherpa_221_NNPDF30NNLO_Zee_MAXHTPTV1000_E_CMS.deriv.DAOD_FTAG2.e5299_s3126_r10201_p3703
mc16_13TeV.364128.Sherpa_221_NNPDF30NNLO_Ztautau_MAXHTPTV0_70_CVetoBVeto.deriv.DAOD_FTAG2.e5307_s3126_r10201_p3703
mc16_13TeV.364129.Sherpa_221_NNPDF30NNLO_Ztautau_MAXHTPTV0_70_CFilterBVeto.deriv.DAOD_FTAG2.e5307_s3126_r10201_p3703
mc16_13TeV.364130.Sherpa_221_NNPDF30NNLO_Ztautau_MAXHTPTV0_70_BFilter.deriv.DAOD_FTAG2.e5307_s3126_r10201_p3703
mc16_13TeV.364131.Sherpa_221_NNPDF30NNLO_Ztautau_MAXHTPTV70_140_CVetoBVeto.deriv.DAOD_FTAG2.e5307_s3126_r10201_p3703
mc16_13TeV.364132.Sherpa_221_NNPDF30NNLO_Ztautau_MAXHTPTV70_140_CFilterBVeto.deriv.DAOD_FTAG2.e5307_s3126_r10201_p3703
mc16_13TeV.364133.Sherpa_221_NNPDF30NNLO_Ztautau_MAXHTPTV70_140_BFilter.deriv.DAOD_FTAG2.e5307_s3126_r10201_p3703
mc16_13TeV.364134.Sherpa_221_NNPDF30NNLO_Ztautau_MAXHTPTV140_280_CVetoBVeto.deriv.DAOD_FTAG2.e5307_s3126_r10201_p3703
mc16_13TeV.364135.Sherpa_221_NNPDF30NNLO_Ztautau_MAXHTPTV140_280_CFilterBVeto.deriv.DAOD_FTAG2.e5307_s3126_r10201_p3703
mc16_13TeV.364136.Sherpa_221_NNPDF30NNLO_Ztautau_MAXHTPTV140_280_BFilter.deriv.DAOD_FTAG2.e5307_s3126_r10201_p3703
mc16_13TeV.364137.Sherpa_221_NNPDF30NNLO_Ztautau_MAXHTPTV280_500_CVetoBVeto.deriv.DAOD_FTAG2.e5307_s3126_r10201_p3703
mc16_13TeV.364138.Sherpa_221_NNPDF30NNLO_Ztautau_MAXHTPTV280_500_CFilterBVeto.deriv.DAOD_FTAG2.e5313_s3126_r10201_p3703
mc16_13TeV.364139.Sherpa_221_NNPDF30NNLO_Ztautau_MAXHTPTV280_500_BFilter.deriv.DAOD_FTAG2.e5313_s3126_r10201_p3703
mc16_13TeV.364140.Sherpa_221_NNPDF30NNLO_Ztautau_MAXHTPTV500_1000.deriv.DAOD_FTAG2.e5307_s3126_r10201_p3703
mc16_13TeV.364141.Sherpa_221_NNPDF30NNLO_Ztautau_MAXHTPTV1000_E_CMS.deriv.DAOD_FTAG2.e5307_s3126_r10201_p3703

Table 30: MC16d MC background samples used in this analysis. MC16a files correspond to 2017 data conditions.

Sample
$t\bar{t}$
mc16_13TeV.410472.PhPy8EG_A14_ttbar_hdamp258p75_dil.deriv.DAOD_FTAG2.e6348_s3126_r10724_p3703
Diboson
mc16_13TeV.363356.Sherpa_221_NNPDF30NNLO_ZqqZll.deriv.DAOD_FTAG2.e5525_s3126_r10724_p3703
mc16_13TeV.363358.Sherpa_221_NNPDF30NNLO_WqqZll.deriv.DAOD_FTAG2.e5525_s3126_r10724_p3703
mc16_13TeV.364302.Sherpa_222_NNPDF30NNLO_ggZllZqq.deriv.DAOD_FTAG2.e6273_s3126_r10724_p3703
Z + jets
mc16_13TeV.364100.Sherpa_221_NNPDF30NNLO_Zmumu_MAXHTPTV0_70_CVetoBVeto.deriv.DAOD_FTAG2.e5271_s3126_r10724_p3703
mc16_13TeV.364101.Sherpa_221_NNPDF30NNLO_Zmumu_MAXHTPTV0_70_CFilterBVeto.deriv.DAOD_FTAG2.e5271_s3126_r10724_p3703
mc16_13TeV.364102.Sherpa_221_NNPDF30NNLO_Zmumu_MAXHTPTV0_70_BFilter.deriv.DAOD_FTAG2.e5271_s3126_r10724_p3703
mc16_13TeV.364103.Sherpa_221_NNPDF30NNLO_Zmumu_MAXHTPTV70_140_CVetoBVeto.deriv.DAOD_FTAG2.e5271_s3126_r10724_p3703
mc16_13TeV.364104.Sherpa_221_NNPDF30NNLO_Zmumu_MAXHTPTV70_140_CFilterBVeto.deriv.DAOD_FTAG2.e5271_s3126_r10724_p3703
mc16_13TeV.364105.Sherpa_221_NNPDF30NNLO_Zmumu_MAXHTPTV70_140_BFilter.deriv.DAOD_FTAG2.e5271_s3126_r10724_p3703
mc16_13TeV.364106.Sherpa_221_NNPDF30NNLO_Zmumu_MAXHTPTV140_280_CVetoBVeto.deriv.DAOD_FTAG2.e5271_s3126_r10724_p3703
mc16_13TeV.364107.Sherpa_221_NNPDF30NNLO_Zmumu_MAXHTPTV140_280_CFilterBVeto.deriv.DAOD_FTAG2.e5271_s3126_r10724_p3703
mc16_13TeV.364108.Sherpa_221_NNPDF30NNLO_Zmumu_MAXHTPTV140_280_BFilter.deriv.DAOD_FTAG2.e5271_s3126_r10724_p3703
mc16_13TeV.364109.Sherpa_221_NNPDF30NNLO_Zmumu_MAXHTPTV280_500_CVetoBVeto.deriv.DAOD_FTAG2.e5271_s3126_r10724_p3703
mc16_13TeV.364110.Sherpa_221_NNPDF30NNLO_Zmumu_MAXHTPTV280_500_CFilterBVeto.deriv.DAOD_FTAG2.e5271_s3126_r10724_p3703
mc16_13TeV.364111.Sherpa_221_NNPDF30NNLO_Zmumu_MAXHTPTV280_500_BFilter.deriv.DAOD_FTAG2.e5271_s3126_r10724_p3703
mc16_13TeV.364112.Sherpa_221_NNPDF30NNLO_Zmumu_MAXHTPTV500_1000.deriv.DAOD_FTAG2.e5271_s3126_r10724_p3703
mc16_13TeV.364113.Sherpa_221_NNPDF30NNLO_Zmumu_MAXHTPTV1000_E_CMS.deriv.DAOD_FTAG2.e5271_s3126_r10724_p3703
mc16_13TeV.364114.Sherpa_221_NNPDF30NNLO_Zee_MAXHTPTV0_70_CVetoBVeto.deriv.DAOD_FTAG2.e5299_s3126_r10724_p3703
mc16_13TeV.364115.Sherpa_221_NNPDF30NNLO_Zee_MAXHTPTV0_70_CFilterBVeto.deriv.DAOD_FTAG2.e5299_s3126_r10724_p3703
mc16_13TeV.364116.Sherpa_221_NNPDF30NNLO_Zee_MAXHTPTV0_70_BFilter.deriv.DAOD_FTAG2.e5299_s3126_r10724_p3703
mc16_13TeV.364117.Sherpa_221_NNPDF30NNLO_Zee_MAXHTPTV70_140_CVetoBVeto.deriv.DAOD_FTAG2.e5299_s3126_r10724_p3703
mc16_13TeV.364118.Sherpa_221_NNPDF30NNLO_Zee_MAXHTPTV70_140_CFilterBVeto.deriv.DAOD_FTAG2.e5299_s3126_r10724_p3703
mc16_13TeV.364119.Sherpa_221_NNPDF30NNLO_Zee_MAXHTPTV70_140_BFilter.deriv.DAOD_FTAG2.e5299_s3126_r10724_p3703
mc16_13TeV.364120.Sherpa_221_NNPDF30NNLO_Zee_MAXHTPTV140_280_CVetoBVeto.deriv.DAOD_FTAG2.e5299_s3126_r10724_p3703
mc16_13TeV.364121.Sherpa_221_NNPDF30NNLO_Zee_MAXHTPTV140_280_CFilterBVeto.deriv.DAOD_FTAG2.e5299_s3126_r10724_p3703
mc16_13TeV.364122.Sherpa_221_NNPDF30NNLO_Zee_MAXHTPTV140_280_BFilter.deriv.DAOD_FTAG2.e5299_s3126_r10724_p3703
mc16_13TeV.364123.Sherpa_221_NNPDF30NNLO_Zee_MAXHTPTV280_500_CVetoBVeto.deriv.DAOD_FTAG2.e5299_s3126_r10724_p3703
mc16_13TeV.364124.Sherpa_221_NNPDF30NNLO_Zee_MAXHTPTV280_500_CFilterBVeto.deriv.DAOD_FTAG2.e5299_s3126_r10724_p3703
mc16_13TeV.364125.Sherpa_221_NNPDF30NNLO_Zee_MAXHTPTV280_500_BFilter.deriv.DAOD_FTAG2.e5299_s3126_r10724_p3703
mc16_13TeV.364126.Sherpa_221_NNPDF30NNLO_Zee_MAXHTPTV500_1000.deriv.DAOD_FTAG2.e5299_s3126_r10724_p3703
mc16_13TeV.364127.Sherpa_221_NNPDF30NNLO_Zee_MAXHTPTV1000_E_CMS.deriv.DAOD_FTAG2.e5299_s3126_r10724_p3703
mc16_13TeV.364128.Sherpa_221_NNPDF30NNLO_Ztautau_MAXHTPTV0_70_CVetoBVeto.deriv.DAOD_FTAG2.e5307_s3126_r10724_p3703
mc16_13TeV.364129.Sherpa_221_NNPDF30NNLO_Ztautau_MAXHTPTV0_70_CFilterBVeto.deriv.DAOD_FTAG2.e5307_s3126_r10724_p3703
mc16_13TeV.364130.Sherpa_221_NNPDF30NNLO_Ztautau_MAXHTPTV0_70_BFilter.deriv.DAOD_FTAG2.e5307_s3126_r10724_p3703
mc16_13TeV.364131.Sherpa_221_NNPDF30NNLO_Ztautau_MAXHTPTV70_140_CVetoBVeto.deriv.DAOD_FTAG2.e5307_s3126_r10724_p3703
mc16_13TeV.364132.Sherpa_221_NNPDF30NNLO_Ztautau_MAXHTPTV70_140_CFilterBVeto.deriv.DAOD_FTAG2.e5307_s3126_r10724_p3703
mc16_13TeV.364133.Sherpa_221_NNPDF30NNLO_Ztautau_MAXHTPTV70_140_BFilter.deriv.DAOD_FTAG2.e5307_s3126_r10724_p3703
mc16_13TeV.364134.Sherpa_221_NNPDF30NNLO_Ztautau_MAXHTPTV140_280_CVetoBVeto.deriv.DAOD_FTAG2.e5307_s3126_r10724_p3703
mc16_13TeV.364135.Sherpa_221_NNPDF30NNLO_Ztautau_MAXHTPTV140_280_CFilterBVeto.deriv.DAOD_FTAG2.e5307_s3126_r10724_p3703
mc16_13TeV.364136.Sherpa_221_NNPDF30NNLO_Ztautau_MAXHTPTV140_280_BFilter.deriv.DAOD_FTAG2.e5307_s3126_r10724_p3703
mc16_13TeV.364137.Sherpa_221_NNPDF30NNLO_Ztautau_MAXHTPTV280_500_CVetoBVeto.deriv.DAOD_FTAG2.e5307_s3126_r10724_p3703
mc16_13TeV.364138.Sherpa_221_NNPDF30NNLO_Ztautau_MAXHTPTV280_500_CFilterBVeto.deriv.DAOD_FTAG2.e5313_s3126_r10724_p3703
mc16_13TeV.364139.Sherpa_221_NNPDF30NNLO_Ztautau_MAXHTPTV280_500_BFilter.deriv.DAOD_FTAG2.e5313_s3126_r10724_p3703
mc16_13TeV.364140.Sherpa_221_NNPDF30NNLO_Ztautau_MAXHTPTV500_1000.deriv.DAOD_FTAG2.e5307_s3126_r10724_p3703
mc16_13TeV.364141.Sherpa_221_NNPDF30NNLO_Ztautau_MAXHTPTV1000_E_CMS.deriv.DAOD_FTAG2.e5307_s3126_r10724_p3703

Table 31: MC16e MC background samples used in this analysis. MC16a files correspond to 2017 data conditions.

Sample
Z + jets (MADGRAPH)
mc16_13TeV.363123.MGPy8EG_N30NLO_Zmumu_Ht0_70_CVetoBVeto.deriv.DAOD_FTAG2.e4649_s3126_r9364_p3703
mc16_13TeV.363124.MGPy8EG_N30NLO_Zmumu_Ht0_70_CFilterBVeto.deriv.DAOD_FTAG2.e4649_s3126_r9364_p3703
mc16_13TeV.363125.MGPy8EG_N30NLO_Zmumu_Ht0_70_BFilter.deriv.DAOD_FTAG2.e4649_s3126_r9364_p3703
mc16_13TeV.363126.MGPy8EG_N30NLO_Zmumu_Ht70_140_CVetoBVeto.deriv.DAOD_FTAG2.e4649_s3126_r9364_p3703
mc16_13TeV.363127.MGPy8EG_N30NLO_Zmumu_Ht70_140_CFilterBVeto.deriv.DAOD_FTAG2.e4649_s3126_r9364_p3703
mc16_13TeV.363128.MGPy8EG_N30NLO_Zmumu_Ht70_140_BFilter.deriv.DAOD_FTAG2.e4649_s3126_r9364_p3703
mc16_13TeV.363129.MGPy8EG_N30NLO_Zmumu_Ht140_280_CVetoBVeto.deriv.DAOD_FTAG2.e4649_s3126_r9364_p3703
mc16_13TeV.363130.MGPy8EG_N30NLO_Zmumu_Ht140_280_CFilterBVeto.deriv.DAOD_FTAG2.e4649_s3126_r9364_p3703
mc16_13TeV.363131.MGPy8EG_N30NLO_Zmumu_Ht140_280_BFilter.deriv.DAOD_FTAG2.e4649_s3126_r9364_p3703
mc16_13TeV.363132.MGPy8EG_N30NLO_Zmumu_Ht280_500_CVetoBVeto.deriv.DAOD_FTAG2.e4649_s3126_r9364_p3703
mc16_13TeV.363133.MGPy8EG_N30NLO_Zmumu_Ht280_500_CFilterBVeto.deriv.DAOD_FTAG2.e4649_s3126_r9364_p3703
mc16_13TeV.363134.MGPy8EG_N30NLO_Zmumu_Ht280_500_BFilter.deriv.DAOD_FTAG2.e4649_s3126_r9364_p3703
mc16_13TeV.363135.MGPy8EG_N30NLO_Zmumu_Ht500_700_CVetoBVeto.deriv.DAOD_FTAG2.e4649_s3126_r9364_p3703
mc16_13TeV.363136.MGPy8EG_N30NLO_Zmumu_Ht500_700_CFilterBVeto.deriv.DAOD_FTAG2.e4649_s3126_r9364_p3703
mc16_13TeV.363137.MGPy8EG_N30NLO_Zmumu_Ht500_700_BFilter.deriv.DAOD_FTAG2.e4649_s3126_r9364_p3703
mc16_13TeV.363138.MGPy8EG_N30NLO_Zmumu_Ht700_1000_CVetoBVeto.deriv.DAOD_FTAG2.e4649_s3126_r9364_p3703
mc16_13TeV.363139.MGPy8EG_N30NLO_Zmumu_Ht700_1000_CFilterBVeto.deriv.DAOD_FTAG2.e4649_s3126_r9364_p3703
mc16_13TeV.363140.MGPy8EG_N30NLO_Zmumu_Ht700_1000_BFilter.deriv.DAOD_FTAG2.e4649_s3126_r9364_p3703
mc16_13TeV.363141.MGPy8EG_N30NLO_Zmumu_Ht1000_2000_CVetoBVeto.deriv.DAOD_FTAG2.e4649_s3126_r9364_p3703
mc16_13TeV.363142.MGPy8EG_N30NLO_Zmumu_Ht1000_2000_CFilterBVeto.deriv.DAOD_FTAG2.e4649_s3126_r9364_p3703
mc16_13TeV.363143.MGPy8EG_N30NLO_Zmumu_Ht1000_2000_BFilter.deriv.DAOD_FTAG2.e4649_s3126_r9364_p3703
mc16_13TeV.363144.MGPy8EG_N30NLO_Zmumu_Ht2000_E_CMS_CVetoBVeto.deriv.DAOD_FTAG2.e4649_s3126_r9364_p3703
mc16_13TeV.363145.MGPy8EG_N30NLO_Zmumu_Ht2000_E_CMS_CFilterBVeto.deriv.DAOD_FTAG2.e4649_s3126_r9364_p3703
mc16_13TeV.363146.MGPy8EG_N30NLO_Zmumu_Ht2000_E_CMS_BFilter.deriv.DAOD_FTAG2.e4649_s3126_r9364_p3703
mc16_13TeV.363147.MGPy8EG_N30NLO_Zee_Ht0_70_CVetoBVeto.deriv.DAOD_FTAG2.e4866_s3126_r9364_p3703
mc16_13TeV.363148.MGPy8EG_N30NLO_Zee_Ht0_70_CFilterBVeto.deriv.DAOD_FTAG2.e4866_s3126_r9364_p3703
mc16_13TeV.363149.MGPy8EG_N30NLO_Zee_Ht0_70_BFilter.deriv.DAOD_FTAG2.e4866_s3126_r9364_p3703
mc16_13TeV.363150.MGPy8EG_N30NLO_Zee_Ht70_140_CVetoBVeto.deriv.DAOD_FTAG2.e4866_s3126_r9364_p3703
mc16_13TeV.363151.MGPy8EG_N30NLO_Zee_Ht70_140_CFilterBVeto.deriv.DAOD_FTAG2.e4866_s3126_r9364_p3703
mc16_13TeV.363152.MGPy8EG_N30NLO_Zee_Ht70_140_BFilter.deriv.DAOD_FTAG2.e4866_s3126_r9364_p3703
mc16_13TeV.363153.MGPy8EG_N30NLO_Zee_Ht140_280_CVetoBVeto.deriv.DAOD_FTAG2.e4866_s3126_r9364_p3703
mc16_13TeV.363154.MGPy8EG_N30NLO_Zee_Ht140_280_CFilterBVeto.deriv.DAOD_FTAG2.e4866_s3126_r9364_p3703
mc16_13TeV.363155.MGPy8EG_N30NLO_Zee_Ht140_280_BFilter.deriv.DAOD_FTAG2.e4866_s3126_r9364_p3703
mc16_13TeV.363156.MGPy8EG_N30NLO_Zee_Ht280_500_CVetoBVeto.deriv.DAOD_FTAG2.e4866_s3126_r9364_p3703
mc16_13TeV.363157.MGPy8EG_N30NLO_Zee_Ht280_500_CFilterBVeto.deriv.DAOD_FTAG2.e4866_s3126_r9364_p3703
mc16_13TeV.363158.MGPy8EG_N30NLO_Zee_Ht280_500_BFilter.deriv.DAOD_FTAG2.e4866_s3126_r9364_p3703
mc16_13TeV.363159.MGPy8EG_N30NLO_Zee_Ht500_700_CVetoBVeto.deriv.DAOD_FTAG2.e4866_s3126_r9364_p3703
mc16_13TeV.363160.MGPy8EG_N30NLO_Zee_Ht500_700_CFilterBVeto.deriv.DAOD_FTAG2.e4866_s3126_r9364_p3703
mc16_13TeV.363161.MGPy8EG_N30NLO_Zee_Ht500_700_BFilter.deriv.DAOD_FTAG2.e4866_s3126_r9364_p3703
mc16_13TeV.363162.MGPy8EG_N30NLO_Zee_Ht700_1000_CVetoBVeto.deriv.DAOD_FTAG2.e4866_s3126_r9364_p3703
mc16_13TeV.363163.MGPy8EG_N30NLO_Zee_Ht700_1000_CFilterBVeto.deriv.DAOD_FTAG2.e4866_s3126_r9364_p3703
mc16_13TeV.363164.MGPy8EG_N30NLO_Zee_Ht700_1000_BFilter.deriv.DAOD_FTAG2.e4866_s3126_r9364_p3703
mc16_13TeV.363165.MGPy8EG_N30NLO_Zee_Ht1000_2000_CVetoBVeto.deriv.DAOD_FTAG2.e4866_s3126_r9364_p3703
mc16_13TeV.363166.MGPy8EG_N30NLO_Zee_Ht1000_2000_CFilterBVeto.deriv.DAOD_FTAG2.e4866_s3126_r9364_p3703
mc16_13TeV.363167.MGPy8EG_N30NLO_Zee_Ht1000_2000_BFilter.deriv.DAOD_FTAG2.e4866_s3126_r9364_p3703
mc16_13TeV.363168.MGPy8EG_N30NLO_Zee_Ht2000_E_CMS_CVetoBVeto.deriv.DAOD_FTAG2.e4866_s3126_r9364_p3703
mc16_13TeV.363169.MGPy8EG_N30NLO_Zee_Ht2000_E_CMS_CFilterBVeto.deriv.DAOD_FTAG2.e4866_s3126_r9364_p3703
mc16_13TeV.363170.MGPy8EG_N30NLO_Zee_Ht2000_E_CMS_BFilter.deriv.DAOD_FTAG2.e4866_s3126_r9364_p3703
mc16_13TeV.361510.MadGraphPythia8EvtGen_A14NNPDF23LO_Ztautau_Np0.deriv.DAOD_FTAG2.e3898_s3126_r9364_p3703
mc16_13TeV.361511.MadGraphPythia8EvtGen_A14NNPDF23LO_Ztautau_Np1.deriv.DAOD_FTAG2.e3898_s3126_r9364_p3703
mc16_13TeV.361512.MadGraphPythia8EvtGen_A14NNPDF23LO_Ztautau_Np2.deriv.DAOD_FTAG2.e3898_s3126_r9364_p3703
mc16_13TeV.361513.MadGraphPythia8EvtGen_A14NNPDF23LO_Ztautau_Np3.deriv.DAOD_FTAG2.e3898_s3126_r9364_p3703
mc16_13TeV.361514.MadGraphPythia8EvtGen_A14NNPDF23LO_Ztautau_Np4.deriv.DAOD_FTAG2.e3898_s3126_r9364_p3703

Table 32: MC16a MC background samples used in this analysis. MC16a files correspond to 2015 and 2016 data conditions.

Sample
Z + jets (MADGRAPH)
mc16_13TeV.363123.MGPy8EG_N30NLO_Zmumu_Ht0_70_CVetoBVeto.deriv.DAOD_FTAG2.e4649_s3126_r10201_p3703
mc16_13TeV.363124.MGPy8EG_N30NLO_Zmumu_Ht0_70_CFilterBVeto.deriv.DAOD_FTAG2.e4649_s3126_r10201_p3703
mc16_13TeV.363125.MGPy8EG_N30NLO_Zmumu_Ht0_70_BFilter.deriv.DAOD_FTAG2.e4649_s3126_r10201_p3703
mc16_13TeV.363126.MGPy8EG_N30NLO_Zmumu_Ht70_140_CVetoBVeto.deriv.DAOD_FTAG2.e4649_s3126_r10201_p3703
mc16_13TeV.363127.MGPy8EG_N30NLO_Zmumu_Ht70_140_CFilterBVeto.deriv.DAOD_FTAG2.e4649_s3126_r10201_p3703
mc16_13TeV.363128.MGPy8EG_N30NLO_Zmumu_Ht70_140_BFilter.deriv.DAOD_FTAG2.e4649_s3126_r10201_p3703
mc16_13TeV.363129.MGPy8EG_N30NLO_Zmumu_Ht140_280_CVetoBVeto.deriv.DAOD_FTAG2.e4649_s3126_r10201_p3703
mc16_13TeV.363130.MGPy8EG_N30NLO_Zmumu_Ht140_280_CFilterBVeto.deriv.DAOD_FTAG2.e4649_s3126_r10201_p3703
mc16_13TeV.363131.MGPy8EG_N30NLO_Zmumu_Ht140_280_BFilter.deriv.DAOD_FTAG2.e4649_s3126_r10201_p3703
mc16_13TeV.363132.MGPy8EG_N30NLO_Zmumu_Ht280_500_CVetoBVeto.deriv.DAOD_FTAG2.e4649_s3126_r10201_p3703
mc16_13TeV.363133.MGPy8EG_N30NLO_Zmumu_Ht280_500_CFilterBVeto.deriv.DAOD_FTAG2.e4649_s3126_r10201_p3703
mc16_13TeV.363134.MGPy8EG_N30NLO_Zmumu_Ht280_500_BFilter.deriv.DAOD_FTAG2.e4649_s3126_r10201_p3703
mc16_13TeV.363135.MGPy8EG_N30NLO_Zmumu_Ht500_700_CVetoBVeto.deriv.DAOD_FTAG2.e4649_s3126_r10201_p3703
mc16_13TeV.363136.MGPy8EG_N30NLO_Zmumu_Ht500_700_CFilterBVeto.deriv.DAOD_FTAG2.e4649_s3126_r10201_p3703
mc16_13TeV.363137.MGPy8EG_N30NLO_Zmumu_Ht500_700_BFilter.deriv.DAOD_FTAG2.e4649_s3126_r10201_p3703
mc16_13TeV.363138.MGPy8EG_N30NLO_Zmumu_Ht700_1000_CVetoBVeto.deriv.DAOD_FTAG2.e4649_s3126_r10201_p3703
mc16_13TeV.363139.MGPy8EG_N30NLO_Zmumu_Ht700_1000_CFilterBVeto.deriv.DAOD_FTAG2.e4649_s3126_r10201_p3703
mc16_13TeV.363140.MGPy8EG_N30NLO_Zmumu_Ht700_1000_BFilter.deriv.DAOD_FTAG2.e4649_s3126_r10201_p3703
mc16_13TeV.363141.MGPy8EG_N30NLO_Zmumu_Ht1000_2000_CVetoBVeto.deriv.DAOD_FTAG2.e4649_s3126_r10201_p3703
mc16_13TeV.363142.MGPy8EG_N30NLO_Zmumu_Ht1000_2000_CFilterBVeto.deriv.DAOD_FTAG2.e4649_s3126_r10201_p3703
mc16_13TeV.363143.MGPy8EG_N30NLO_Zmumu_Ht1000_2000_BFilter.deriv.DAOD_FTAG2.e4649_s3126_r10201_p3703
mc16_13TeV.363144.MGPy8EG_N30NLO_Zmumu_Ht2000_E_CMS_CVetoBVeto.deriv.DAOD_FTAG2.e4649_s3126_r10201_p3703
mc16_13TeV.363145.MGPy8EG_N30NLO_Zmumu_Ht2000_E_CMS_CFilterBVeto.deriv.DAOD_FTAG2.e4649_s3126_r10201_p3703
mc16_13TeV.363146.MGPy8EG_N30NLO_Zmumu_Ht2000_E_CMS_BFilter.deriv.DAOD_FTAG2.e4649_s3126_r10201_p3703
mc16_13TeV.363147.MGPy8EG_N30NLO_Zee_Ht0_70_CVetoBVeto.deriv.DAOD_FTAG2.e4866_s3126_r10201_p3703
mc16_13TeV.363148.MGPy8EG_N30NLO_Zee_Ht0_70_CFilterBVeto.deriv.DAOD_FTAG2.e4866_s3126_r10201_p3703
mc16_13TeV.363149.MGPy8EG_N30NLO_Zee_Ht0_70_BFilter.deriv.DAOD_FTAG2.e4866_s3126_r10201_p3703
mc16_13TeV.363150.MGPy8EG_N30NLO_Zee_Ht70_140_CVetoBVeto.deriv.DAOD_FTAG2.e4866_s3126_r10201_p3703
mc16_13TeV.363151.MGPy8EG_N30NLO_Zee_Ht70_140_CFilterBVeto.deriv.DAOD_FTAG2.e4866_s3126_r10201_p3703
mc16_13TeV.363152.MGPy8EG_N30NLO_Zee_Ht70_140_BFilter.deriv.DAOD_FTAG2.e4866_s3126_r10201_p3703
mc16_13TeV.363153.MGPy8EG_N30NLO_Zee_Ht140_280_CVetoBVeto.deriv.DAOD_FTAG2.e4866_s3126_r10201_p3703
mc16_13TeV.363154.MGPy8EG_N30NLO_Zee_Ht140_280_CFilterBVeto.deriv.DAOD_FTAG2.e4866_s3126_r10201_p3703
mc16_13TeV.363155.MGPy8EG_N30NLO_Zee_Ht140_280_BFilter.deriv.DAOD_FTAG2.e4866_s3126_r10201_p3703
mc16_13TeV.363156.MGPy8EG_N30NLO_Zee_Ht280_500_CVetoBVeto.deriv.DAOD_FTAG2.e4866_s3126_r10201_p3703
mc16_13TeV.363157.MGPy8EG_N30NLO_Zee_Ht280_500_CFilterBVeto.deriv.DAOD_FTAG2.e4866_s3126_r10201_p3703
mc16_13TeV.363158.MGPy8EG_N30NLO_Zee_Ht280_500_BFilter.deriv.DAOD_FTAG2.e4866_s3126_r10201_p3703
mc16_13TeV.363159.MGPy8EG_N30NLO_Zee_Ht500_700_CVetoBVeto.deriv.DAOD_FTAG2.e4866_s3126_r10201_p3703
mc16_13TeV.363160.MGPy8EG_N30NLO_Zee_Ht500_700_CFilterBVeto.deriv.DAOD_FTAG2.e4866_s3126_r10201_p3703
mc16_13TeV.363161.MGPy8EG_N30NLO_Zee_Ht500_700_BFilter.deriv.DAOD_FTAG2.e4866_s3126_r10201_p3703
mc16_13TeV.363162.MGPy8EG_N30NLO_Zee_Ht700_1000_CVetoBVeto.deriv.DAOD_FTAG2.e4866_s3126_r10201_p3703
mc16_13TeV.363163.MGPy8EG_N30NLO_Zee_Ht700_1000_CFilterBVeto.deriv.DAOD_FTAG2.e4866_s3126_r10201_p3703
mc16_13TeV.363164.MGPy8EG_N30NLO_Zee_Ht700_1000_BFilter.deriv.DAOD_FTAG2.e4866_s3126_r10201_p3703
mc16_13TeV.363165.MGPy8EG_N30NLO_Zee_Ht1000_2000_CVetoBVeto.deriv.DAOD_FTAG2.e4866_s3126_r10201_p3703
mc16_13TeV.363166.MGPy8EG_N30NLO_Zee_Ht1000_2000_CFilterBVeto.deriv.DAOD_FTAG2.e4866_s3126_r10201_p3703
mc16_13TeV.363167.MGPy8EG_N30NLO_Zee_Ht1000_2000_BFilter.deriv.DAOD_FTAG2.e4866_s3126_r10201_p3703
mc16_13TeV.363168.MGPy8EG_N30NLO_Zee_Ht2000_E_CMS_CVetoBVeto.deriv.DAOD_FTAG2.e4866_s3126_r10201_p3703
mc16_13TeV.363169.MGPy8EG_N30NLO_Zee_Ht2000_E_CMS_CFilterBVeto.deriv.DAOD_FTAG2.e4866_s3126_r10201_p3703
mc16_13TeV.363170.MGPy8EG_N30NLO_Zee_Ht2000_E_CMS_BFilter.deriv.DAOD_FTAG2.e4866_s3126_r10201_p3703
mc16_13TeV.361510.MadGraphPythia8EvtGen_A14NNPDF23LO_Ztautau_Np0.deriv.DAOD_FTAG2.e3898_s3126_r10201_p3703
mc16_13TeV.361511.MadGraphPythia8EvtGen_A14NNPDF23LO_Ztautau_Np1.deriv.DAOD_FTAG2.e3898_s3126_r10201_p3703
mc16_13TeV.361512.MadGraphPythia8EvtGen_A14NNPDF23LO_Ztautau_Np2.deriv.DAOD_FTAG2.e3898_s3126_r10201_p3703
mc16_13TeV.361513.MadGraphPythia8EvtGen_A14NNPDF23LO_Ztautau_Np3.deriv.DAOD_FTAG2.e3898_s3126_r10201_p3703
mc16_13TeV.361514.MadGraphPythia8EvtGen_A14NNPDF23LO_Ztautau_Np4.deriv.DAOD_FTAG2.e3898_s3126_r10201_p3703

Table 33: MC16d MC background samples used in this analysis. MC16a files correspond to 2017 data conditions.

Sample
Z + jets (MADGRAPH)
mc16_13TeV.363123.MGPy8EG_N30NLO_Zmumu_Ht0_70_CVetoBVeto.deriv.DAOD_FTAG2.e4649_s3126_r10724_p3703
mc16_13TeV.363124.MGPy8EG_N30NLO_Zmumu_Ht0_70_CFilterBVeto.deriv.DAOD_FTAG2.e4649_s3126_r10724_p3703
mc16_13TeV.363125.MGPy8EG_N30NLO_Zmumu_Ht0_70_BFilter.deriv.DAOD_FTAG2.e4649_s3126_r10724_p3703
mc16_13TeV.363126.MGPy8EG_N30NLO_Zmumu_Ht70_140_CVetoBVeto.deriv.DAOD_FTAG2.e4649_s3126_r10724_p3703
mc16_13TeV.363127.MGPy8EG_N30NLO_Zmumu_Ht70_140_CFilterBVeto.deriv.DAOD_FTAG2.e4649_s3126_r10724_p3703
mc16_13TeV.363128.MGPy8EG_N30NLO_Zmumu_Ht70_140_BFilter.deriv.DAOD_FTAG2.e4649_s3126_r10724_p3703
mc16_13TeV.363129.MGPy8EG_N30NLO_Zmumu_Ht140_280_CVetoBVeto.deriv.DAOD_FTAG2.e4649_s3126_r10724_p3703
mc16_13TeV.363130.MGPy8EG_N30NLO_Zmumu_Ht140_280_CFilterBVeto.deriv.DAOD_FTAG2.e4649_s3126_r10724_p3703
mc16_13TeV.363131.MGPy8EG_N30NLO_Zmumu_Ht140_280_BFilter.deriv.DAOD_FTAG2.e4649_s3126_r10724_p3703
mc16_13TeV.363132.MGPy8EG_N30NLO_Zmumu_Ht280_500_CVetoBVeto.deriv.DAOD_FTAG2.e4649_s3126_r10724_p3703
mc16_13TeV.363133.MGPy8EG_N30NLO_Zmumu_Ht280_500_CFilterBVeto.deriv.DAOD_FTAG2.e4649_s3126_r10724_p3703
mc16_13TeV.363134.MGPy8EG_N30NLO_Zmumu_Ht280_500_BFilter.deriv.DAOD_FTAG2.e4649_s3126_r10724_p3703
mc16_13TeV.363135.MGPy8EG_N30NLO_Zmumu_Ht500_700_CVetoBVeto.deriv.DAOD_FTAG2.e4649_s3126_r10724_p3703
mc16_13TeV.363136.MGPy8EG_N30NLO_Zmumu_Ht500_700_CFilterBVeto.deriv.DAOD_FTAG2.e4649_s3126_r10724_p3703
mc16_13TeV.363137.MGPy8EG_N30NLO_Zmumu_Ht500_700_BFilter.deriv.DAOD_FTAG2.e4649_s3126_r10724_p3703
mc16_13TeV.363138.MGPy8EG_N30NLO_Zmumu_Ht700_1000_CVetoBVeto.deriv.DAOD_FTAG2.e4649_s3126_r10724_p3703
mc16_13TeV.363139.MGPy8EG_N30NLO_Zmumu_Ht700_1000_CFilterBVeto.deriv.DAOD_FTAG2.e4649_s3126_r10724_p3703
mc16_13TeV.363140.MGPy8EG_N30NLO_Zmumu_Ht700_1000_BFilter.deriv.DAOD_FTAG2.e4649_s3126_r10724_p3703
mc16_13TeV.363141.MGPy8EG_N30NLO_Zmumu_Ht1000_2000_CVetoBVeto.deriv.DAOD_FTAG2.e4649_s3126_r10724_p3703
mc16_13TeV.363142.MGPy8EG_N30NLO_Zmumu_Ht1000_2000_CFilterBVeto.deriv.DAOD_FTAG2.e4649_s3126_r10724_p3703
mc16_13TeV.363143.MGPy8EG_N30NLO_Zmumu_Ht1000_2000_BFilter.deriv.DAOD_FTAG2.e4649_s3126_r10724_p3703
mc16_13TeV.363144.MGPy8EG_N30NLO_Zmumu_Ht2000_E_CMS_CVetoBVeto.deriv.DAOD_FTAG2.e4649_s3126_r10724_p3703
mc16_13TeV.363145.MGPy8EG_N30NLO_Zmumu_Ht2000_E_CMS_CFilterBVeto.deriv.DAOD_FTAG2.e4649_s3126_r10724_p3703
mc16_13TeV.363146.MGPy8EG_N30NLO_Zmumu_Ht2000_E_CMS_BFilter.deriv.DAOD_FTAG2.e4649_s3126_r10724_p3703
mc16_13TeV.363147.MGPy8EG_N30NLO_Zee_Ht0_70_CVetoBVeto.deriv.DAOD_FTAG2.e4866_s3126_r10724_p3703
mc16_13TeV.363148.MGPy8EG_N30NLO_Zee_Ht0_70_CFilterBVeto.deriv.DAOD_FTAG2.e4866_s3126_r10724_p3703
mc16_13TeV.363149.MGPy8EG_N30NLO_Zee_Ht0_70_BFilter.deriv.DAOD_FTAG2.e4866_s3126_r10724_p3703
mc16_13TeV.363150.MGPy8EG_N30NLO_Zee_Ht70_140_CVetoBVeto.deriv.DAOD_FTAG2.e4866_s3126_r10724_p3703
mc16_13TeV.363151.MGPy8EG_N30NLO_Zee_Ht70_140_CFilterBVeto.deriv.DAOD_FTAG2.e4866_s3126_r10724_p3703
mc16_13TeV.363152.MGPy8EG_N30NLO_Zee_Ht70_140_BFilter.deriv.DAOD_FTAG2.e4866_s3126_r10724_p3703
mc16_13TeV.363153.MGPy8EG_N30NLO_Zee_Ht140_280_CVetoBVeto.deriv.DAOD_FTAG2.e4866_s3126_r10724_p3703
mc16_13TeV.363154.MGPy8EG_N30NLO_Zee_Ht140_280_CFilterBVeto.deriv.DAOD_FTAG2.e4866_s3126_r10724_p3703
mc16_13TeV.363155.MGPy8EG_N30NLO_Zee_Ht140_280_BFilter.deriv.DAOD_FTAG2.e4866_s3126_r10724_p3703
mc16_13TeV.363156.MGPy8EG_N30NLO_Zee_Ht280_500_CVetoBVeto.deriv.DAOD_FTAG2.e4866_s3126_r10724_p3703
mc16_13TeV.363157.MGPy8EG_N30NLO_Zee_Ht280_500_CFilterBVeto.deriv.DAOD_FTAG2.e4866_s3126_r10724_p3703
mc16_13TeV.363158.MGPy8EG_N30NLO_Zee_Ht280_500_BFilter.deriv.DAOD_FTAG2.e4866_s3126_r10724_p3703
mc16_13TeV.363159.MGPy8EG_N30NLO_Zee_Ht500_700_CVetoBVeto.deriv.DAOD_FTAG2.e4866_s3126_r10724_p3703
mc16_13TeV.363160.MGPy8EG_N30NLO_Zee_Ht500_700_CFilterBVeto.deriv.DAOD_FTAG2.e4866_s3126_r10724_p3703
mc16_13TeV.363161.MGPy8EG_N30NLO_Zee_Ht500_700_BFilter.deriv.DAOD_FTAG2.e4866_s3126_r10724_p3703
mc16_13TeV.363162.MGPy8EG_N30NLO_Zee_Ht700_1000_CVetoBVeto.deriv.DAOD_FTAG2.e4866_s3126_r10724_p3703
mc16_13TeV.363163.MGPy8EG_N30NLO_Zee_Ht700_1000_CFilterBVeto.deriv.DAOD_FTAG2.e4866_s3126_r10724_p3703
mc16_13TeV.363164.MGPy8EG_N30NLO_Zee_Ht700_1000_BFilter.deriv.DAOD_FTAG2.e4866_s3126_r10724_p3703
mc16_13TeV.363165.MGPy8EG_N30NLO_Zee_Ht1000_2000_CVetoBVeto.deriv.DAOD_FTAG2.e4866_s3126_r10724_p3703
mc16_13TeV.363166.MGPy8EG_N30NLO_Zee_Ht1000_2000_CFilterBVeto.deriv.DAOD_FTAG2.e4866_s3126_r10724_p3703
mc16_13TeV.363167.MGPy8EG_N30NLO_Zee_Ht1000_2000_BFilter.deriv.DAOD_FTAG2.e4866_s3126_r10724_p3703
mc16_13TeV.363168.MGPy8EG_N30NLO_Zee_Ht2000_E_CMS_CVetoBVeto.deriv.DAOD_FTAG2.e4866_s3126_r10724_p3703
mc16_13TeV.363169.MGPy8EG_N30NLO_Zee_Ht2000_E_CMS_CFilterBVeto.deriv.DAOD_FTAG2.e4866_s3126_r10724_p3703
mc16_13TeV.363170.MGPy8EG_N30NLO_Zee_Ht2000_E_CMS_BFilter.deriv.DAOD_FTAG2.e4866_s3126_r10724_p3703
mc16_13TeV.361510.MadGraphPythia8EvtGen_A14NNPDF23LO_Ztautau_Np0.deriv.DAOD_FTAG2.e3898_s3126_r10724_p3703
mc16_13TeV.361511.MadGraphPythia8EvtGen_A14NNPDF23LO_Ztautau_Np1.deriv.DAOD_FTAG2.e3898_s3126_r10724_p3703
mc16_13TeV.361512.MadGraphPythia8EvtGen_A14NNPDF23LO_Ztautau_Np2.deriv.DAOD_FTAG2.e3898_s3126_r10724_p3703
mc16_13TeV.361513.MadGraphPythia8EvtGen_A14NNPDF23LO_Ztautau_Np3.deriv.DAOD_FTAG2.e3898_s3126_r10724_p3703
mc16_13TeV.361514.MadGraphPythia8EvtGen_A14NNPDF23LO_Ztautau_Np4.deriv.DAOD_FTAG2.e3898_s3126_r10724_p3703

Table 34: MC16e MC background samples used in this analysis. MC16a files correspond to 2017 data conditions.

D Trigger Studies

The trigger efficiencies after pre-selection are shown in Table 35. The inclusion of di-lepton triggers was found to result in just a ∼ 2% gain in signal efficiency, while letting in more background and increasing the uncertainty on the trigger scale factors (also making the *TrigGlobalEfficiencyCorrectionTool* tool insufficient for the evaluation of these uncertainties). For this reason these di-lepton triggers were not included.

Sample	Single Trigger Efficiency	Fractional Efficiency Gain
0.5 GeV a	93.6 ± 0.7%	2.4 ± 0.8%
2.5 GeV a	93.2 ± 0.7%	2.6 ± 0.7%
8 GeV a	93.9 ± 0.9%	2.5 ± 1%
η_c	93.4 ± 0.7%	2.8 ± 0.7%

Table 35: Trigger efficiencies for the nominal single lepton triggers after pre-selection, and fractional gain in trigger efficiency by introducing the dilepton triggers as well.

E Track Selection Studies

In order to reject the large contamination from pileup tracks, two track selection requirements are considered. One is a combination of the ATLAS *Loose* Track Quality and *Loose* track-to-vertex association (TTVA) requirements, which are implemented using the *InDetTrackSelectionTool* [64] and *TrackVertexAssociationTool* [65], respectively. The other requirement considered is a combination of the ATLAS Loose Track Quality and specifically optimised vertexing requirements (summarised in Table 36). While the custom requirements did result in a better signal to background ratio, then also resulted in a greater dependence on the signal hypothesis mass, as shown in Table 36. As such, the former requirement is chosen.

Signal Sample	Loose TTVA ($|d_0|$ < 2, $|\Delta z_0 sin\theta|$ < 3)		$|d_0|$ < 2, $|\Delta z_0 sin\theta|$ < 1, p_T > 1 GeV	
	Signal Efficiency	Pileup Efficiency	Signal Efficiency	Pileup Efficiency
0.5 GeV a	$96 \pm 7\%$	$41 \pm 3\%$	$94 \pm 7\%$	$26 \pm 2\%$
2.5 GeV a	$95 \pm 6\%$	$38 \pm 2\%$	$90 \pm 5\%$	$24 \pm 2\%$
8 GeV a	$94 \pm 6\%$	$47 \pm 3\%$	$83 \pm 5\%$	$32 \pm 2\%$
η_c	$95 \pm 4\%$	$37 \pm 2\%$	$88 \pm 4\%$	$23 \pm 2\%$

Table 36: Comparison of efficiencies of two track selection working points. Both working points include the *Loose* track selection working point. The *Loose* TMVA working point (in bold) is adopted for the analysis, while the other requirement was optimised specifically for the analysis.

F MVA Input Variable Reduction Studies

A BDT analogous to the one described in this section was trained without η, *angularity*(2), and both. The signal efficiencies for a 1% background efficiency are shown in Table 37. The efficiency loss from removing the *angularity*(2) variable was on the order of 2-12% (depending on the signal hypothesis), which warrants keeping the variable. However, the η variable resulted in a negligible loss in efficiency. As such, the next iteration of the analysis is expected to use a BDT without the η variable.

Sample	Nominal BDT	No η	No *angularity*(2)	No η or *angularity*(2)
0.5 GeV a	46.1%	46.1%	45.7%	45.2%
2.5 GeV a	17.7%	17.6%	15.5%	15.6%
8 GeV a	3.3%	3.4%	3.2%	3.0%
η_c	10.3%	10.0%	9.3%	9.3%

Table 37: Signal efficiencies for each of the BDTs described in subsubsection F, for a constant background efficiency of 1%.

G MVA Hyper-Parameter Studies

The variables used to definite the BDT with which the *X* particle is identified are: NTrees, the number of trees in the random forest; MaxDepth, the maximum depth of each decision tree; MinNodeSize, the minimum fraction of evens that may be contained in a tree node; nCuts, the number of cut values which are tested in each variable. Various values of these parameters were tested before settling on the default TMVA parameters. These tested values included: NTrees=400; NTrees=1200; MaxDepth=4; MinNodeSize=2%; MinNodeSize=2% and nCuts=50.

H MLP Pileup Dependence

Figures 40, 41 and 42 show the MLP distributions for events with 0-25, 25-40 and > 40 interactions per bunch crossing, respectively.
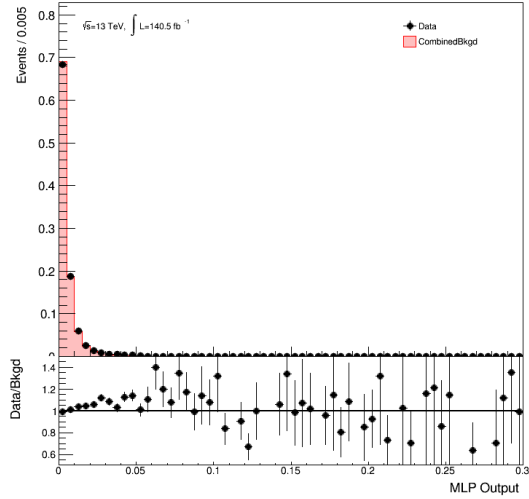
(a) Classification MLP
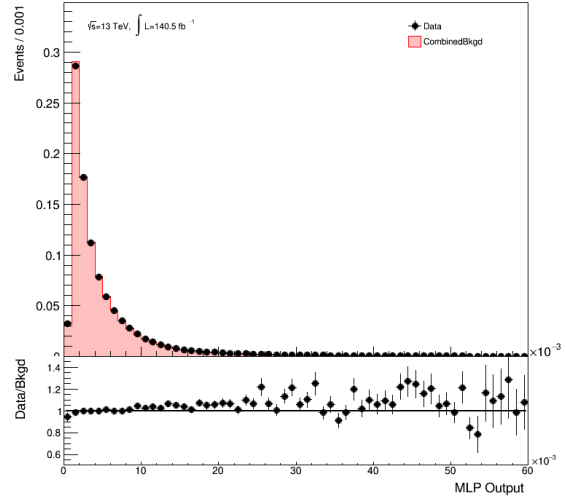
(b) Classification MLP (Zoomed)
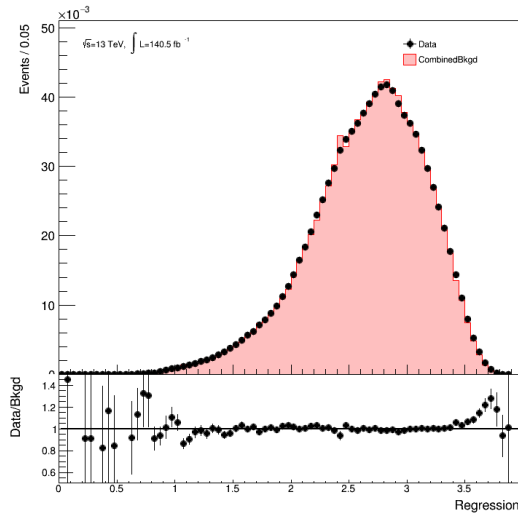
(c) Regression MLP

Figure 40: Classification MLP with a nominal (a) and zoomed (b) axis range, and regression MLP (c), for events with 0-25 interactions per bunch crossing.
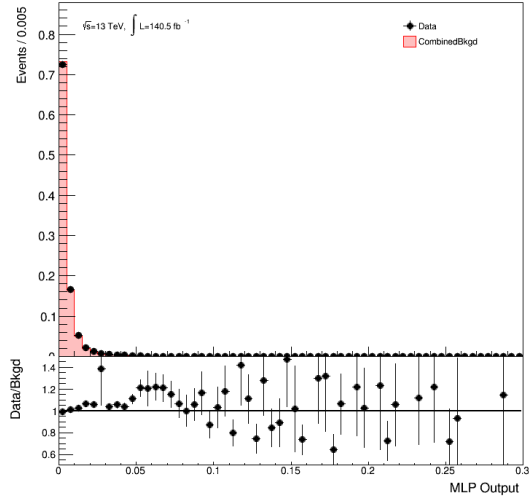
(a) Classification MLP
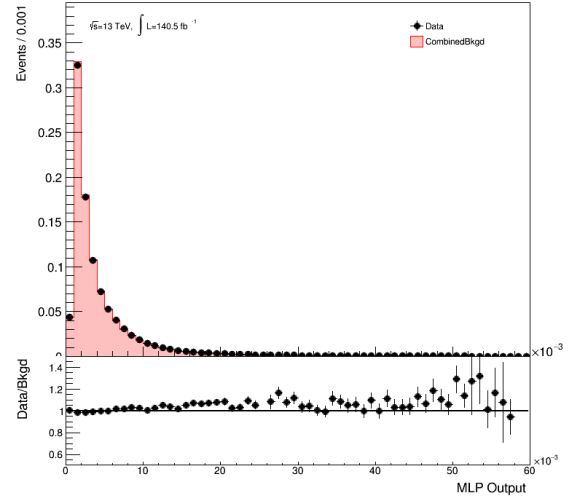
(b) Classification MLP (Zoomed)
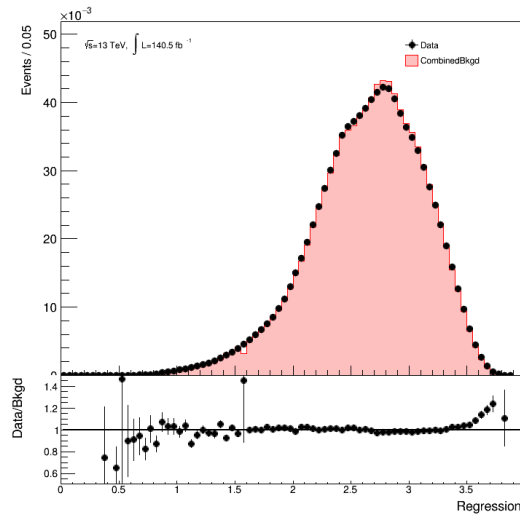
(c) Regression MLP

Figure 41: Classification MLP with a nominal (a) and zoomed (b) axis range, and regression MLP (c), for events with 25-40 interactions per bunch crossing.
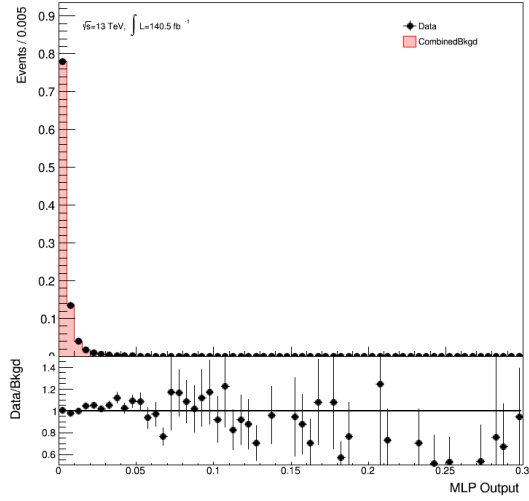
(a) Classification MLP
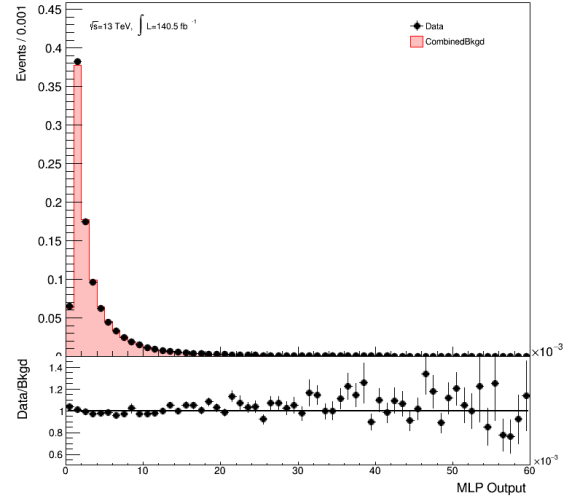
(b) Classification MLP (Zoomed)
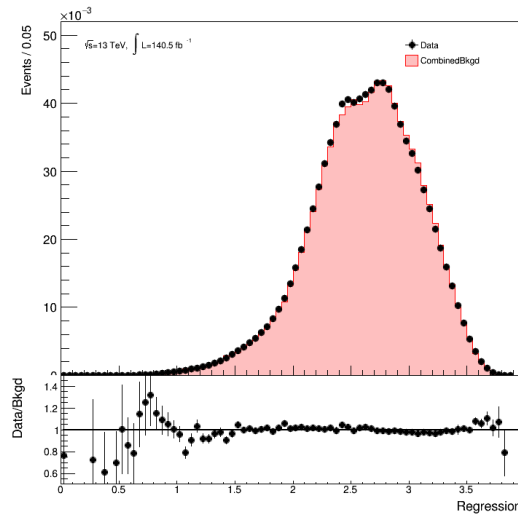
(c) Regression MLP

Figure 42: Classification MLP with a nominal (a) and zoomed (b) axis range, and regression MLP (c), for events with > 40 interactions per bunch crossing.

I MadGraph Reweighting Studies

The MadGraph Z + jets sample has been reweighted using a procedure designed to mitigate the observed mismodelling in the MadGraph Z + jets sample, using the p_T of the calorimeter jet, the p_T of the three body system, and the multiplicity of tracks Ghost-Associated to the calorimeter jet. Various distributions before and after this reweighting is applied are shown in Figures 43 to 48.
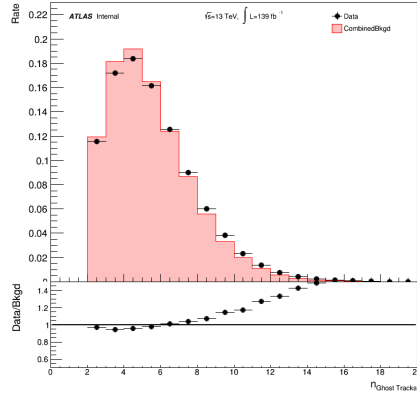
(a) n_{tracks} Pre-Reweighting
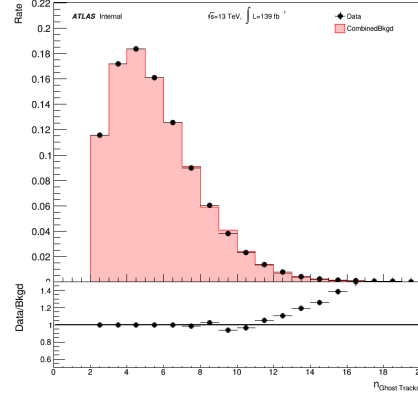
(b) n_{tracks} Post-Reweighting
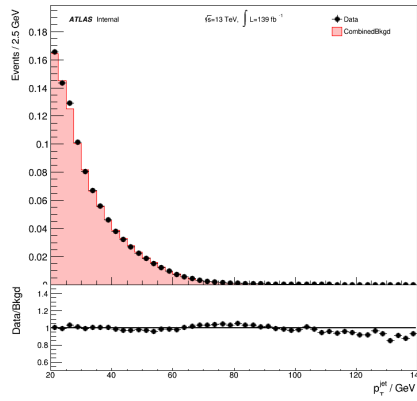
(c) $p_{\text{T}}^{\text{jet}}$ Pre-Reweighting
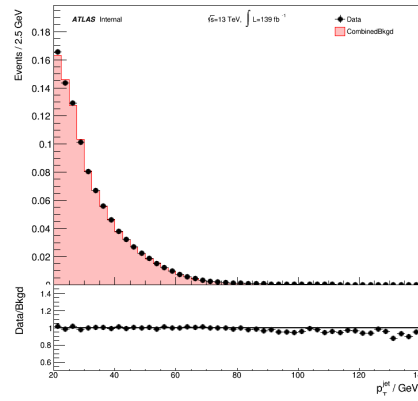
(d) $p_{\text{T}}^{\text{jet}}$ Post-Reweighting
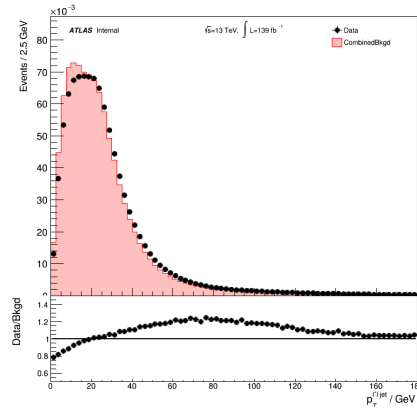
(e) $p_{\text{T}}^{\text{jet}}$ Pre-Reweighting
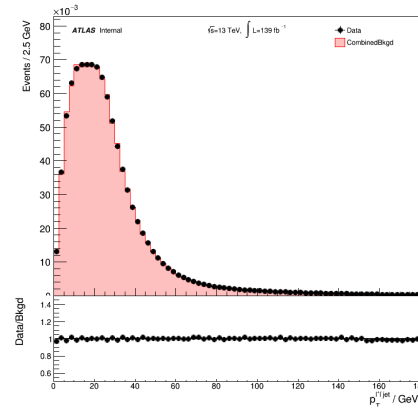
(f) $p_{\text{T}}^{\text{jet}}$ Post-Reweighting

Figure 43: Distributions of the three variables used to reweight the MADGRAPH Z + jets background simulation, after the full event-level pre-selection, in data and background MC (both reweighted and not). These variables are the ghost-associated track multiplicity (a and b), the transverse momentum of the calorimeter jet (c and d), and the transverse momentum of the three body system (e and f).
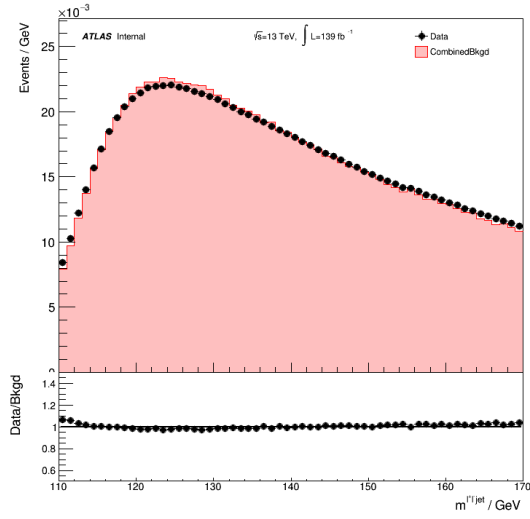
(a) $m_{\ell^+\ell^-\mathrm{j}}$ Pre-Reweighting
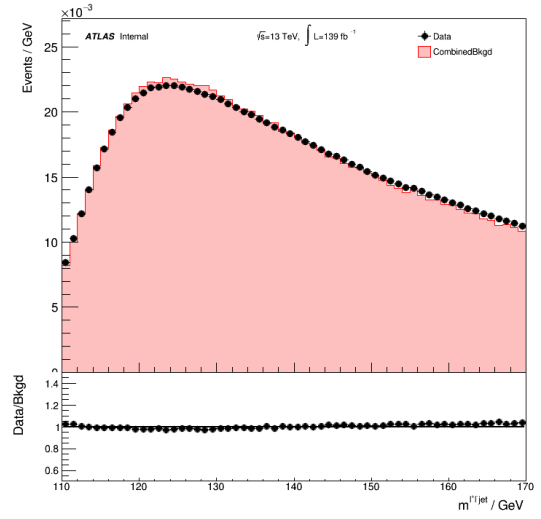
(b) $m_{\ell^+\ell^-\mathrm{j}}$ Post-Reweighting

Figure 44: Distributions of the three body mass distribution, after the full event-level pre-selection, in data and MADGRAPH Z + jets background MC (both reweighted and not).
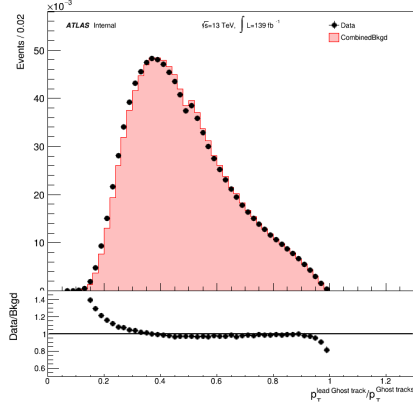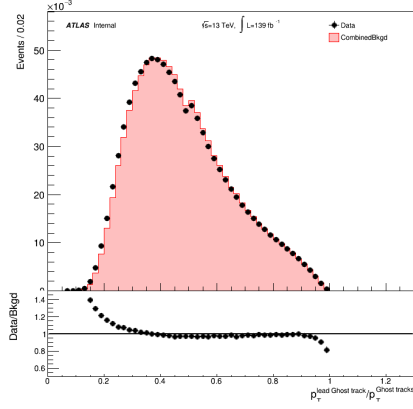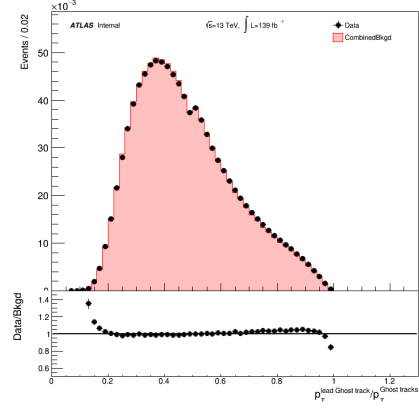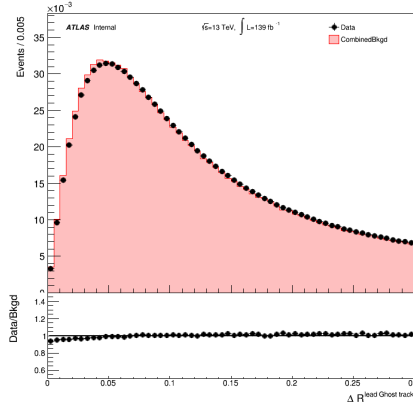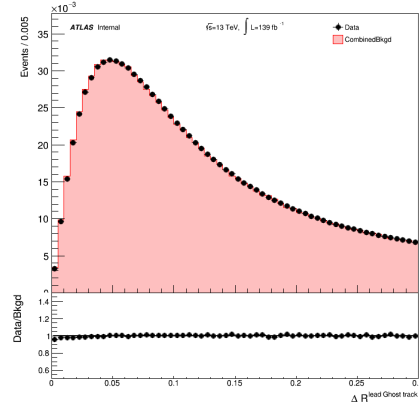
(a) $p_T^{\text{lead track}}/p_T^{\text{tracks}}$ Pre-Reweighting
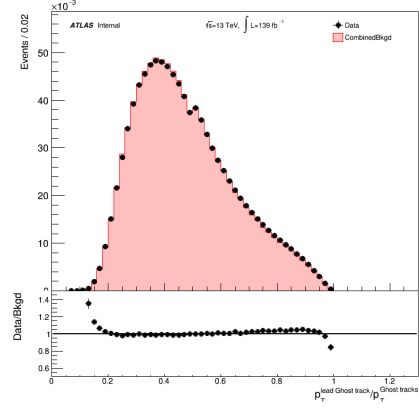
(b) $p_T^{\text{lead track}}/p_T^{\text{tracks}}$ Post-Reweighting
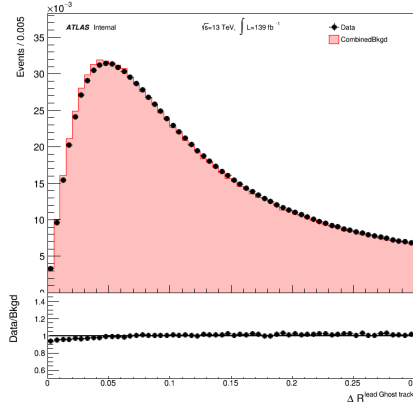
(c) $\Delta R^{\text{lead track, calo jet}}$ Pre-Reweighting
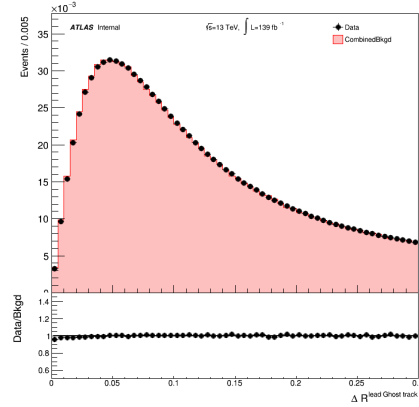
(d) $\Delta R^{\text{lead track, calo jet}}$ Post-Reweighting

Figure 45: Distributions of the variables input to the MLP, after the full event-level pre-selection, in data and MADGRAPH Z + jets background MC (both reweighted and not). In the case of exactly two tracks, the $p_T^{\text{lead track}}/p_T^{\text{tracks}}$ variable can not take values less than 0.5, leading to the spike around 0.5.

(a) $p_T^{\text{lead track}}/p_T^{\text{tracks}}$ Pre-Reweighting

(b) $p_T^{\text{lead track}}/p_T^{\text{tracks}}$ Post-Reweighting

(c) $\Delta R^{\text{lead track, calo jet}}$ Pre-Reweighting

(d) $\Delta R^{\text{lead track, calo jet}}$ Post-Reweighting

Figure 46: Distributions of the variables input to the MLP, after the full event-level pre-selection, in data and MadGraph Z + jets background MC (both reweighted and not). In the case of exactly two tracks, the $p_T^{\text{lead track}}/p_T^{\text{tracks}}$ variable can not take values less than 0.5, leading to the spike around 0.5.
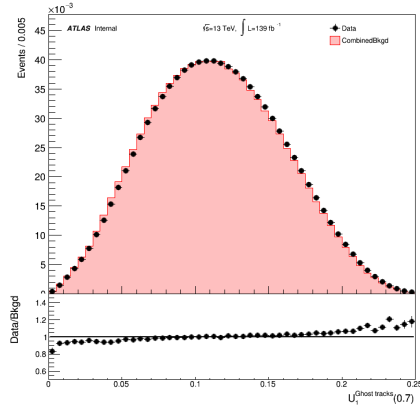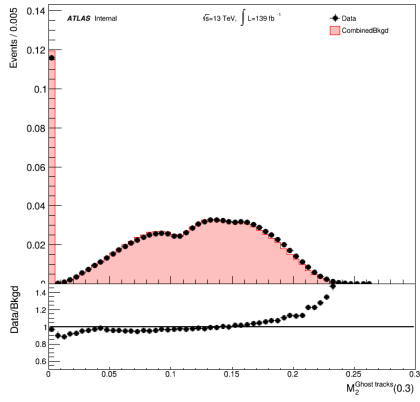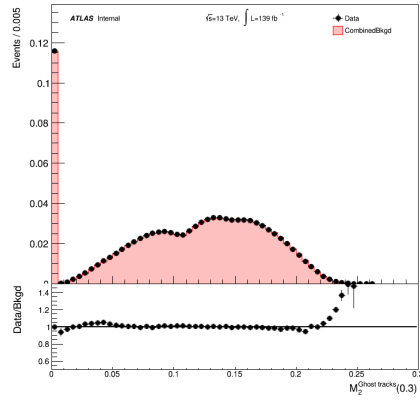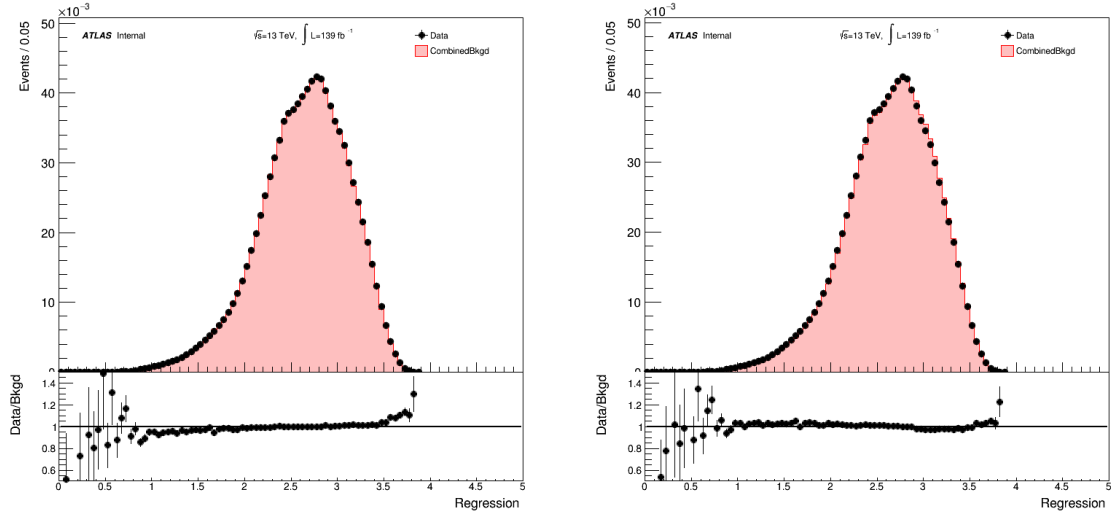
(a) $U_1(0.7)$ Pre-Reweighting
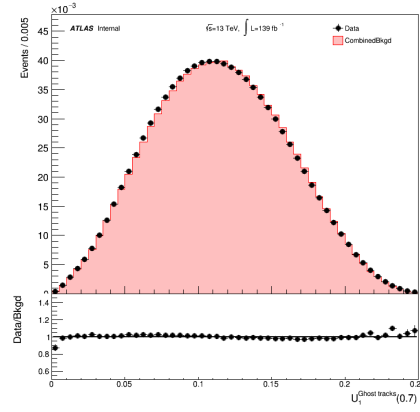
(b) $U_1(0.7)$ Post-Reweighting

(c) $M_2(0.3)$ Pre-Reweighting

(d) $M_2(0.3)$ Post-Reweighting

Figure 47: Distributions of the variables input to the MLP, after the full event-level pre-selection, in data and MADGRAPH Z + jets background MC (both reweighted and not).

(a) Mass Regression MLP Output Variable Pre-Reweighting (b) Mass Regression MLP Output Variable Post-Reweighting
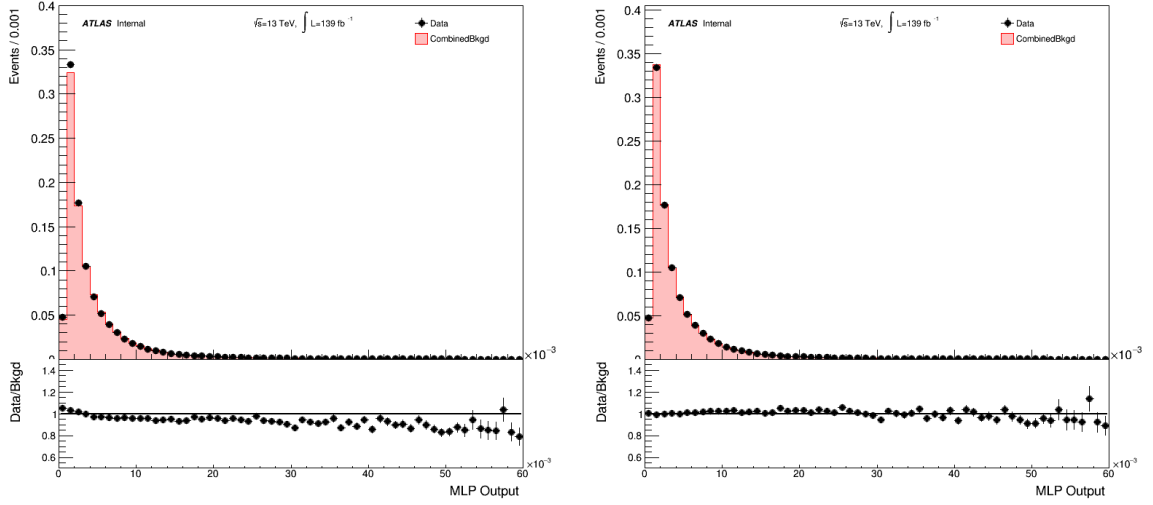
(c) Classification MLP Output Variable Pre-Reweighting (d) Classification MLP Output Variable Post-Reweighting

Figure 48: Distributions of the output of the regression (a) and classification (b) MLPs, after the full event-level pre-selection, in data and MADGRAPH Z + jets background MC (both reweighted and not).

J MLP Inputs in SR

The MLP inputs in the SR are given in Figure 49.

(a) $p_T^{\text{lead track}}/p_T^{\text{tracks}}$

(b) $\Delta R^{\text{lead track, calo jet}}$

(c) $U_1(0.7)$
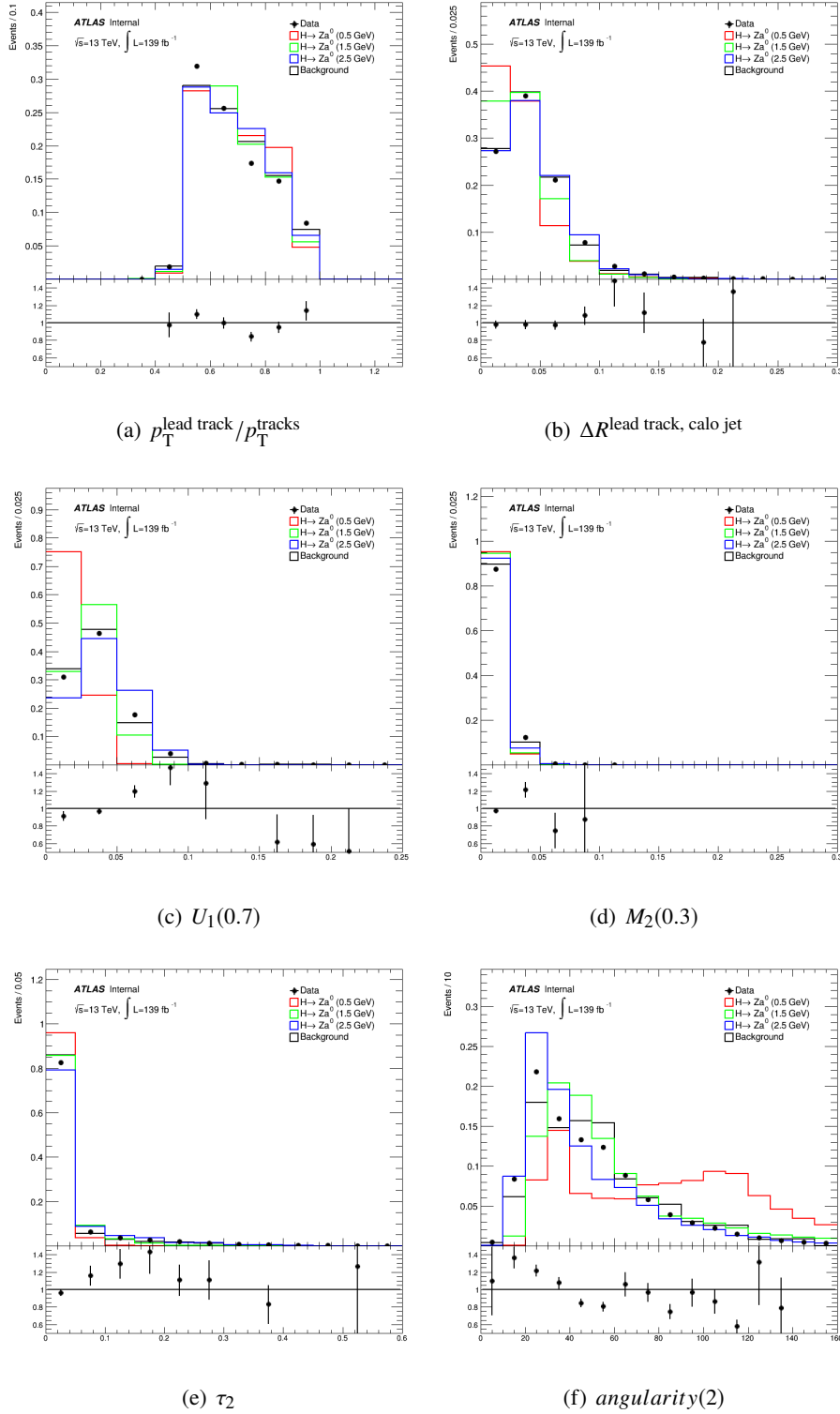
(d) $M_2(0.3)$

(e) τ_2

(f) $angularity(2)$

Figure 49: Distributions of the variables input to the MLP, after the full selection, in data and background MC (reweighted).

K Full Selection Cutflow

A summary of the full event selection, with an example cutflow is given in Figure 38.

Cut	Details	1.5 GeV a Cutflow
FTAG2	Event must enter FTAG2 derivation	44.0%
Triggers	Single lepton triggers requiring $p_{\mathrm{T}} > 27$ GeV	39.2%
Event Cleaning	Event Cleaning	39.1%
Leptons	e or $\mu \geq 2$	32.2%
Z boson	2 same-flavour opposite-sign leptons, with $|m^{ll} - m_Z| < 10$ GeV and $p_{\mathrm{T}}^{lead} > 27$ GeV	27.9%
Trigger Matching	One of the Z boson leptons must have triggered the event	27.8%
Select X-candidate as anti-k_T 4 topo EM jet ($p_{\mathrm{T}}^{jet} > 20$ GeV), with highest p_{T}, for which $m^{llj} < 250$ GeV		21.4%
FTAG2 Harmonisation Cuts	Lepton $p_{\mathrm{T}} > 18$ GeV	21.3%
> 2 tracks	≥ 2 tracks ghost associated to the calo jet, surviving track selection	20.3%
Higgs boson	120 GeV $< m^{llj} < 135$ GeV	8.34%
MLP	$MLP > 0.0524$	2.62%

Table 38: Summary of full event selection. The cutflow for the 1.5 GeV a signal sample is shown for the unweighted MC, relative to the initial number of events in the FTAG2 DxAOD.